GEO-3900

MASTER'S THESIS IN GEOLOGY

Geophysical investigation of faults and fractures in Upper-Palaeozoic carbonate build-ups at the Loppa High, SW Barents Sea

Tanya Kovacova

May, 2010

FACULTY OF SCIENCE,

Department of Geology,

University of Tromsø, Norway

GEO-3900

MASTER'S THESIS IN GEOLOGY

Geophysical investigation of faults and fractures in Upper-Palaeozoic carbonate build-ups at the Loppa High, SW Barents Sea

Tanya Kovacova

May, 2010

ACKNOWLEDGEMENTS

I would like to thank my supervisors Karin Andreassen, Kai Hogstad and Geir Elvebakk for giving me the opportunity to work on this interesting topic. This thesis was a great experience for me and I have learnt a lot. It would never be possible without your advice and guidance. I appreciate all of your input and help. It was a wonderful cooperation for me. I want to thank Karin for introducing me to Kai and Geir and for her support and encouragement during the whole process. I want to thank Kai for his feed-back which always made me think and forced me to explain myself much better than I would ever manage on my own. I want to thank Geir for inviting me to 'The Core Work Shop'. I have learnt there much more than I would ever expect and it was a great geological experience. Thanks for the knowledge I have gained on 'The Core Work Shop' belongs also to other participants: Lars Stemmerik, Mateu Esteban Cerdà and Pieter J. Pestman. I am grateful to Det norske oljeselskap, Harstad for financing this workshop for me.

For advice and consultation, I would also like to thank to: Mohamed Ali Matar, who was a great Petrel instructor, and also gave me advice regarding the interpretation of my data and helped me to understand the velocity modelling. To Bjarne Raffaelsen, who gave me advice in the beginning of my work with Ant-tracking, when I had a hard time believing that I am getting anywhere. To my grandma, who contributed by her knowledge and experience from years of academic work exactly when I needed it the most.

I would like to thank all of my friends both in Slovakia and Norway for making my life more colourful and for being exactly the way they are. A thank you belongs also to my fellow master students and my office mates for creating a good working environment, and especially to Linn for forcing me to speak Norwegian, and always consulting my journey through the thesis and life.

Last but not least I would like to thank all the members of my family for supporting me, when I followed my dreams and went to Norway. I am grateful to have you all. I wouldn't manage this without you. A very special thank you belongs to Finn-Henning, my fiancée, for always standing by my side and for making me happy every single day.

ABSTRACT

During previous studies of the Upper-Palaeozoic carbonate build-ups at the Loppa High in SW Barents Sea, a connection between locations of the build-ups and syn-depositional faults was observed. This thesis is studying this relationship in detail, applying the Ant-tracking semi-automated method for detection of faults. To my knowledge, this relatively new method has not been used in the Barents Sea area before. The Ant-tracking is a patent protected technology developed by Schlumberger Stavanger Research for Petrel^{TM} software for automatic detection of faults and fractures from three dimensional seismic data. In this thesis, two 3D seismic surveys were used the SG9810 survey and the high resolution NH0372 site survey. In both of these surveys faults and fractures were revealed. These were further analyzed and also visualized in three dimensions. The connection between the positions of the Upper-Palaeozoic carbonate build-ups and the positions of faults and fractures was confirmed. Furthermore, all the detected build-ups were associated with one or two faults or fractures.

Key words: fault, fracture, Ant-tracking, carbonate build-up, Loppa High

CONTENTS

1. Introduction

Carbonate rocks contribute with approximately 10% of the worlds' sedimentary rocks but contain about half of the world's oil and gas resources (Ahr, 2008). There are many topics of interest concerning carbonate rocks, like composition, structure, porosity development, deposition and depositional environment, and other. Faults in carbonate rocks are studied in several significant projects worldwide (e.g. UniCam, 2006, SwRI®, 2007). Many papers describe faults connected to carbonate build-ups, observed in out-crops on shore (e.g. Stemmerik *et al.*, 1994), as well as in two dimensional (2D) (e.g. Hovland *et al.*, 1994) and three dimensional (3D) seismic data (e.g. Elvebakk *et al.*, 2002, Rafaelsen *et al.*, 2003a, Rafaelsen *et al.*, 2008). According to Stemmerik and Worsley (1989) and Stemmerik et al. (1999) deposition of Upper Carboniferous – Lower Permian carbonate build-ups is influenced by high-frequency and high-amplitude, glacioeustatic sea-level fluctuations. Rafaelsen et al. (2003a, 2008) states, from 3D surveys in the Barents Sea, that the location of carbonate build-ups is controlled by faults and sea floor morphology at the time of their deposition. Elvebakk *et al.* (2002) described a direct relationship between location of the polygonal network build-ups and the mapped position of syndepositional faults.

There are different approaches to fault interpretation. It can be done manually, or using a semi-automated interpretation method. The Ant-tracking algorithm, first time introduced by Pedersen *et al.* (2002) and developed by Schlumberger Stavanger Research for Petrel™ software, is a new unique algorithm and a part of an innovative workflow. The Ant-tracking algorithm workflow is a powerful tool designed for the interpretation of faults. It also detects minor faults and fractures not noticeable directly from amplitude seismic data and enhances other linear anomalies and discontinuities (Pedersen *et al.*, 2005). To detect only preferred anomalies as faults and fractures, preconditioning of the data is inevitable.

Several papers (e.g. Silva *et al.*, 2005) have confirmed that Ant-tracking algorithm is one of the most effective methods for interpreting and extracting faults. Silva et al. (2005) concluded that the fault interpretation using Ant-tracking is more than three times faster than manual fault interpretation. Because this method is relatively new, there are only few publications mentioning successful application of Ant-tracking for

fault recognition, e.g. Sutadiwiria and Prasetyo (2006) for a potential carbonate field offshore Indonesia, or Shi (2009) for the Chengdao Oilfield offshore China.

In the Loppa High area, SW Barents Sea (Figure 1.1), carbonate build-ups have been studied using both 2D (Stemmerik *et al.*, 1999) and 3D seismic data (Elvebakk *et al.*, 2002, Hunt *et al.*, 2003, Rafaelsen *et al.*, 2003b, Carrillat *et al.*, 2005). The application of 3D seismic data (Elvebakk *et al.*, 2002), revealed that Upper Palaeozoic carbonate build-ups in this area are not isolated, as assumed before, but create inter-connected mosaics of laterally linked ridges, referred to as polygonal network build-ups, enclosing polygonal lagoons. Furthermore, Elvebakk et al. (2002) confirmed that this pattern is not only local phenomena but occurs also in other areas of Barents Sea. Carrillat et al. (2005) presented 3D multi-attribute seismic data analysis for supervised automated 3D mapping of carbonate build-ups and palaeokarst facies at Loppa High. The visualisation of karst also revealed fault control on the location of the build-ups.

However, there are no publications that have applied the Ant-tracking algorithm for study of faults and fractures in carbonates in the Barents Sea area. The overall objective of this thesis is ***to investigate, analyze and visualize in three dimensional images the relationship between faults and fractures, and Palaeozoic warm water carbonate build-ups at the Loppa High, SW Barents Sea*** (Figure 1.1). To achieve this, the Ant-tracking algorithm workflow will be applied to 3D seismic data. The parameters of the workflow will be tested and customized to fit this case.

1.1. Study area

The Barents Sea (Figure 1.2) is an epicontinental sea, bordered by Svalbard archipelago to the northwest, Franz Josef Land to the northeast, Novaya Zemlya to the east and by Russia and Norway to the south. Its western border towards the Greenland Sea and the Norwegian Sea is a continental slope (Figure 1.1A).

The 3D seismic study area is located at the Loppa High, a structural high approximately halfway between Norway and the Bjørnøya island (Figure 1.1A).

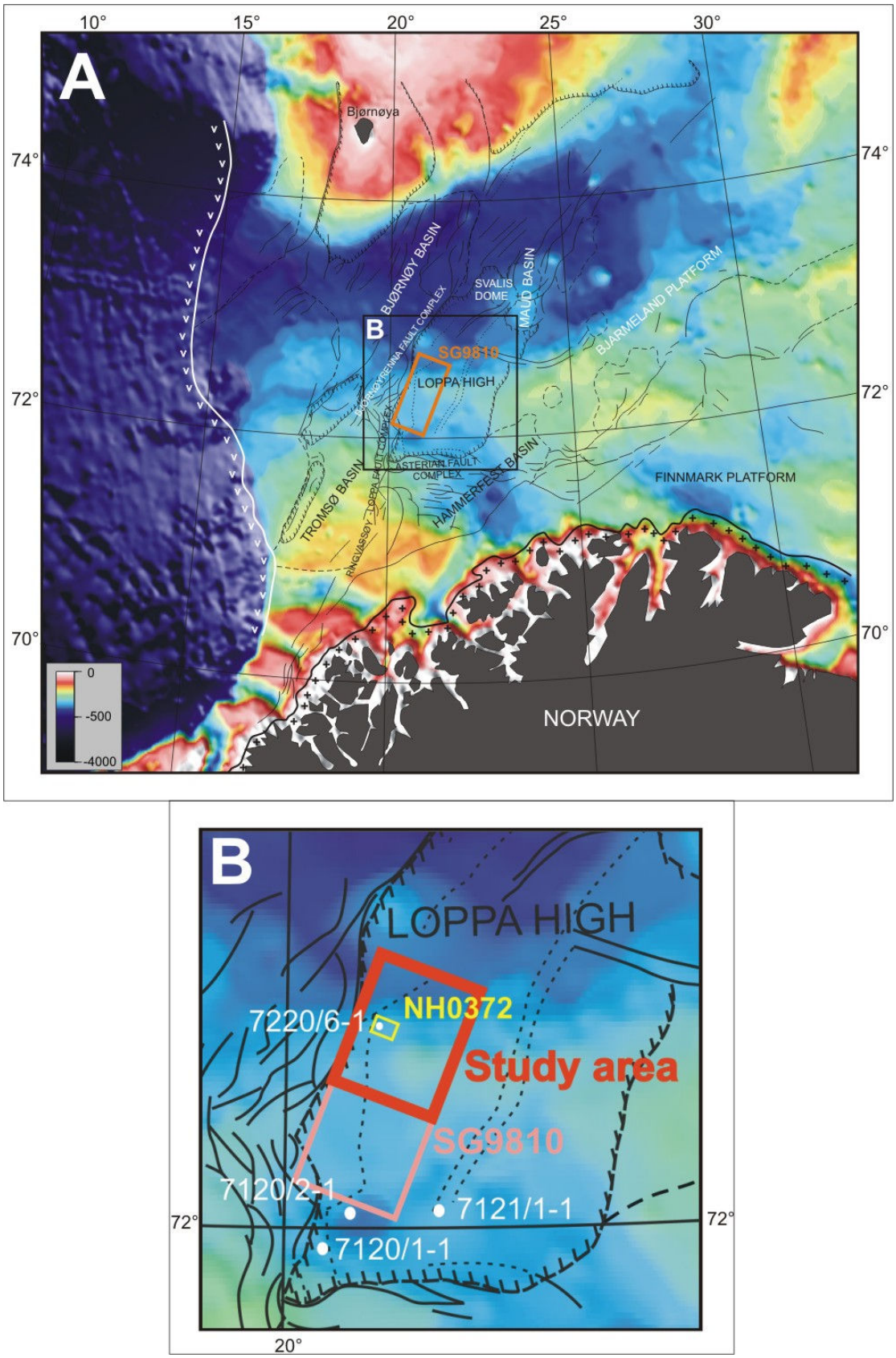

Figure 1.1 (A) Bathymetry map of Barents Sea (Modified from Larsen *et al.*, 2003) overlaid by map of main structural features in the area (Modified from Gabrielsen *et al.*, 1990). (B) Detailed map of Loppa High. Positions of 3D seismic surveys SG9810 and NH0372 (site survey), study area and four wells are indicated.

Figure 1.2 The map shows the location of the Barents Sea north of Russia and Norway, and the surrounding seas and islands (Modified from NormanEinstein, 2005). Position of Figure 1.1A is indicated by the black rectangle.

The Loppa High was considered one of several key exploration areas for the Upper Palaeozoic rocks in the "Barents Sea Project", a cooperative effort between the authorities and the oil industry (Larssen *et al.*, 2002). Three exploration wells were drilled here (7120/1-1, 7120/2-1 and 7121/1-1) before year 2002 (Figure 1.1B). The wells tested the Upper Palaeozoic succession on the high (Figure 1.3) (Larssen *et al.*, 2002). Well 7220/6-1 (Figure 1.1B), which is part of the data input to this thesis, was drilled in 2005 and penetrates the Upper Carboniferous carbonates of the Gipsdalen Group and into Caledonian basement (NPD, 2009).

1.1.1. Geological structural setting

Gabrielsen et al. (1990) defined structural elements of the Norwegian continental shelf. The Loppa High (Figure 1.1B) consists of an eastern platform and a crestal western and north-western margin (Figure 1.4). It is bounded by the Asterian Fault Complex to the south - to the Hammerfest Basin, and by Ringvassøy-Loppa and Bjørnøyrenna Fault Complexes to the west - to the Tromsø and Bjørnøya basins (Figure 1.1A). The eastern boundary is a monocline towards the Hammerfest Basin

and the Bjarmeland Platform and the northern boundary is the Svalis Dome with its associated rim syncline, the Maud Basin.

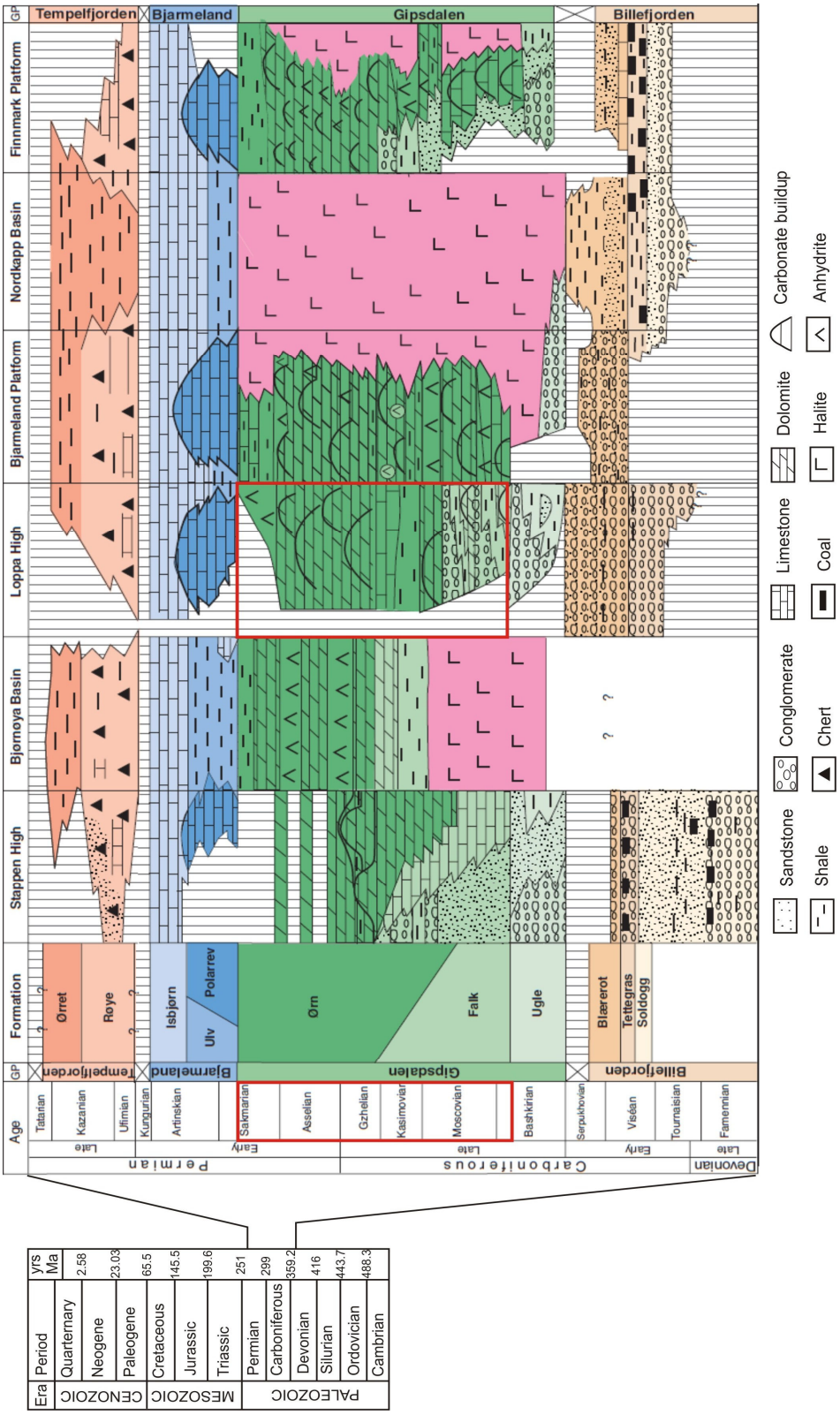

Figure 1.3 Correlation of Upper Palaeozoic lithostratigraphic units in the offshore areas of the southern Norwegian Barents Sea (modified from Larssen *et al.*, 2002). The stratigraphical interval studied in the thesis is indicated by red rectangles.

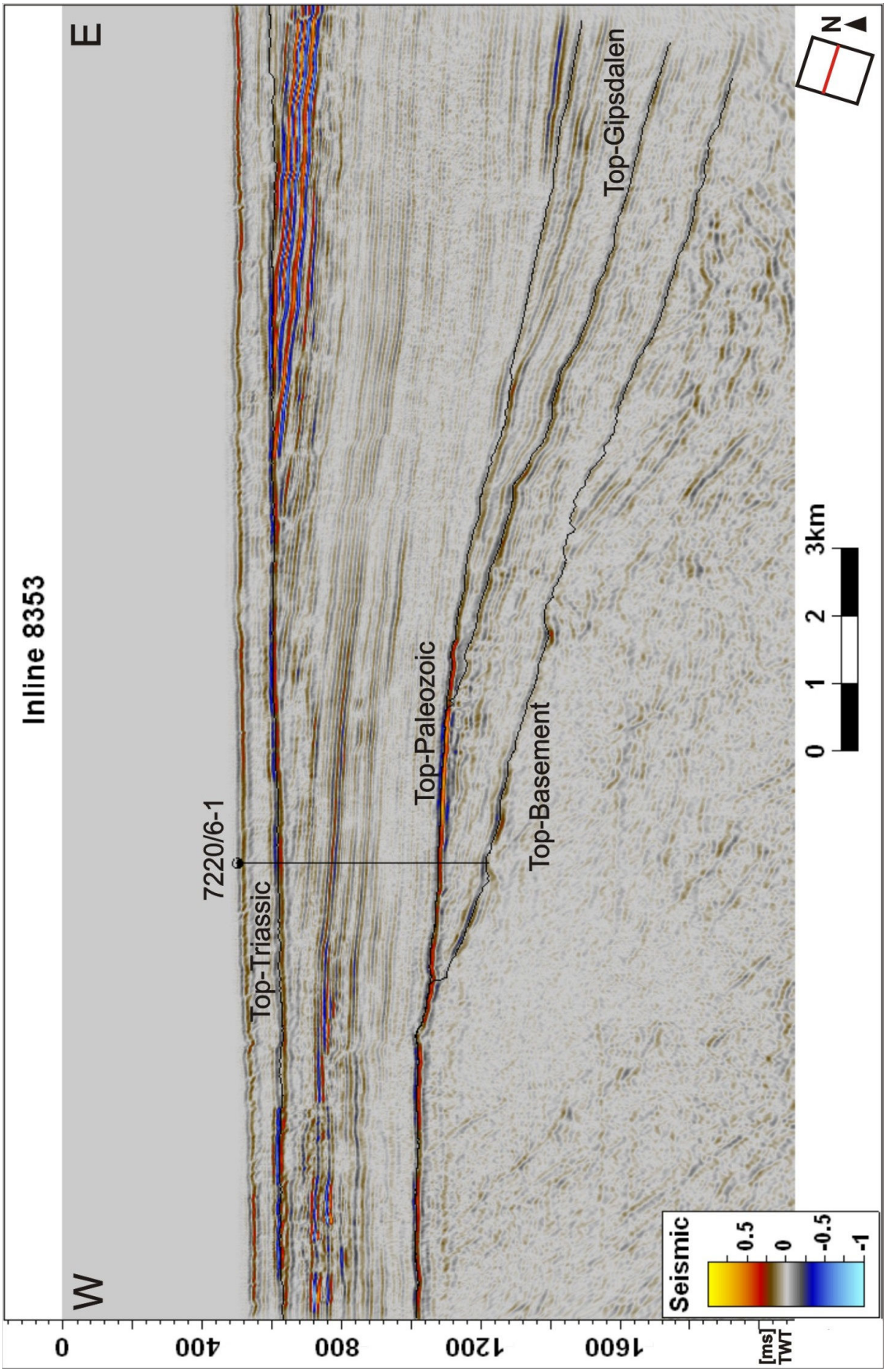

Figure 1.4 Seismic line across the study area, showing the positions of Top-Triassic, Top-Palaeozoic, Top-Gipsdalen and Top-Basement surfaces and the well 7220/6-1.

The Loppa High has mid-Carboniferous rift topography that was filled and draped successively by Upper Palaeozoic siliciclastic evaporites and carbonate deposits (Figure 1.3) (Larssen *et al.*, 2002). The Triassic succession is unusually thick (Figure 1.4), deposited during rapid subsidence. It contains siliciclastic sediments of the Ladinian-Norian Snadd Formation (NPD, 2010).

During the Upper Palaeozoic, the Barents Sea formed part of a vast continental shelf (Figure 1.5) extending from the Arctic Russia westwards through northern Greenland and the Arctic Canada Sverdrup Basin to Alaska (Worsley *et al.*, 1986, Beauchamp *et al.*, 1989, Doré, 1991, Stemmerik and Worsley, 1989). Since the Caledonian orogenic movements terminated in Early Devonian, the Barents Sea region has been affected by several phases of tectonism (Gabrielsen *et al.*, 1990).

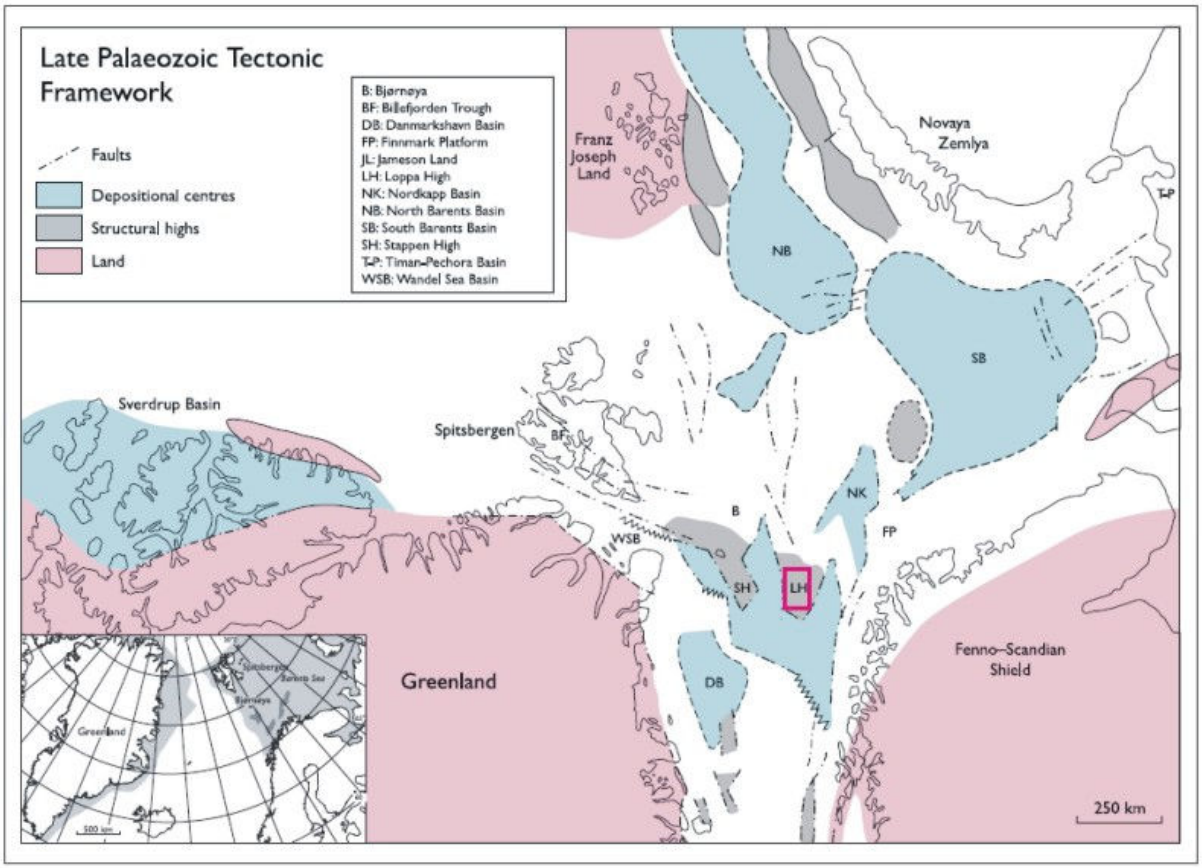

Figure 1.5 The northern margin of Pangaea during Upper Palaeozoic, showing major structural elements. Inset map shows the present day position of Greenland and Norway and the adjacent shelf areas (From Stemmerik and Worsley, 2005).

Gabrielsen et al. (1990) described structural development of the Norwegian continental shelf. The west of Loppa High was influenced by NNW-SSE trending structures during Late Devonian and Early Carboniferous (Rønnevik *et al.*, 1982).

Then, the block faulting occurred in Late Carboniferous and Early Permian (Brekke and Riis, 1987), together with NNE-SSW trending structures prevailing in the western Loppa High area. In mid-Sakmarian, the crestal area of the Loppa High was uplifted and rotated towards east and formed an island in the Barents Sea, which was drowned by a transgression in the Middle Triassic. This phase is linked to main faulting to the west of the Loppa High along a structural trend, the Polhem Fault Complex. During otherwise relatively quiet period, the latest Triassic and Early Jurassic, tilting occurred on Loppa High. Block faulting started again in the Early Jurassic and continued into Early Cretaceous (Berglund *et al.*, 1986) and resulted in the present day outline of the Loppa High. The Loppa High was uplifted and became an island in the Early Cretaceous (Gabrielsen *et al.*, 1990). Towards the end of the Cretaceous, renewed tectonic activities took place and are thought to be formed in response to strike slip movements along the Wandel Sea strike slip mobile zone and the Senja Fracture Zone and later by the opening of the Norwegian-Greenland Sea in the Paleocene-Eocene. The structures include reverse faulting and folding, and also extensional faulting in some areas (Gabrielsen *et al.*, 1990).

1.2. Carbonate build-ups

The term carbonate build-up (Figure 1.6) describes carbonate deposits of limited lateral extend, consisting of rocks built essentially of organisms (Scoffin, 1987). Carbonate build-ups are deposited on seafloor and create mounded structures with positive topographic relief.

In the investigated area of Loppa High, carbonate build-ups form inter-connected mosaics of laterally linked ridges, enclosing polygonal lagoons (Figure 1.6A) (Elvebakk *et al.*, 2002). Build-ups' deposition is dependent on sea-level changes (Stemmerik and Worsley, 1989, Stemmerik *et al.*, 1999). The reef-building organisms require water movement to carry nutrients to them (Scoffin, 1987), which causes build-ups' growth in shallow shelf areas. The location of initial reef growth is also governed by substrate, organisms creating build-ups prefer to attach to a firm substrate, in association with topographic elevated areas (Scoffin, 1987, Rafaelsen *et al.*, 2008), often created by syndepositional faulting. In the Gipsdalen Group (Figure 1.3), the build-ups form vertically stacked complexes (Figure 1.6B). Several authors (Elvebakk *et al.*, 2002, Rafaelsen *et al.*, 2003a, Carrillat *et al.*, 2005, Rafaelsen *et al.*, 2008) mentioned a relationship between location of the carbonate build-ups and position of faults.

Depending on the size of stacked build-ups and the resolution of seismic data, carbonate build-ups can be visible in seismic profiles. The focus of this thesis are the Upper Carboniferous – Lower Permian (Upper-Bashkirian – Lower-Sakmarian) carbonate build-ups of the Gipsdalen Group (Figure 1.3) at the Loppa High (Figure 1.1). Carbonates of the Gipsdalen Group were deposited in warm and arid climate during a period of high-frequency and high-amplitude glacioeustatic sea-level changes (Figure 1.7) (Stemmerik and Worsley, 1989).

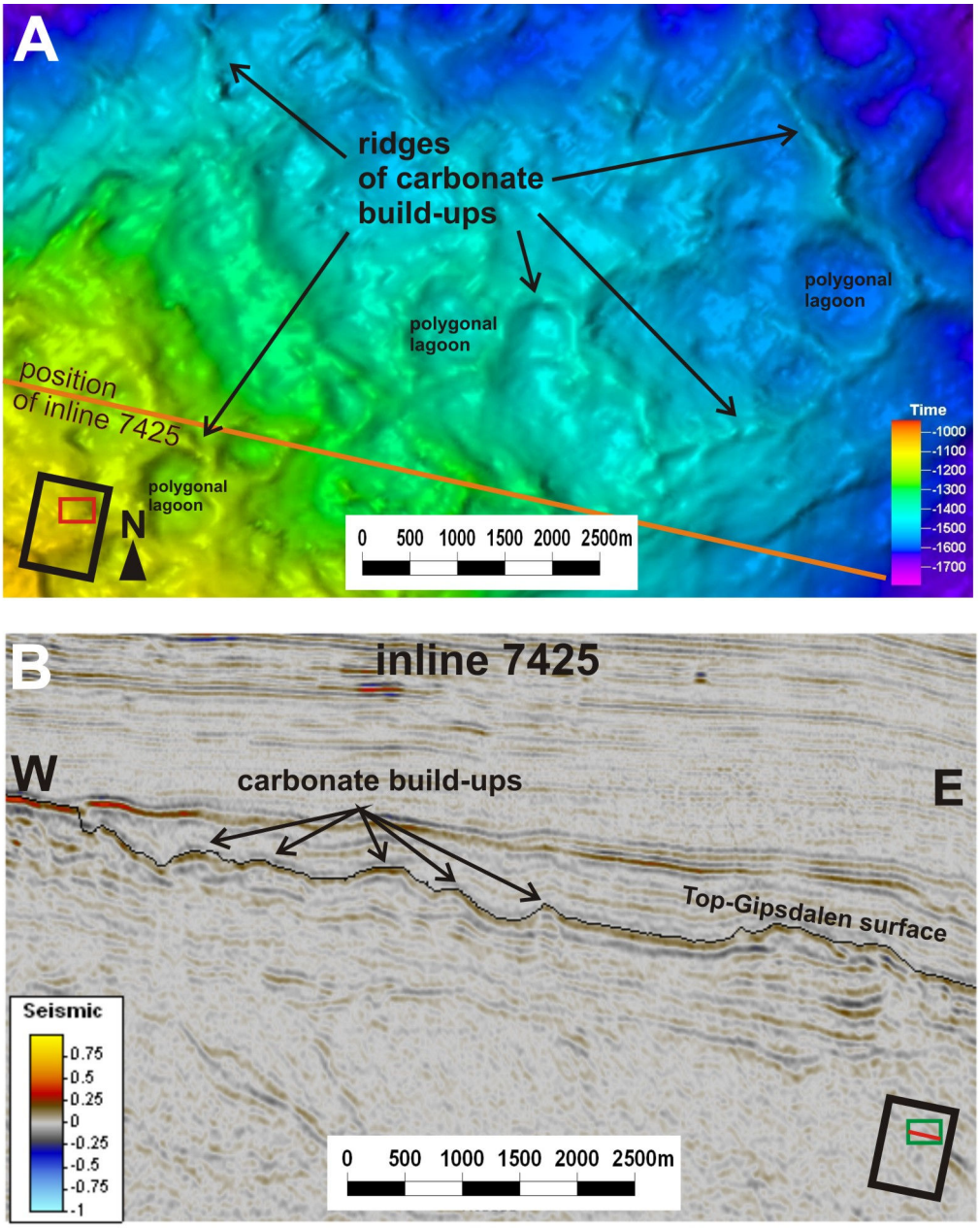

Figure 1.6 (A) Some interconnected ridges of carbonate build-ups and enclosed polygonal lagoons are indicated on the TWT-map view of the Top-Gipsdalen surface as well as the position of the seismic inline 7425. (B) Seismic inline 7425, displaying carbonate build-ups on the Top-Gipsdalen surface.

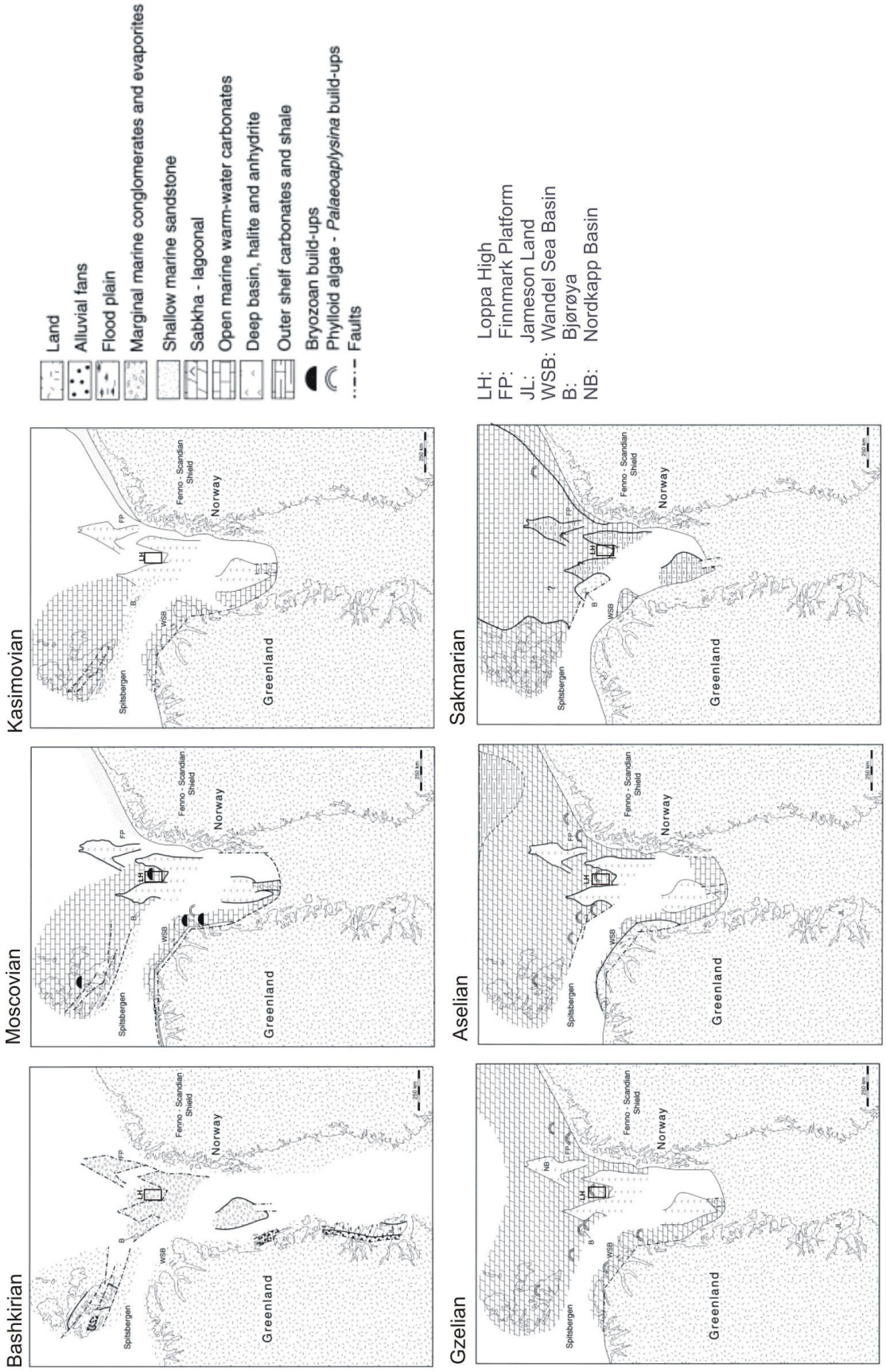

Figure 1.7 Paleogeography maps of the Barents Sea region during the deposition of warm water carbonates of the Gipsdalen Group (Bashkirian -Sakmarian) (Modified from Stemmerik, 2000).

1.3. Karstification

Karstification is a process of dissolution of carbonates and evaporites by water percolating through the rock as well as mechanical abrasion caused by the water flow and transported particles (Bates and Jackson, 1980).

Meteoric water, percolating through the soil, combines with CO_2 from organic matter, forming a weak solution of carbonic acid (Rafaelsen *et al.*, 2006). More acidic water causes faster dissolution of carbonate rocks. Water, flowing at the surface, enters fractures and faults in the rock and enlarges them by karstification process (Figure 1.8). The rate of the karstification processes is controlled by several factors: drainage area, structure and composition of the karstified rock, climate – particularly the amount of precipitation, and the amount of vegetation in the area (Rafaelsen *et al.*, 2006). The karstification process creates karst topography such as dolinas (sinkholes) (Figure 1.8), karren (channels of furrows) and mogotes (karst towers in tropical areas) on the surface, and shafts, caves (Figure 1.8) and drainage systems in the subsurface (Bates and Jackson, 1980).

Figure 1.8 The result of karstification process in carbonate rocks, showing sinkholes, caves and a karstified fault. Water is draining through the rock enlarging the caves.

1.4. Lithostratigraphy

Lithostratigraphy of the Barents Sea area spans sequences from Upper Palaeozoic to Tertiary. The under-laying basement is composed of metamorphic rocks of Caledonian, equivalent to those exposed along the Norwegian coast, on the island of Bjørnøya and on Svalbard (Worsley *et al.*, 1986, Harland *et al.*, 1997, Larssen *et al.*, 2002).

The Upper Palaeozoic succession, which is the target of this thesis, contains 4 major groups. These groups are the siliciclastic-dominated Upper Devonian – Lower Carboniferous Billefjorden Group, the Upper Carboniferous – Lower Permian warm-water carbonates and minor siliciclastics dominated Gipsdalen Group, the temperate-water carbonates dominated mid-Permian Bjarmeland Group and the cool-water carbonates, cherts and siliciclastics dominated Upper Permian Tempelfjorden Group (Figure 1.3). The boundaries between them reflect significant changes in climate, sea-level and tectonic regime (Larssen *et al.*, 2002, Stemmerik and Worsley, 2005). The change in palaeoclimate reflects the northward movement of the Barents Sea area from the humide equatorial tropical zone in the Early Carboniferous, through the northern arid climatic belt during the Middle Carboniferous to Early Permian, and through the temperate to cool water zone in the Middle Permian (Steel and Worsley, 1984, Worsley *et al.*, 1986, Stemmerik and Worsley, 1989, Stemmerik and Worsley, 2005).

1.4.1. Billefjorden Group

The term “Billefjorden Group” was introduced by Cutbill & Challinor (1965). Billefjorden Group (Figure 1.3) is a suite of predominantly non-marine sediments now recognised to be of Late Devonian to Early Carboniferous age (Larssen *et al.*, 2002). It is a well-established lithostratigraphic unit and its depositional evolution and overall facies development is well known (e.g. Steel and Worsley, 1984). The type area of this group is in Billefjorden in central Spitsbergen with thickness of 2500 m (Dallmann *et al.*, 1999). The offshore development of the group is similar to the onshore one on Spitsbergen with one major exception in the southeastern Finnmark

Platform: the upper part of the group includes some shallow marine deposits (Larssen *et al.*, 2002).

The the Billefjorden Group offshore is best mapped on the Finnmark Platform, where it is represented by three formations (Figure 1.3): the Soldogg Formation, the Tettegras Formation and the Blærerot Formation (Larssen *et al.*, 2002). Main lithologies in this group are: medium- to coarse-grained, occasionally conglomeratic sandstones and minor siltstones and coals represented by the Soldogg Formation; stacked metre-scale fining-upward cycles of sandstone, siltstone, claystone and coal redpresented by Tettegras Formation and basal unit of fossiliferous limestones, overlain by marine shales and fine- to medium-grained, fluvial and shallow marine sandstones represented by Blærerot Formation (Larssen *et al.*, 2002). Sediments of the Billefjorden Group are separated from the underlying basement rocks by an angular unconformity.

According to Larssen et al. (2002) the red-bed sequences on the Loppa High are tentatively assigned to this group, but need further investigation. The succession on the Loppa High (Figure 1.3) represents deposition in alluvial fans and proximal braided river systems in a rapidly subsiding sub-basin. Volcanoclastic material in well 7120/2-1 (Figure 1.1) is suggesting local volcanic activity.

1.4.2. Gipsdalen Group

The term Gipsdalen Group was introduced by Cutbill and Challinor (1965) for a suite of rocks of mid-Carboniferous to early Permian age (Figure 1.3). The type area of this group is in central Spitsbergen, where it is widely exposed (Larssen *et al.*, 2002). The group's geological development is well known onshore, on Spitsbergen (e.g. Steel and Worsley, 1984, Dallmann *et al.*, 1999) and on Bjørnøya (e.g. Worsley *et al.*, 2001).

Offshore succession in the southern Norwegian Barents Sea (Figure 1.3) is dominated by red-coloured siliciclastics and warm-water, often dolomitized carbonates – also with the significant presence of evaporites and the halite diapirs in

the Nordkapp Basin (Larssen *et al.*, 2002). Warm-water dolomitized carbonates of this group on Loppa High are in the centre of interest of this thesis.

The thickest drilled succession of Gipsdalen Group is from the southern flanks of the Loppa High, where it is more than 1000 m thick in well 7121/1-1 (Figure 1.1) and seismic data suggest that the succession continues even 500 m deeper (Larssen *et al.*, 2002). In contrast, the Gipsdalen Group sediments are totally absent on the crest of the Loppa High (Figure 1.4).

The Gipsdalen Group is represented by three formations (Figure 1.3): Ugle, Falk and Ørn.

The Gipsdalen Group (Figure 1.3) was decribed by Larssen et al. (2002). The group is composed of several-metre thick rhythmic units showing the trend of upward shallowing, deposited during a period of high-frequency and high-amplitude glacioeustatic sea-level changes (Figure 1.7) (Stemmerik and Worsley, 1989). The basal part of the succession is dominated by continental red bed sandstones, siltstones and conglomerates (Ugle Formation). These are overlaid by mixed carbonates of shallow marine facies and siliciclastics (grey-coloured marine sandstones), conglomerates and shales (Falk Formation). The upper part of the group is dominated by rhythmically bedded limestones and dolomites with Palaeoaplysina build-ups, and minor evaporites on the platform areas (Ørn Formation). Seismic data from Loppa High show that build-ups form several hundred metre thick, stacked successions in the deeper ramp areas (Elvebakk *et al.*, 2002).

The boundary between the Gipsdalen Group and the underlying Billefjorden Group is represented by a major regional unconformity, associated with a significant change in palaeoclimate from warm and humid to warm and arid to semi-arid (Steel and Worsley, 1984, Stemmerik and Worsley, 1989, Stemmerik, 2000).

1.4.3. Bjarmeland Group

The group was introduced by Dallmann *et al.* (1999). According to Gabrielsen et al. (1990), Bjarmeland was also used before to name a structural element on the

Barents Shelf: the Bjarmeland Platform (Figure 1.1A). The Bjarmeland Platform is also defined as type area for this group (Larssen *et al.*, 2002). The maximum confirmed thickness of the group is 488 m in well 7121/1-1 (Figure 1.1) at the south-eastern flank of the Loppa High (Larssen *et al.*, 2002).

Lithology of the Bjarmeland Group (Figure 1.3) is dominated by white to light grey bioclastic limestones, containing a typical cool-water fauna, and also silty, dark grey to black limestones characteristic for the deeper-water succession. In the shallow environment were deposited shelf bioclastic grainstones, and in deeper outer shelf bryozoans-dominated cool-water carbonate build-ups and thinly bedded bioclastic wackestones and packstones (Larssen *et al.*, 2002).

The Bjarmeland Group is represented by three formations (Figure 1.3): the Polarrev, the Ulv and the Isbjørn. The Polarrev Formation represents the cold-water carbonate build-ups and the Ulv Formation represents the inter-build-up lithofacies interfingering the build-ups (Larssen *et al.*, 2002). The uppermost Isbjørn Formation was developed in inner shelf areas. It overlies earlier build-ups but does not extend into deeper waters characteristic of the Ulv Formation (Larssen *et al.*, 2002).

1.4.4. Tempelfjorden Group

The term Tempelfjorden Group was introduced by Cutbill & Challinor (1965) for a suite of spiculites, spiculitic chert, silicified skeletal limestones and fine-grained siliciclastics of mid- to late Permian age (Figure 1.3). The type area of this group is in the innermost part of Isfjorden in central Spitsbergen (Larssen *et al.*, 2002). Several areas offshore illustrate a quite significant variations in the group's development: the southern Loppa High – Hammerfest Basin, the Bjarmeland Platform and the eastern Finnmark Platform (Figure 1.3) (Larssen *et al.*, 2002).

The facies, development and depositional evolution of the Tempelfjorden Group have been described by Steel & Worsley (1984) and Ezaki *et al.* (1994). The Tempelfjorden Group has the maximum confirmed thickness of 901 m, in well on the southern margins of the Hammerfest Basin (Larssen *et al.*, 2002). On the Loppa

High, the succession thins and is then truncated up-flank, reflecting repeated uplift in the Permian to Early Triassic (Larssen *et al.*, 2002).

The Tempelfjorden Group was deposited during an overall transgression, representing deposition in cool-water, temperate shelf and basinal environments (Larssen *et al.*, 2002). Two formations are assigned to the Tempelfjorden Group (Figure 1.3): the Røye Formation and the Ørret Formation.

2. Data and methods

2.1. Data

The data for this thesis were provided by Det norske oljeselskap, Harstad.

- The main dataset is the northern part of the 3D seismic survey SG9810 (Figure 2.1), acquired by SAGA PETROLEUM AS in 1998. Data were processed by GECO-PRAKLA in January 1999. The dataset contains full-stacked final migrated seismic data in SEG-Y format. The sampling interval was 4 ms, the streamer depth 6 m, and the acquisition grid: $\Delta x \times \Delta y$ = 12.5 m × 37.5 m. The calculated seismic resolution in the carbonates of the Gipsdalen Group is 42 m.

- The second dataset is the high resolution 3D seismic site survey NH0372 (Figure 2.1). The acquisition grid was: $\Delta x \times \Delta y$ = 6.25 m × 12.5 m, and the streamer depth 3 m. The calculated seismic resolution in the carbonates of the Gipsdalen Group is 23 m.

- One well, located inside both 3D surveys, SG9810 and NH0372, was used in this thesis. According to NPD (2009), well 7220/6-1 (Figure 2.1, Figure 1.4) was drilled in 2005 by Norsk Hydro Produksjon AS. The well is 1540 m deep and penetrates into metamorphic rocks assigned to the Caledonian orogeny. It is considered a dry well with oil shows in carbonates of the Gipsdalen Group.

- The stacking velocity cube from the area of the 3D seismic survey SG9810 was used to create a velocity model. The grid size of the stacking velocity cube is 525 m × 525 m.

2.2. Methods

The data analysis was carried out using Petrel™ 2009 PC software, at the University of Tromsø. Petrel™ 2009, of Schlumberger, is seismic-to-simulation software, an integrated workflow tool for geoscientists (Schlumberger, 2009b). Methods applied for the analysis of the data are listed below.

- Testing and customizing of the Ant-tracking algorithm workflow and its application to both the study area of 3D seismic survey SG9810 and the high

resolution site survey NH0372, for the recognition of faults and fractures connected to Palaeozoic warm water carbonate build-ups of the Gipsdalen Group at the Loppa High.

- 3D visualization of the results of the Ant-tracking algorithm workflow - faults and fractures connected to Palaeozoic warm water carbonate build-ups of the Gipsdalen Group at the Loppa High.
- Seismic interpretation of the main horizons in the study area of survey SG9810 to be used in a velocity model.
- Creating the velocity model, using stacking velocity cube from the area of seismic survey SG9810 and the main interpreted seismic horizons.
- Depth conversion of the main seismic horizons and the seismic cube SG9810 using the created velocity model.
- Comparison of the results from the study area of survey SG9810 with the results from the high resolution site survey NH0372.

The main methods: the Ant-tracking algorithm workflow, the 3D visualization of the results and the velocity modelling and the depth conversion are described in more detail in the following chapters.

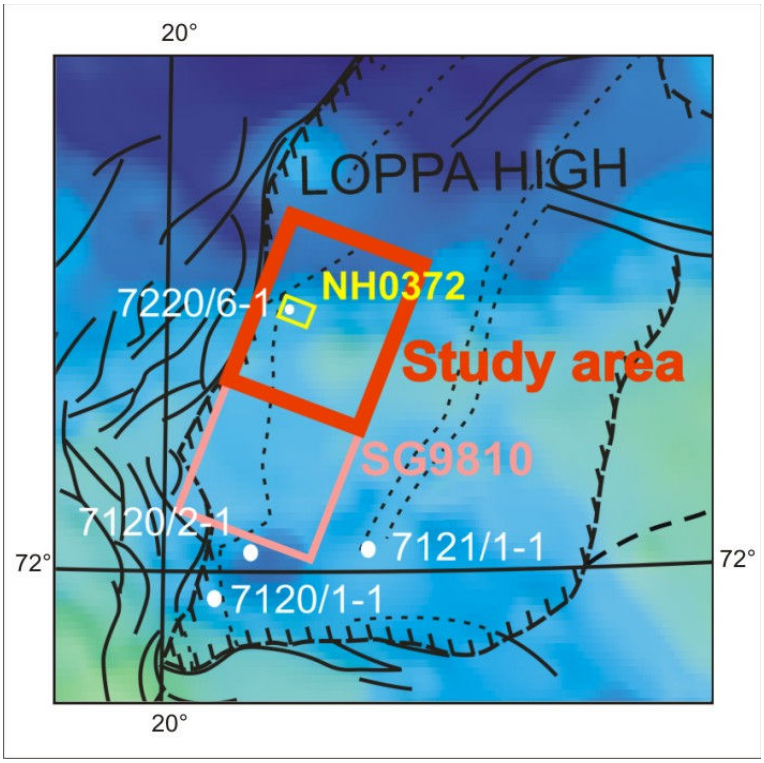

Figure 2.1 Positions of 3D seismic surveys SG9810 and NH0372 (site survey), study area and four wells are indicated on the Loppa High.

2.3. Ant-tracking

Ant-tracking, a patent-protected technology from Schlumberger, is used for identification and automatic extraction of faults and fractures from a pre-processed seismic volume (Schlumberger, 2009b, Schlumberger, 2009a, Pedersen *et al.*, 2002). It is a unique innovative algorithm based on behaviour of virtual ant colonies, which are using their pheromones to mark their paths in order to optimize their search for food (Schlumberger, 2009b).

Similarly (after Pedersen *et al.*, 2005), virtual ants are placed in seismic volume to look for fault zones. A large number of ants is evenly distributed in the volume. They are programmed to move along what appears to be a fault zone, while emitting 'pheromone'. If they get to the area, which does not fulfil conditions for fault zone, they are terminated. This way, the surfaces fulfilling pre-programmed conditions will be traced by many ants coming from different initial positions and therefore enhanced, sharper and more continuous.

It is important to keep in mind that Ant-tracking will not only enhance faults and fractures in the data, but also other discontinuities such as different chaotic responses, internal amplitude variations, processing effects and other (Pedersen *et al.*, 2005). That is why the preconditioning of the data is important. Depending on what in the data needs to be enhanced, parameters in the Ant-tracking algorithm workflow would differ. To get the best results, testing of parameters and their combinations is inevitable.

After application of the Ant-tracking attribute cube, the last step of the Ant-tracking algorithm workflow used in this thesis, Petrel^{TM} 2009 offers an option of Automatic fault extraction process. It is a set of interactive tools to display, analyze and edit extracted fault-patches (Schlumberger, 2009b). This is a very good tool for extracting major faults in the area. However, in this case, we want to concentrate on minor faults and fractures, and Automatic fault extraction process removes minor details from the Ant-tracking result. Therefore, faults and fractures, connected to Palaeozoic warm water carbonate build-ups of the Gipsdalen Group at the Loppa High, will be visualized directly from the results of the Ant-tracking algorithm workflow.

2.3.1. Ant-tracking algorithm workflow – explanations and definitions

The Ant-tracking algorithm workflow consists of several steps which are meant to pre-condition the data. The last step is the Volume Attribute cube of Ant-tracking algorithm itself. The input for the Ant-tracking Attribute Cube should be an edge enhanced volume, such as Chaos or Variance attribute cube (Schlumberger, 2009b). It is possible to apply Ant-tracking cube directly to the seismic data, but that would not generate the desired result.

Main steps of Ant-tracking algorithm workflow:

1. Cropping and Realizing the Seismic cube
2. Graphic Equalizer Attribute cube *(optional)*
3. Structural Smoothing Attribute cube
4. Variance or Chaos Attribute cube *(edge detection method)*
5. Ant-tracking Attribute cube

In each of these steps are several parameters, which can be set or kept default. To achieve the best results, it is necessary to test these parameters and their combinations, according to given seismic data and the information we wish to extract from them. The main steps of the Ant-tracking algorithm workflow are explained in detail below.

2.3.1.1. Cropping and Realizing the Seismic cube

The Ant-tracking algorithm is an intensive process for the computer-processor (Schlumberger, 2009b). Therefore, the seismic cube must be realized in the first step. Realization is a process, which creates a physical copy of seismic data in ZGY bricked seismic format (Schlumberger, 2009b). Realization increases memory-loading speed and converts 32-bit cube to 16 or 8-bit format.

For testing of parameters of the Ant-tracking algorithm workflow, the main seismic cube must be cropped to a small volume (Figure 2.2). This greatly spares time of the testing. Only after deciding the final parameters, the time-consuming Ant-tracking algorithm workflow can be applied to the whole realized seismic cube.

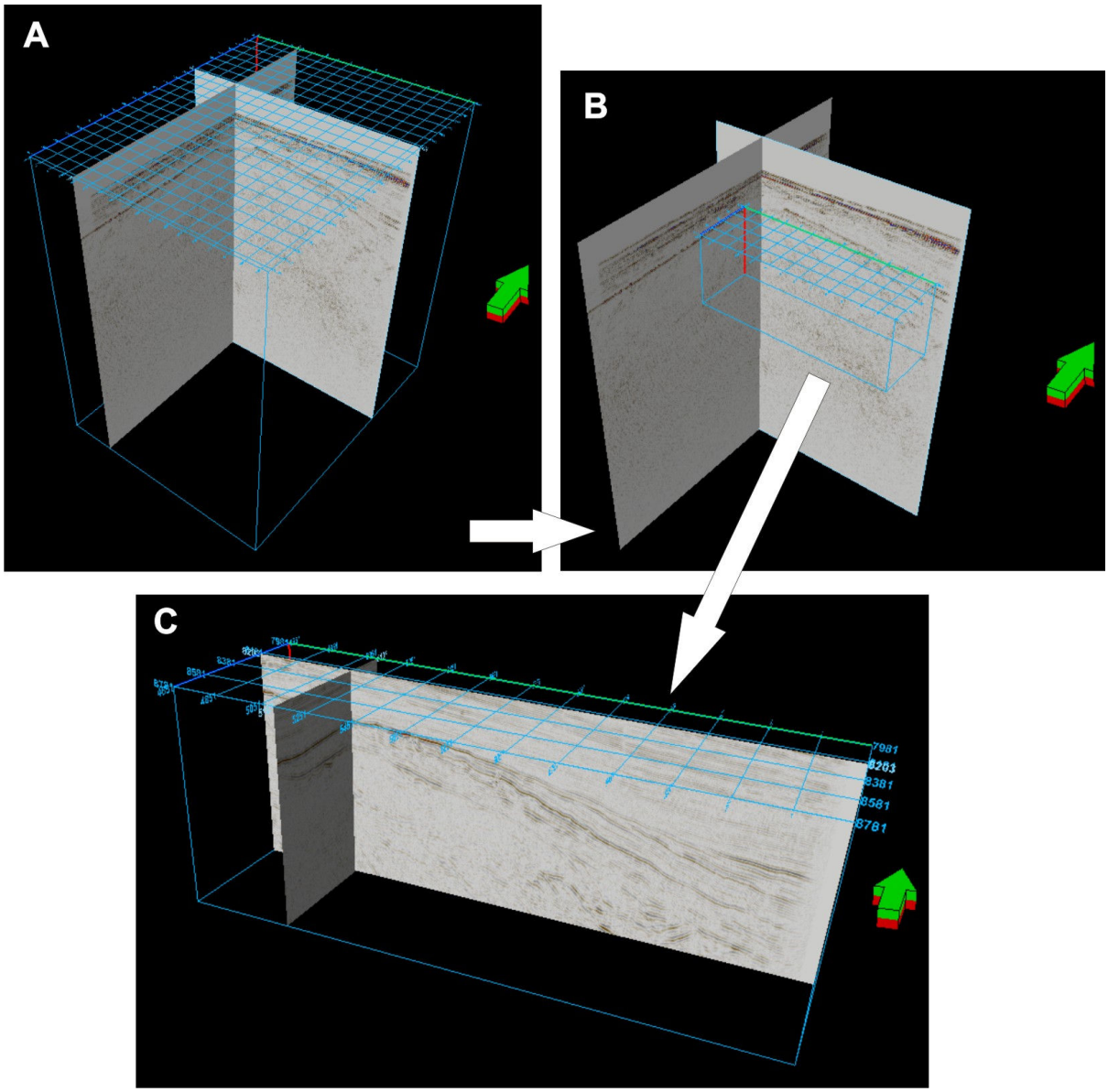

Figure 2.2 (A) The seismic cube of the study area. (B) Cropping smaller seismic volume for testing of the Ant-tracking workflow. (C) Zoomed cropped and realized seismic volume.

2.3.1.2. Graphic equalizer Attribute cube

The Graphic equalizer attribute cube (Figure 2.3B) enhances or reduces the selected frequency component of the input signal. It can be used to apply high, low or band-pass filters to the input seismic volume (Schlumberger, 2009b) if necessary.

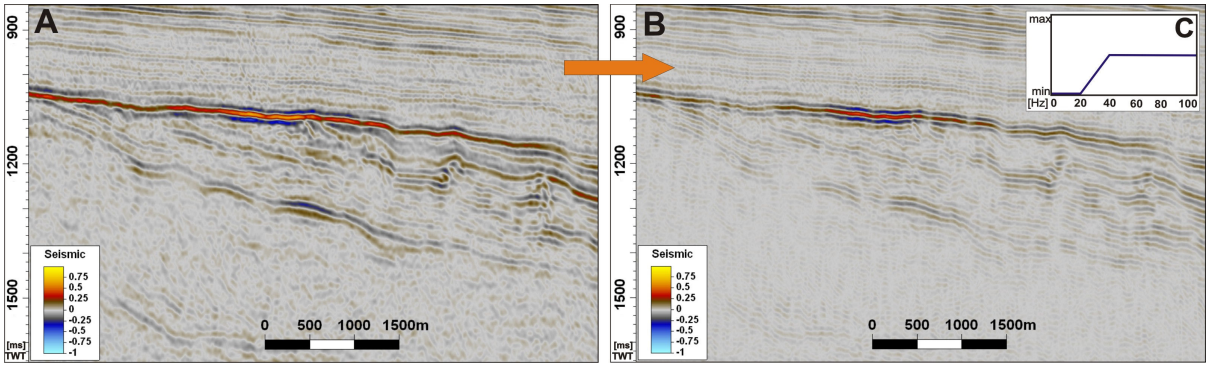

Figure 2.3 (A) Original seismic data. (B) Filtered seismic data. (C) Applied filter removing the low frequencies.

2.3.1.3. Structural smoothing Attribute cube

The Structural smoothing (Figure 2.4B) is a smoothing of the input seismic data, guided by the local structure, for increasing the continuity of the seismic reflections (Schlumberger, 2009b). Structural smoothing attribute has optional parameters available for sharpening the discontinuities: Dip-guide and Enhance edge. The Dip-Guide performs the smoothing parallel to local structural orientation estimate and the Enhance edge performs the smoothing by two half filters and removes only more chaotic signal to enhance edges in the seismic data. The size of the filter can be defined independently for each orientation by Inline, Crossline and Vertical scale parameters (0 – 5.0, default 1.5).

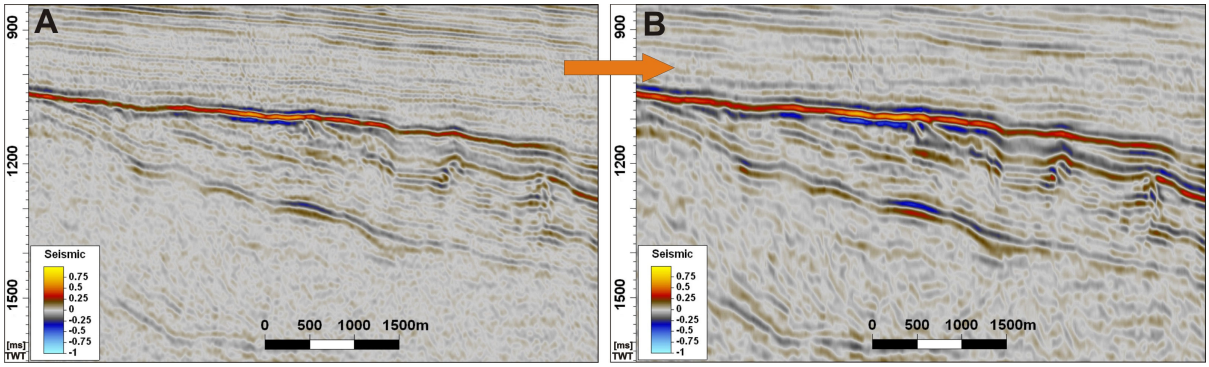

Figure 2.4 (A) Original seismic data. (B) Seismic data after the application of the Structural smoothing.

2.3.1.4. Variance and Chaos Attribute cubes

The Variance Attribute cube (Figure 2.5A) is an edge detection method. It estimates the local variance in the seismic signal (Schlumberger, 2009b). The size of the filter can be defined independently for each orientation by the Inline and the Crossline range parameters (1 – 11, default 3) and by the Vertical smooth parameter (0 – 200 ms, default 15 ms).

The Chaos Attribute cube (Figure 2.5B) is an edge detection method and computes the local chaos – measure of the 'lack of organization' in the dip and azimuth estimation method. It can be used to enhance faults and discontinuities (Schlumberger, 2009b). There are no optional parameters to choose when applying this attribute cube.

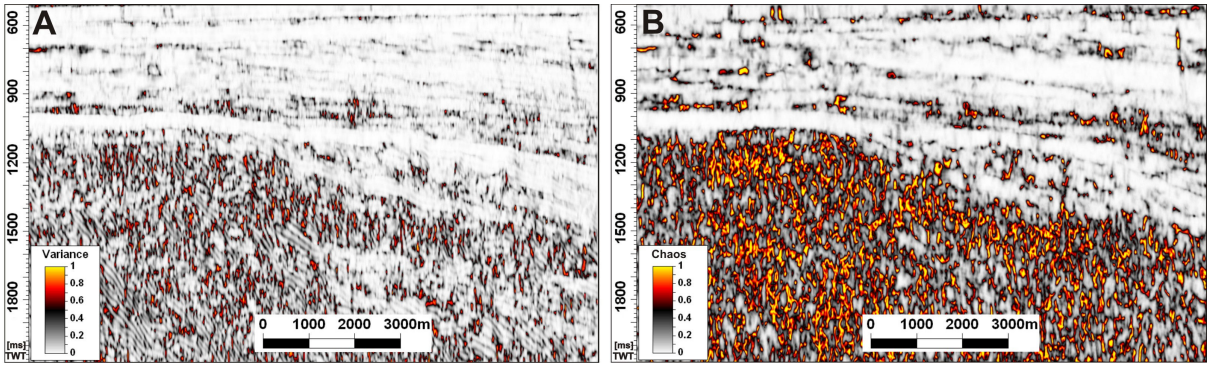

Figure 2.5 (A) A seismic line after application of the Variance attribute cube. (B) A seismic line after application of the Chaos attribute cube.

2.3.1.5. Ant-tracking Attribute cube

The Ant-tracking algorithm is used for automatic extraction of faults and fractures (Figure 2.6) from a pre-processed seismic volume (Schlumberger, 2009b). There are several parameters available in the Ant-tracking algorithm: Initial ant boundary, Ant track deviation, Ant step size, Illegal step allowed, Legal steps required and Stop criteria [%]. The Initial ant boundary (1 – 30) controls how closely the ants are deployed within the volume. Larger the number is, fewer ants are deployed and less detail is captured. The Ant track deviation (0 – 3) allows the ants to search on sides of their tracking direction. A larger value allows finding more connections. The Ant step size (2 – 10) defines increment within each step. Higher value lowers the

resolution of the result. The Illegal step allowed (0 – 3) defines how many steps is an ant allowed to search without detecting an edge zone. A larger value allows finding more connections. The Legal steps required (0 – 3) describes a number of required legal steps after an illegal step. Lower value is less restrictive and allows finding more connections. The Stop criteria [0 – 50%] controls the termination of ants after taking too many illegal steps. Larger value allows the ants to advance further.

There is an option of choosing the 'Passive ants' or the 'Aggressive ants' parameter. This option gives 2 different defaults of above mentioned parameters: the Passive ants default (Initial ant boundary = 7, Ant track deviation = 2, Ant step size = 3, Illegal step allowed = 1, Legal steps required = 3 and Stop criteria = 5 [%]) and the Aggressive ants default (Initial ant boundary = 5, Ant track deviation = 2, Ant step size = 3, Illegal step allowed = 2, Legal steps required = 2 and Stop criteria = 10 [%]). Depending on the data and the objective, one of above two options or customized settings can be chosen. The 'Passive ants' are suitable for finding only major regional faults. On the other hand, the 'Aggressive ants' find both major and subtle faults and fractures.

The Orientation Control for Ant-tracking is achieved by using the Stereonet, another available parameter. In the Stereonet, it is possible to restrict or allow chosen dips and azimuths of ants' paths. This makes the ants to search for discontinuities only in preferred orientation, depending on the objective of the search.

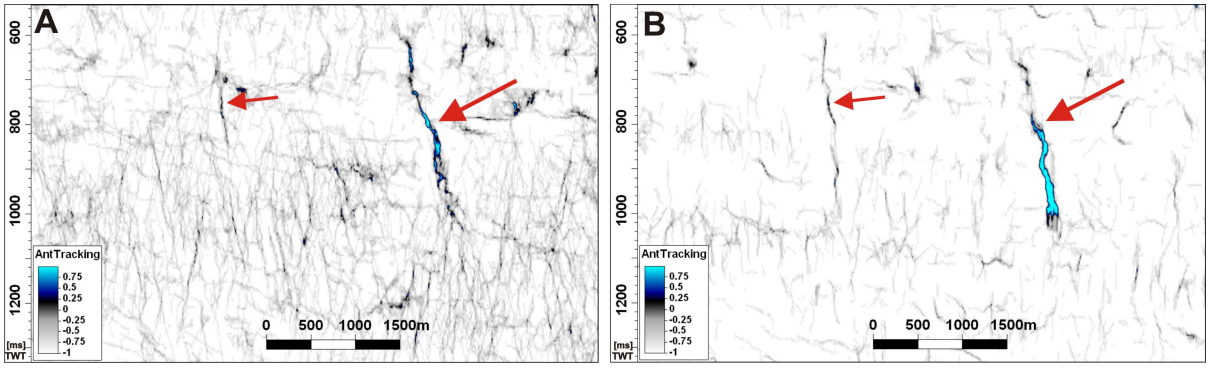

Figure 2.6 Two examples of the results from the Ant-tracking workflows. (A) The Ant-tracking result from the Variance cube. Allowed dips are 20-80°. (B) The Ant-tracking result from the Chaos cube. Allowed dips are 20-90°. The red arrows are indicating the same faults, detected by the two Ant-tracking workflows with different parameters.

All the final parameters chosen for the case of this thesis can be found in *3.1 Ant-tracking algorithm workflow – chosen parameters*.

2.4. Three dimensional visualization of the results of the Ant-tracking algorithm workflow

The faults and fractures connected to carbonate build-ups of the Gipsdalen Group are visualized in three dimensions (3D). In the 3D window, the whole seismic cube is viewed. In order to visualize only one fault, the result of the Ant-tracking algorithm workflow is cropped to a small volume (Figure 2.7A) - containing one build-up and one connected fault. The Ant-tracked data are rendered (Figure 2.7B) and the opacity is chosen so, that only the maximum positive values of the data are visible (Figure 2.7C). This is showed on the background of a seismic line to visualize position of the build-up and the associated fault in the data (Figure 2.7C). Volume Rendering is a direct three dimensional visualisation of a seismic volume, so that all the seismic data are displayed simultaneously (Figure 2.7B). High ant-tracking values indicate the strongest discontinuity, if these are opaque and the low ant-tracking values are transparent (by customizing the opacity), the faults are made visible in three dimensions (Figure 2.7C).

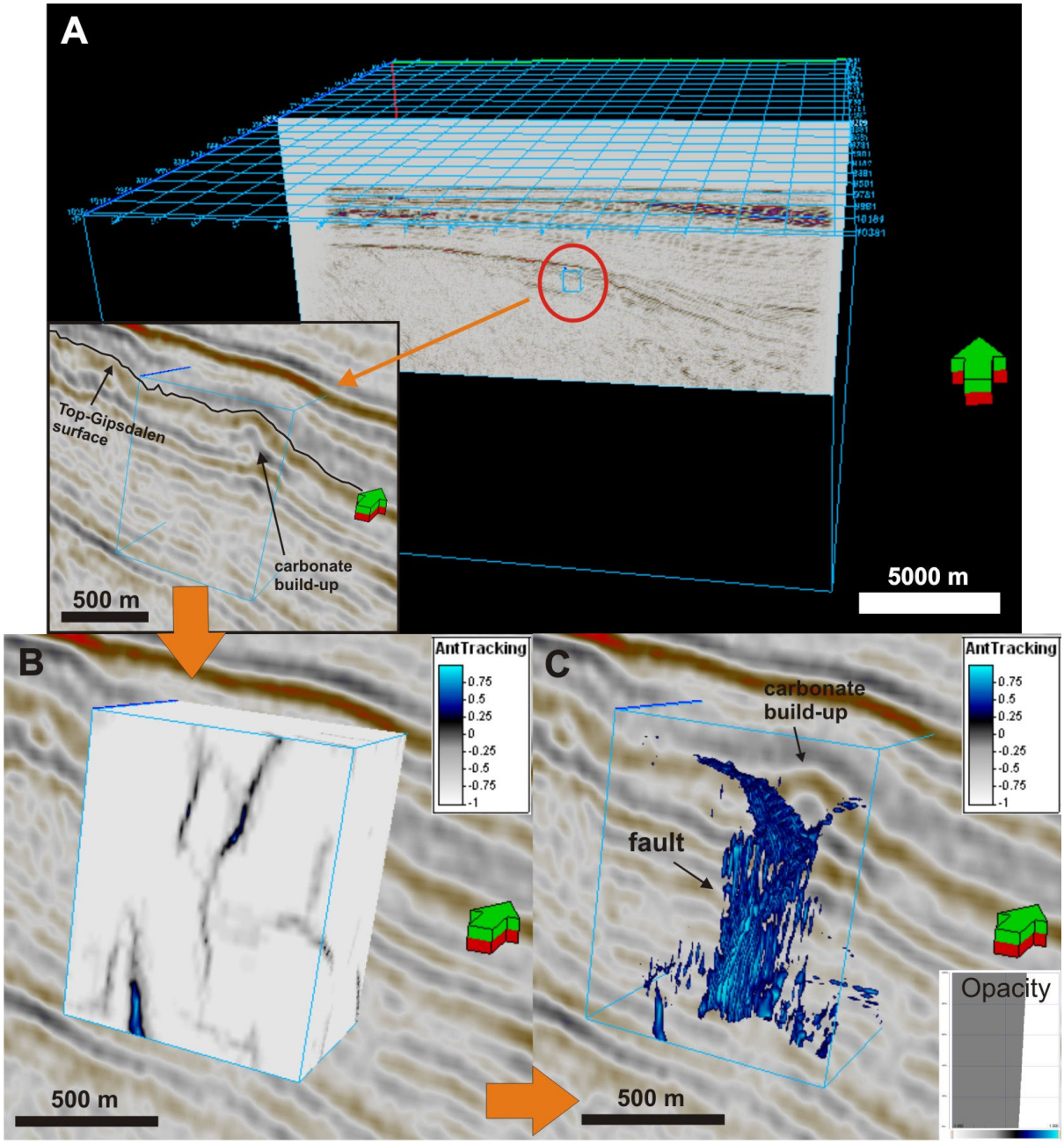

Figure 2.7 (A) Whole seismic cube of the study area. Position of the chosen carbonate build-up is indicated by the red circle. Detail of the cropped volume is showed in the zoomed picture. (B) Rendered cropped cube. (C) Rendered cropped cube with opacity settings applied as indicated.

2.5. Velocity modelling and depth conversion

The depth conversion is a conversion of the z-axes of seismic data from two-way-travel time [ms] to metres [m] (Figure 2.8). To do this, a velocity model is needed (Figure 2.9). In the Petrel^{TM} 2009 software, there are several approaches available depending on the input data. The input for the velocity model, created in this case,

was the stacking velocity cube (Figure 2.9C, Figure 2.10), six interpreted seismic surfaces (Figure 2.9A, Figure 2.10) and three well tops from the well 7220/6-1 (Figure 2.9B, Figure 2.10).

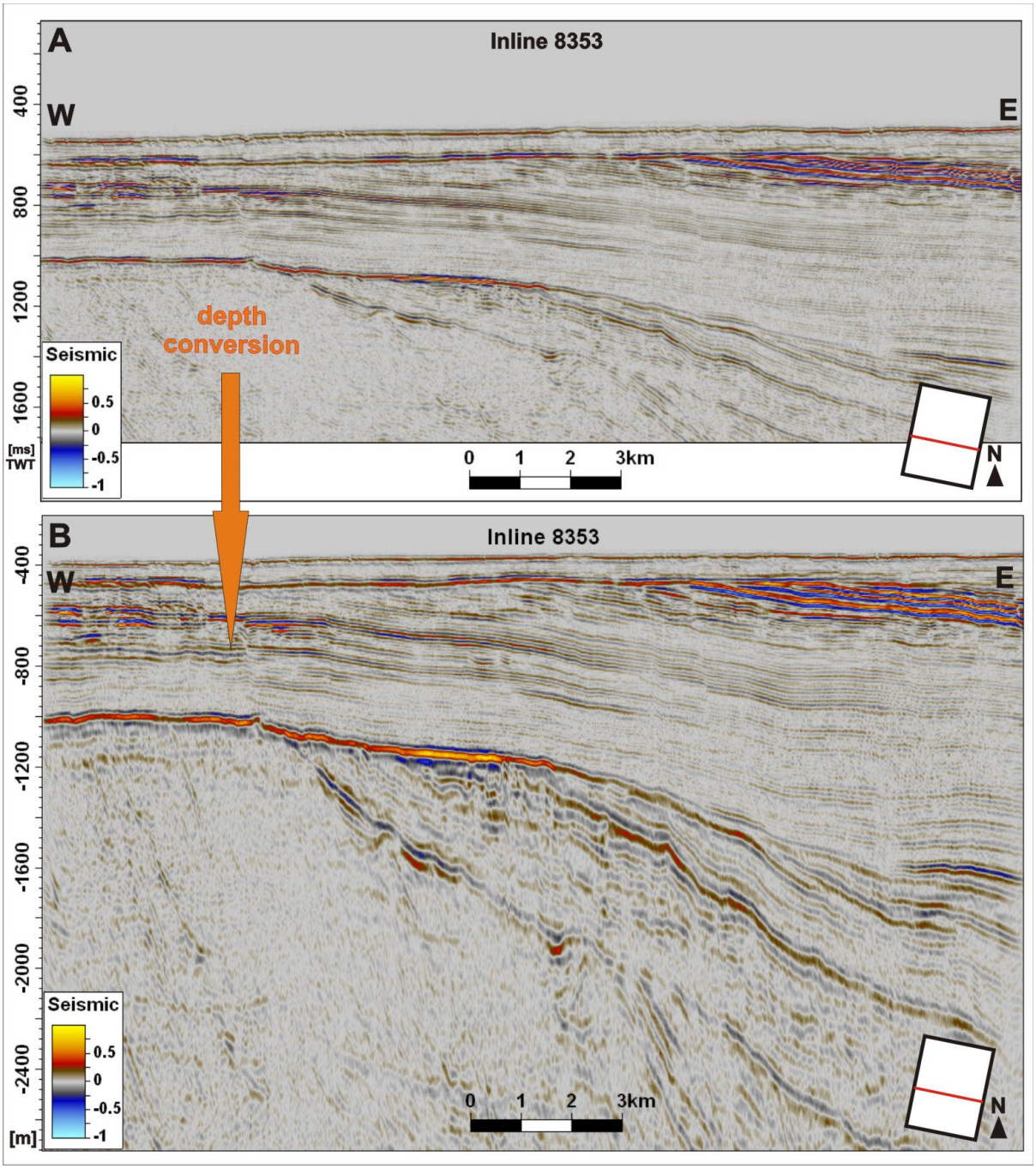

Figure 2.8 (A) Original seismic data in milliseconds, two-way-travel time. (B) Depth converted seismic data in metres.

Velocity Model

A	Base		B	Correction		C	Model	
	Surface	seafloor	Well tops	SEABED (Well tops NPD)		V=V0=Vint	V0: Surface	Interval
	Surface	Top-Triassic	None			V=V0=Vint	V0: Surface	Interval
	Surface	Intra Snadd	None			V=V0=Vint	V0: Surface	Interval
	Surface	top Paleozoic	Well tops	GIPSDALEN GP (Well tops NPD)		V=V0=Vint	V0: Surface	Interval
	Surface	top Gibsdale	None			V=V0=Vint	V0: Surface	Interval
	Surface	top basement	Well tops	BASEMENT (Well tops NPD)		V=V0=Vint	V0: Surface	Interval

Figure 2.9 The created velocity model. (A) Interpreted seismic surfaces as the base input. (B) Well tops corrections. (C) Model consisting of 'Interval velocity surfaces' calculated from both the stacking velocity cube and the seismic surfaces.

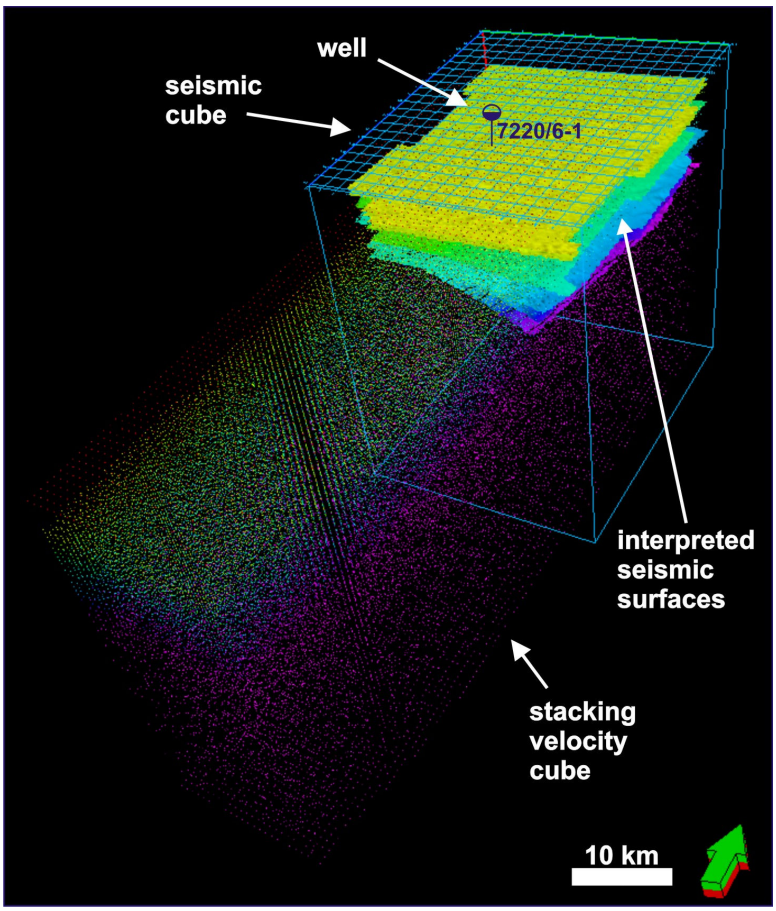

Figure 2.10 The figure is showing all the input data into the velocity model.

After the velocity model was created, the seismic data were depth converted by the 'General depth conversion process', using the created velocity model. Difference between the original [ms] and the depth converted [m] seismic line is showed in Figure 2.8.

3. Results

The main steps of the Ant-tracking workflow are suggested in the Petrel manual. However, these steps contain many parameters which may be customized. Also in one of the steps, when choosing the edge detection method, several different attribute cubes can be chosen. The most common are the Variance and the Chaos attribute cube. To extract faults and fractures associated with build-ups from the seismic data, the Ant-tracking workflow was customised to fit the situation. The testing of parameters was done by choosing different values for parameters in each of the main steps of the Ant-tracking workflow and analyzing how it changes the final result. The whole process was run over and over many times with different combinations of parameters, until it was possible to clearly recognise faults and fractures in the carbonates of the Gipsdalen Group.

The results of the main steps of the Ant-tracking algorithm workflow, with the final chosen parameters applied, are introduced in the following chapter.

3.1. Ant-tracking algorithm workflow – chosen parameters

The Ant-tracking workflow consists of several steps, which are meant to pre-condition the data before applying the Ant-tracking algorithm itself. These steps are in detail explained in *2.3.1. Ant-tracking algorithm workflow – explanations and definitions.* Here are introduced the final chosen parameters for the Ant-tracking workflow. Two sets of different parameters have been chosen to apply to the seismic data. The first set of parameters contains the Variance attribute cube and the second one contains the Chaos attribute cube. In the further text they will be referred to as 'Variance-Ant-tracking workflow' and 'Chaos-Ant-tracking workflow' respectively. A few of the chosen parameters in mentioned two sets slightly differ for the study area of SG9810 and for NH0372 survey (Figure 2.1). The aim was to achieve the best possible results, of fault and fracture detection and visualization, in both surveys. The NH0372 survey has higher resolution, a six times denser acquisition grid, and better data quality than the SG9810 survey. This may be the cause of differences in some of the parameters. The details are described below.

3.1.1. Variance – Ant-tracking workflow

To increase the continuity of seismic reflections, the data were structure-smoothed (Figure 3.1B, Figure 3.1E) in the first step and parameters: Dip-guide and Enhance edge were selected. When the Dip-Guide is selected, smoothing is performed parallel to local structural orientation estimate. When the Enhance edge is selected, smoothing is performed by two half filters and only more chaotic signal is removed, what enhances edges in the seismic data (Schlumberger, 2009b). The size of the filter was kept default.

To detect edges in the data, the variance attribute cube was applied in the second step. Only vertical smooth parameter was changed from the default to 8 ms in the study area of SG9810 survey (Figure 3.1C, Figure 3.3A) and to 10 ms in NH0372 survey (Figure 3.1F, Figure 3.3D). The optimum length of the vertical smooth parameter [ms] is data and objective dependent. Larger values of the parameter (up to 200 ms) reduce noise but also sharpness of the edges. In our case, we wanted to detect the edges, so low values have been selected. The testing showed that a value of 8 ms is the most suitable to use in the SG9810 survey (Figure 3.2A). The use of the same value, 8 ms, in the NH0372 survey (Figure 3.2C) did not give as good final result of the Ant-tracking workflow. Therefore to achieve a comparable good result, in both workflows, the vertical smooth parameter was set to a value of 10 ms (Figure 3.2B) in the NH0372 survey.

To extract faults from the data, the Ant-tracking attribute cube (Figure 3.3B, Figure 3.3E) was applied in the third step. The aim is to extract also minor faults and fractures, that is why the default parameters for the ‘Aggressive ants’ were chosen in this case. The Aggressive ants are able to find both major faults and subtle fractures, because their parameter-settings allow finding more connections in discontinuities in the data. To analyze the results correctly, it is desirable that faults and fractures in all directions and dips are found. However, testing showed that dips under 20° are allowing the ants to track artificial horizontal structures in areas of less pronounced seismic signal between two strong reflections, parallel to these reflections. Also, in survey SG9810 were detected many vertical structures, interpreted as artificial response, making the result unclear. Therefore the dips over 80° allowing the ants to track the vertical artificial response were restricted in this survey. In site survey

NH0372, most likely due to high resolution and good data quality, the Variance cube did not create same vertical artificial response. Even if many of the detected discontinuities were sub-vertical, after analyzing the whole result in three dimensions, it was possible to keep the allowed dips up to 90°. Therefore, the final Stereonet settings were adjusted to all azimuths: 0 - 360° but only dips: 20 – 80° for the study area of SG9810 (Figure 3.3B) and 20 – 90° for NH0372 survey (Figure 3.3E).

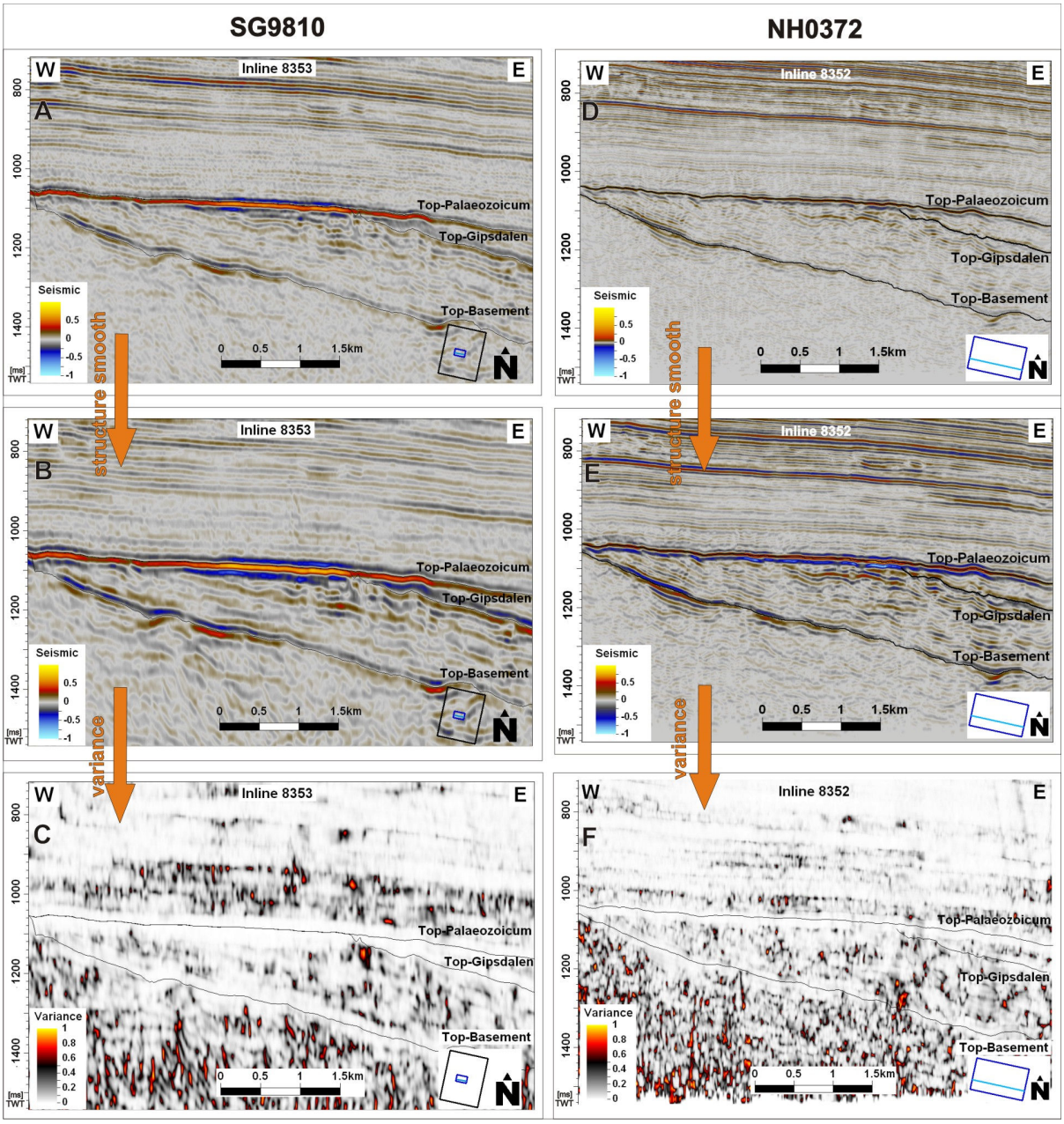

Figure 3.1 The first two steps of the 'Variance – Ant-tracking workflow' applied to seismic inline 8353 of SG9810 survey in B and C, and to seismic inline 8352 of high-resolution survey NH0372 in E and F. (A, D) Original seismic data. (B, E) Structure smoothed seismic data. (C, F) Seismic data after

application of the Variance attribute cube. The positions of the Top-Palaeozoicum, the Top-Gipsdalen and the Top-Basement surfaces are indicated.

To achieve a good quality of 3D visualization, the ant-tracked volume was ant-tracked once more (Figure 3.3C, Figure 3.3F), in the last step of the workflow. It enhanced the amplitudes of the previous result from the Ant-tracking workflow. The final result became clearer and the amplitudes stronger. In this case, it was desirable to enhance the result only slightly, so the artificial response, which often has lower amplitude values, would not get too enhanced and superimpose the result. The Passive ants are suitable for finding only major faults. This makes them also suitable for this case. The default parameters for the 'Passive ants' were applied and the Stereonet settings were kept unchanged from the previous step.

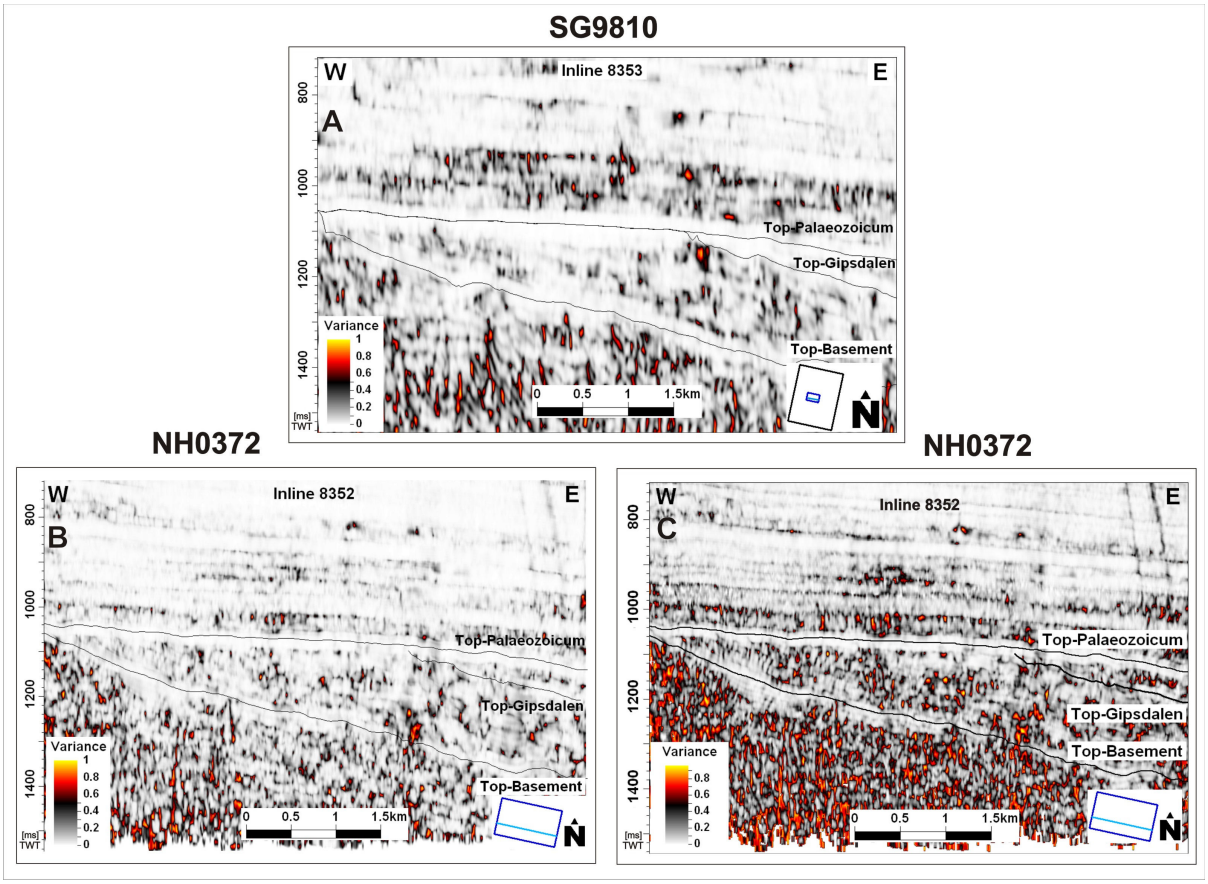

Figure 3.2 Seismic data after application of the Variance attribute cube. Comparison of an effect of the Variance attribute cube when different vertical smooth parameter is set. (A) 3D seismic survey SG9810. The vertical smooth parameter is set to 8 ms. (B) High resolution 3D seismic survey NH0372. The vertical smooth parameter is set to 10 ms. (C) High resolution 3D seismic survey NH0372. The vertical smooth parameter is set to 8 ms.

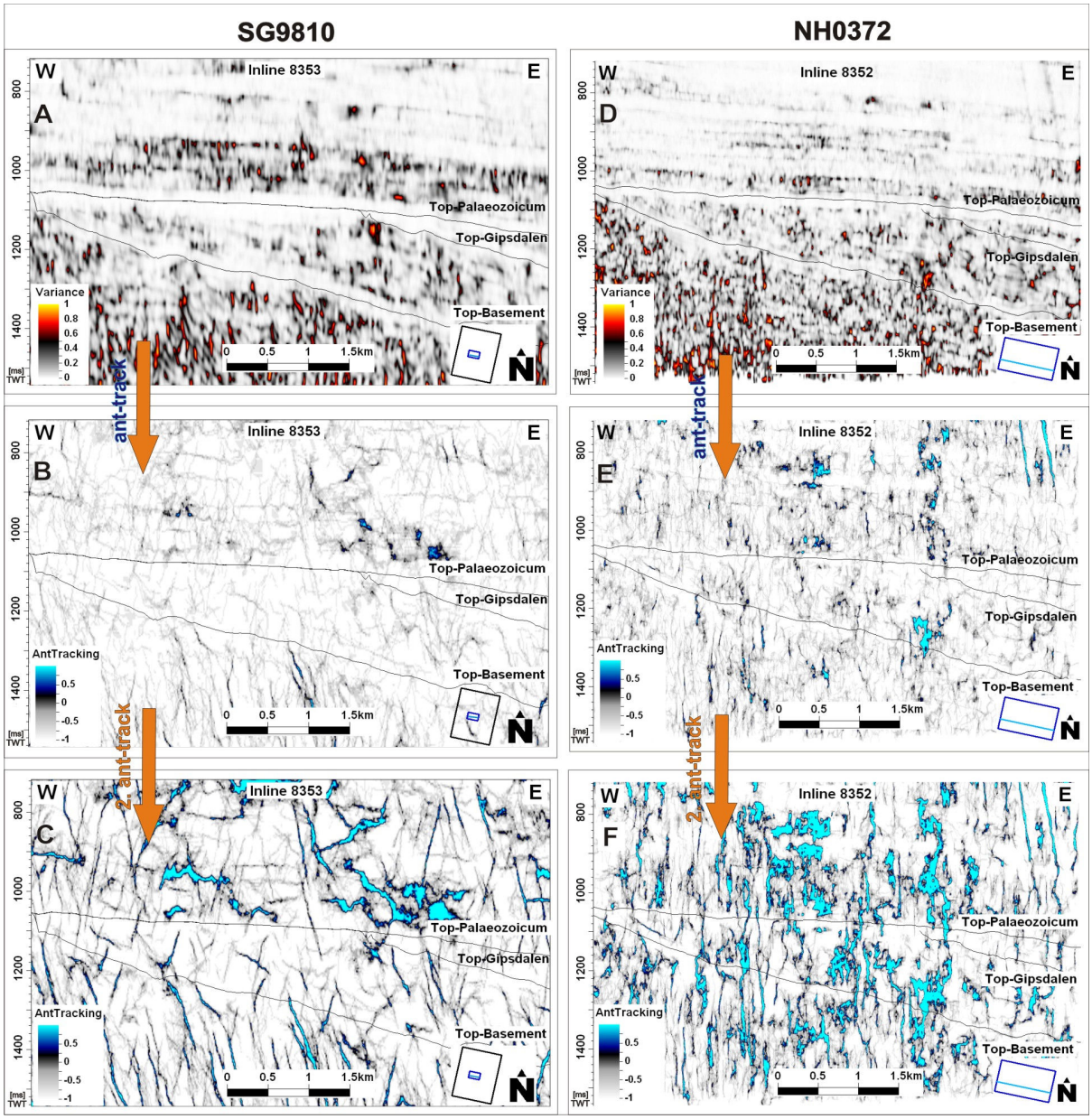

Figure 3.3 The last two steps of the 'Variance – Ant-tracking workflow' applied to the seismic inline 8353 of survey SG9810 in B and C, and to the seismic inline 8352 of high-resolution site survey NH0372 in E and F. (A) Seismic data after application of the Variance attribute cube. (B) Ant-tracked seismic data, aggressive ants. (C) Second time ant-tracked seismic data, passive ants. (D) Seismic data after application of the Variance attribute cube. (E) Ant-tracked seismic data, aggressive ants. (F) Second time ant-tracked seismic data, passive ants. The positions of the Top-Palaeozoicum, the Top-Gipsdalen and the Top-Basement surfaces are indicated.

3.1.2. Chaos – Ant-tracking workflow

To enhance discontinuities for fault and facture mapping, a high-pass filter (Figure 3.4C, Figure 3.4H) was applied to the seismic volumes in the first step (Figure 3.4B, Figure 3.4G). A filter makes discontinuities in the data more apparent (Figure 3.4B, Figure 3.4G). The filter applied to the study area of 3D seismic survey SG9810 removes frequencies below 40 Hz (Figure 3.4C) and the filter applied to the high resolution 3D seismic survey NH0372 removes frequencies below 70 Hz (Figure 3.4H). The testing showed that the final result of the 'Chaos – Ant-tracking workflow' is the best when the mentioned filters are applied.

To increase the continuity of the seismic reflections, the data were structure-smoothed (Figure 3.4D, Figure 3.4I) in the second step and parameters: Dip-guide and Enhance edge were selected. When the Dip-Guide is selected, smoothing is performed parallel to local structural orientation estimate. When the Enhance edge is selected, smoothing is performed by two half filters and only more chaotic signal is removed, what enhances edges in the seismic data (Schlumberger, 2009b). The size of the filter was kept default.

To detect discontinuities in the data, the chaos attribute cube (Figure 3.4E, Figure 3.4J, Figure 3.5A, Figure 3.5D) was applied in the third step. There are no additional parameters to choose regarding this attribute cube.

To extract faults and fractures from the data, the Ant-tracking attribute cube (Figure 3.5B, Figure 3.5E) was applied in the fourth step. The aim is to extract also minor faults and fractures, that is why the default parameters for the 'Aggressive ants' were chosen in this case. The Aggressive ants are able to find both major faults and subtle fractures, because their parameter-settings allow finding more connections in discontinuities in the data. To analyze the results correctly, it is desirable that faults and fractures in all directions and dips are found. However, testing showed that dips under 20° are allowing the ants to track artificial horizontal structures in the areas of less pronounced seismic signal between two strong reflections, parallel to these reflections. That is why the final Stereonet settings were adjusted to all azimuths: 0 - 360° but only dips: 20 – 90° in both 3D surveys.

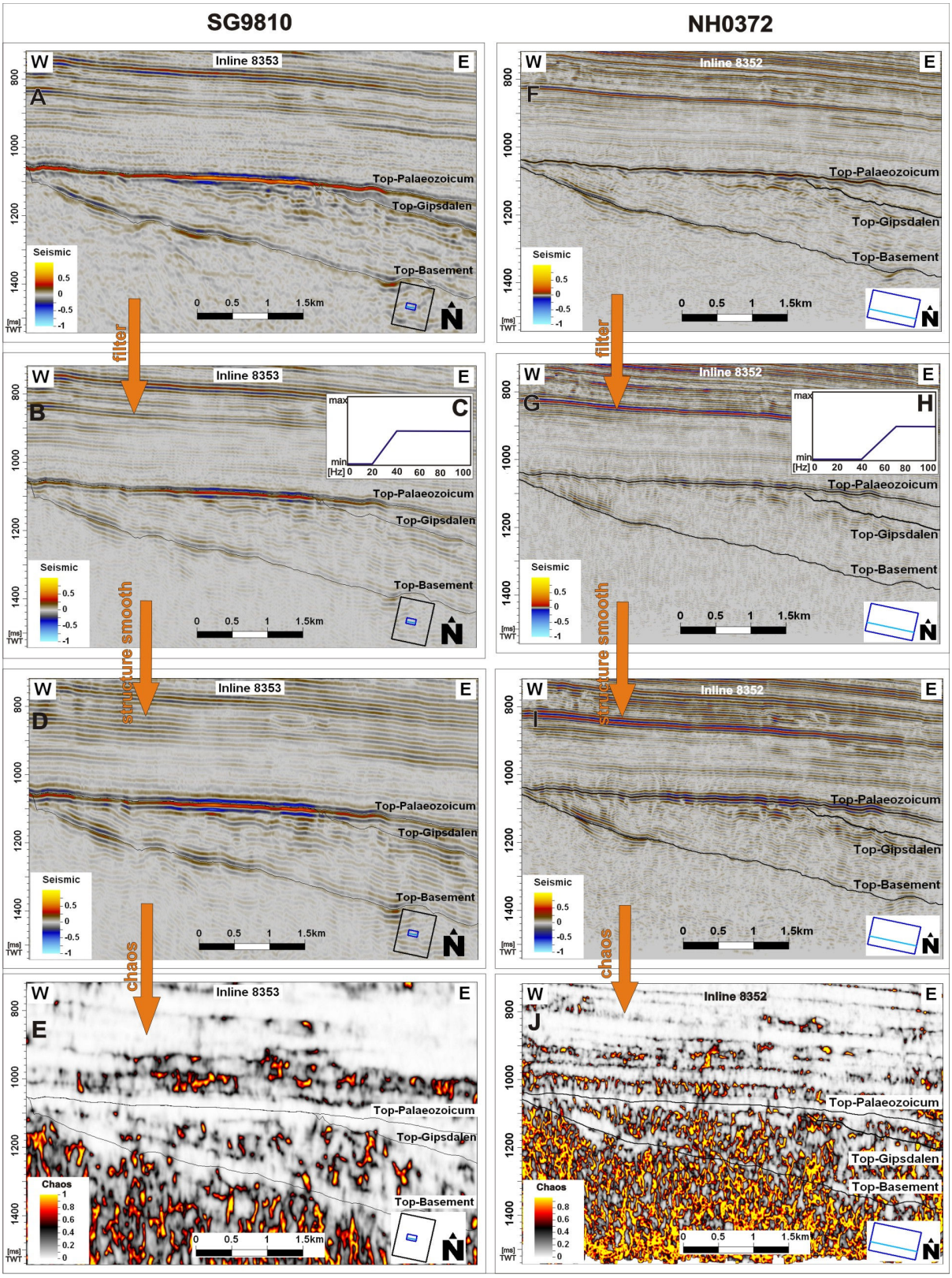

Figure 3.4 The first three steps of 'Chaos – Ant-tracking workflow' applied to the seismic inline 8353 of survey SG9810 (B, D, E) and to the seismic inline 8352 of high-resolution site survey NH0372 (G, H). (A, F) Original seismic data. (B, G) Filtered seismic data. (C, H) Used high-pass filter. (D, I) Structure smoothed seismic data. (E, J) Seismic data after application of the Chaos attribute cube. The positions of the Top-Palaeozoicum, the Top-Gipsdalen and the Top-Basement surfaces are indicated.

To achieve a good quality of 3D visualization, the ant-tracked volume was ant-tracked once more (Figure 3.5C, Figure 3.5F) in the last step of the workflow. It enhanced the amplitudes of the previous Ant-track result. The final result became clearer and the amplitudes stronger. In this case, it was desirable to enhance the result strongly, because the amplitudes after the first application of the Ant-tracking algorithm were low. Therefore the Ant-tracking attribute cube was applied again with exactly the same settings as in the previous step (‘Aggressive ants’).

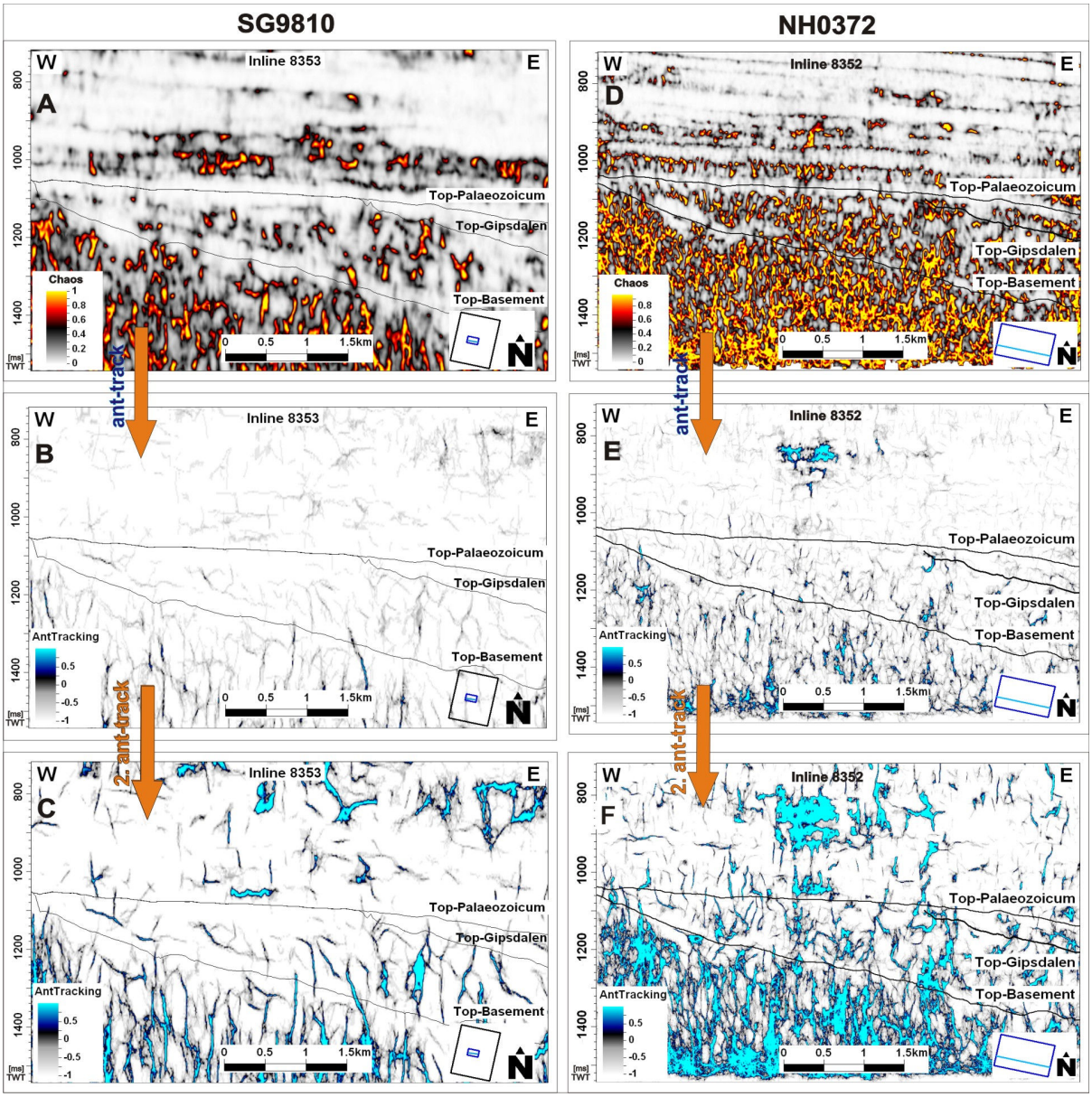

Figure 3.5 The last two steps of ‘Chaos – Ant-tracking workflow’ applied to the seismic inline 8353 of survey SG9810 (B, C) and to the seismic inline 8352 of high-resolution site survey NH0372 (E, F). (A, D) Seismic data after application of the Chaos attribute cube. (B, E) Ant-tracked seismic data, aggressive ants. (C, F) Second time ant-tracked seismic data, agressive ants. The positions of the Top-Palaeozoicum, the Top-Gipsdalen and the Top-Basement surfaces are indicated.

3.2. Final result of Ant-tracking – 3D visualization of faults and fractures connected to carbonate build-ups

The distribution of faults and fractures in carbonate build-ups of the Gipsdalen Group has been checked in the final Ant-tracking results from the two customized workflows, the 'Chaos – Ant-tracking workflow' (Figure 3.5C, Figure 3.5F) and the 'Variance – Ant-tracking workflow' (Figure 3.3C, Figure 3.3F). Each 5th inline of the result of Ant-tracking, in both seismic surveys (Figure 3.6A), was viewed. The purpose of this was to determine positions of faults and fractures in respect to positions of build-ups and connection between the two, as well as an answer to a question: 'Are all of the build-ups associated with a fault or fracture or not?' The answer is: Some of the identified faults or fractures are clearer and bigger than other, but all build-ups in the study area are associated with one or two faults or fractures. There were found no build-ups, which could be claimed to be clearly 'fault-less'. It is important to note that it is not possible to determine directly from the Ant-tracking results, whether the detected discontinuity is a fault or a fracture. A fracture is a general term for any break in a rock, due to mechanical failure by stress, whether or not it causes displacement. A fault is a fracture or a zone of fractures along which there has been a displacement (Bates and Jackson, 1980). It is not an objective of this thesis to differentiate between the two categories, only to detect the discontinuities which could be classified as faults or fractures. However, some interpretation is suggested. The discontinuities with lesser areal extent and often sub-vertical are interpreted as fractures. The larger discontinuities, often several hundred meters in extent, are interpreted as faults.

To determine whether the detected faults and fractures are real and not artefacts, the two Ant-tracking workflows, were applied to both data sets and their results were compared. Both workflows give similar results, revealing faults and fractures in carbonate build-ups of the Gipsdalen Group. In some cases the results are almost identical, in some cases different. The larger the fault or fracture is, the more similar results can be observed. Sometimes the fracture or fault is revealed only by one of the workflows. Then it depends on the interpreter to decide if the response is a real fracture or fault, or if it is an artefact. Mostly the two results are very similar and the difference is only in the size or slightly in the angle of the fracture or fault. In such

cases, the response can be easily considered real. To see the similarities and the differences in the two results, it is essential to do the comparison in three dimensions. Viewing the two results in two dimensions only in a seismic line does not show the full picture and leads to misinterpretation. What looks like a different response in one line, may transform into a continuous clearly visible fault or fracture on the next 10 lines. Cropping the cube in the area of interest as described in *2.4 Three dimensional visualization of the results of the Ant-tracking algorithm workflow* and comparing the results in three dimensions spares a lot of time and gives clear answers.

To illustrate the apparent relationship between the build-ups and faults, I have randomly chosen three build-ups (Area I, II, III) from the Top-Gipsdalen surface map of the study area of survey SG9810 (Figure 3.6A) and one build-up from the Top-Gipsdalen surface map of the high resolution site survey NH0372 (Figure 3.10). These build-ups and their associated faults are visualized, in three dimensions, in figures 3.7, 3.8, 3.9 and 3.11.

3.2.1. Study area of 3D seismic survey SG9810

For 3D visualization of faults in the study area of 3D seismic survey SG9810 was chosen the result of the 'Chaos-Ant-tracking workflow' applied to this survey.

A strong seismic reflector has been mapped in the study area of survey SG9810 (Figure 3.6). Eastern part of this reflector is the Top-Gipsdalen surface and the western part of the reflector reveals a fraction of the Top-Basement surface (Figure 3.6A). The Top-Gipsdalen surface consists of two parts. The eastern, dipping, part (Figure 3.6) represents the boundary between the Gipsdalen Group and the overlaying Bjarmeland Group. It is characterized by an irregular topography, caused by numerous polygonal network build-ups and associated enclosed lagoons. The western, up-dip part is characterized by a smoother topography, where the successive reflectors of the Gipsdalen Group are truncated in the area between the Top-Gipsdalen and the Base-Gipsdalen truncation lines (Figure 3.6A). Further up-dip, to the west, is the visible part of the Top-Basement surface (Figure 3.6A). It is also a truncated surface and represents the boundary between the Caledonian

metamorphic rocks of basement and the overlaying Triassic Snadd Formation. The truncated area of the seismic reflector represents a major unconformity caused by uplift and erosion, including extensive karstification of carbonates of the Gipsdalen Group, during late Sakmarian-Artinskian time (Figure 1.3) (Worsley, 2008).

On the eastern dipping ramp are recognized two areas containing build-ups: the 'Area of larger build-ups' – NE of the study area, and the 'Area of smaller build-ups' – SE of the study area (Figure 3.6A). These two are divided by a SW-NE major fault (Figure 3.6A). The fault is dividing the ramp into two ramp segments. The ramp segment in the 'Area of smaller build-ups' has steeper dip what means that the "Area of larger build-ups" subsided less rapidly.

The three randomly chosen build-ups (I, II, III in Figure 3.6A) are visualized in three dimensions (Figure 3.7A, Figure 3.8A, Figure 3.9A). The seismic lines (Figure 3.7A, Figure 3.8A, Figure 3.9A) create a three dimensional 'slide show', gradually slicing the same fault/faults showed from one angle. Positions of the seismic lines are indicated on the Top-Gipsdalen surface (Figure 3.7B, Figure 3.8B, Figure 3.9B). The seismic line number 1 is always the furthermost from the observer and the following is nearer and nearer. A bigger part of the fault/faults disappears behind each coming line.

There are two faults associated with the build-up in area I (Figure 3.7). Both of these faults are situated on the slope of the build-up, on both sides of the build-up ridge, where the steep dip of the build-up's side partly flattens into a gentle dip. With the build-up in area II is associated one fault (Figure 3.8). The fault is situated very near to the top of the build-up ridge. Its position slightly differs from inline to inline. On the inline 6771 (Figure 3.8A-5), in the deeper part of the build-up, we can see that the fault separates into two. There are again two faults associated with the build-up in area III (Figure 3.9). Same as in area I, the faults are situated on the slope of the build-up, on both sides of the build-up ridge, where the steep dip of the build-up's side partly flattens into a gentle dip. Crosslines 6493, 6473 and 6453 (Figure 3.9A-1, 2, 3) are displaying the southern fault (Figure 3.9B), while crosslines 6433 and 6413 (Figure 3.9A-4, 5) are displaying the northern fault (Figure 3.9B). The crossline 6453 (Figure 3.9A-3) is showed from two different angles.

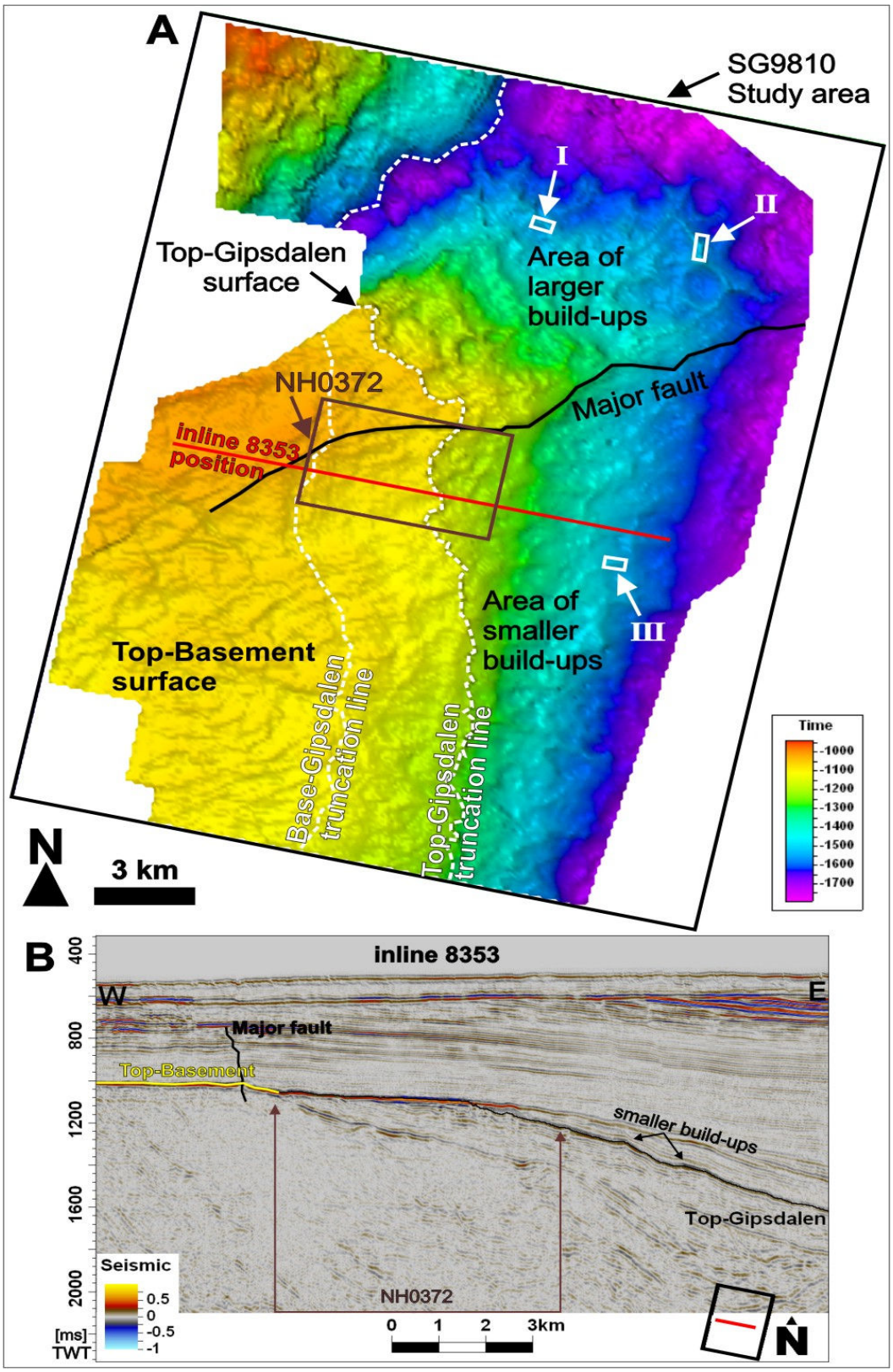

Figure 3.6 (A) Study area of 3D seismic survey SG9810 - the Top-Gipsdalen and the Top-Basement TWT map. Positions of the high resolution 3D site survey NH0372, 'Area of larger build-ups' and 'Area of smaller build-ups', 3 locations containing build-ups (I, II, III), major fault, the Top-Gipsdalen and the Base-Gipsdalen truncation lines, and the seismic inline (showed in B) are indicated. (B) Seismic inline 8353 through the area, showing the Top-Gipsdalen and Top-basement surfaces. The major fault, the two of the smaller build-ups and the position of high resolution 3D seismic survey NH0372 are indicated.

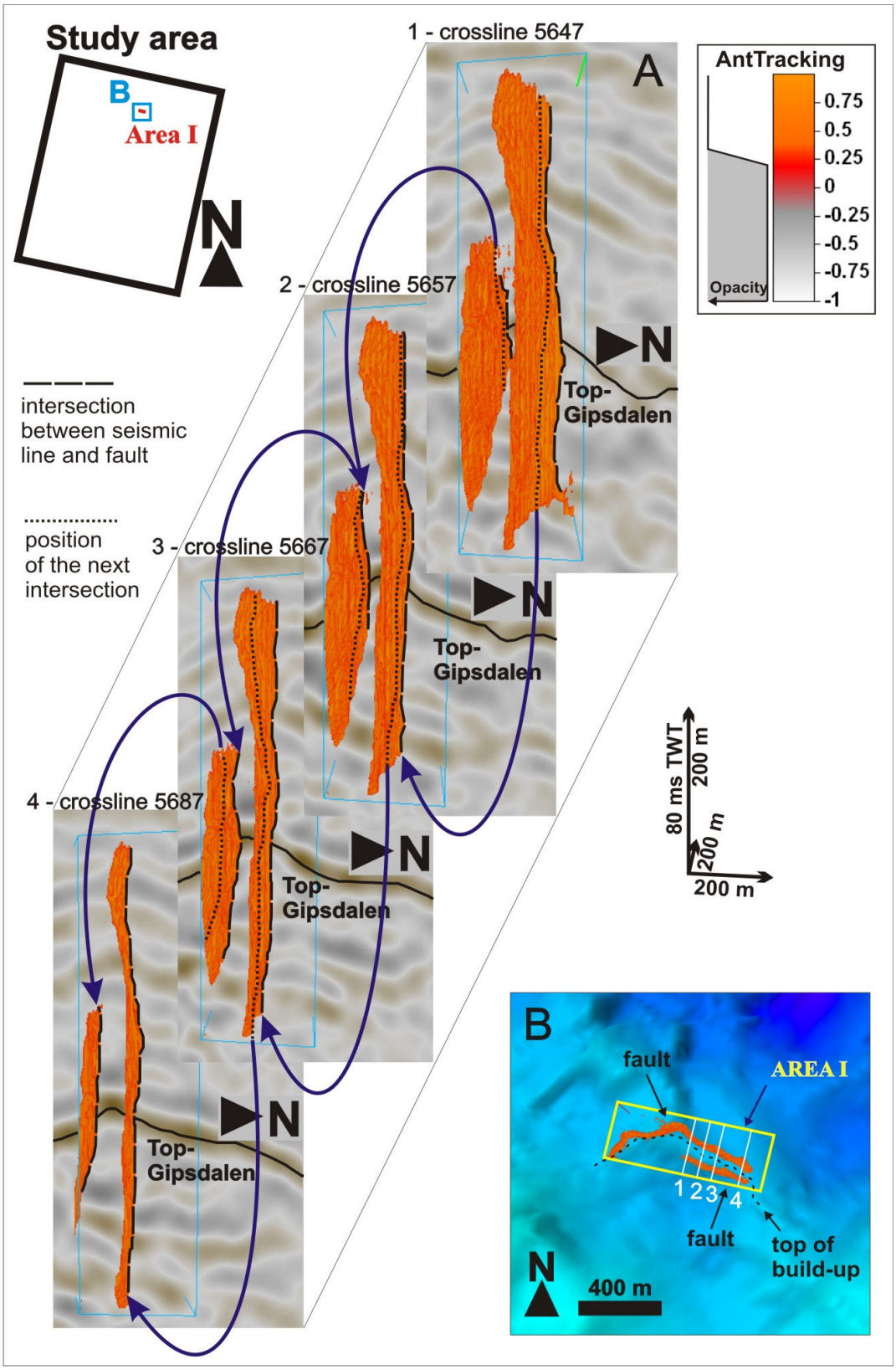

Figure 3.7 (A) Three dimensional visualization of area I, showing a build-up forming a relief on the Top-Gipsdalen surface (black line) and connected faults (orange) on four crosslines. Positions of the Top-Gipsdalen surface, intersections between the seismic line and the fault and the positions of the following intersections are indicated on seismic lines. (B) Location of area I on the Top-Gipsdalen surface time structure map. Positions of faults on sides of the build-up are illustrated in orange. Positions of seismic crosslines (1, 2, 3, 4), visualized in A, are indicated by white lines. The top of the build-up ridge is indicated by black dashed line.

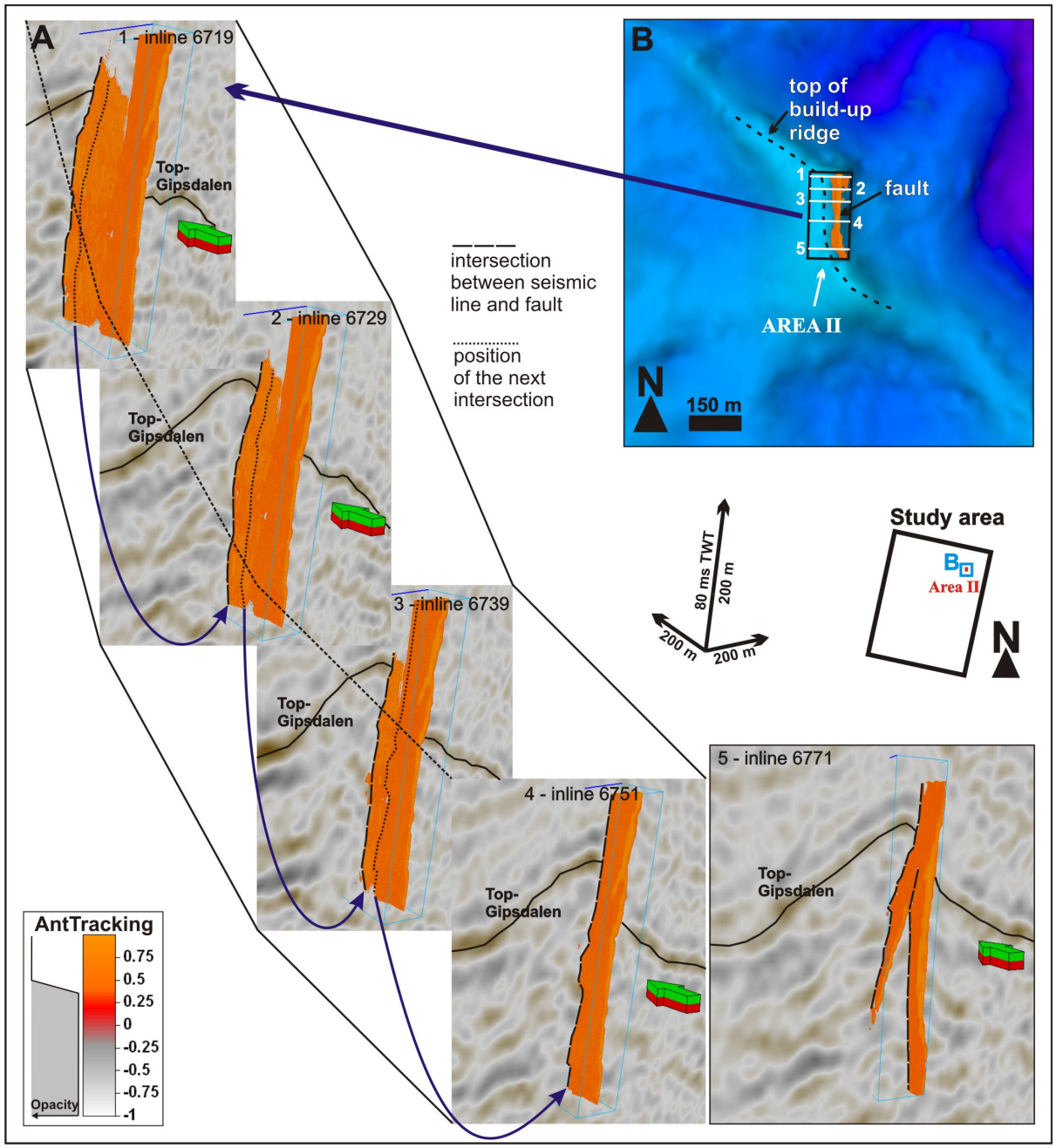

Figure 3.8 (A) Three dimensional visualization of area II, showing a build-up forming a relief on the Top-Gipsdalen surface (black line) and a connected fault (orange) on five inlines. Positions of the Top-Gipsdalen surface, intersections between the seismic line and the fault and the positions of the following intersections are indicated on seismic lines. (B) Location of area II on the Top-Gipsdalen surface time structure map. A position of fault on side of the build-up is illustrated in orange. Positions of seismic inlines (1, 2, 3, 4, 5), visualized in A, are indicated by white lines. The top of the build-up ridge is indicated by black dashed line.

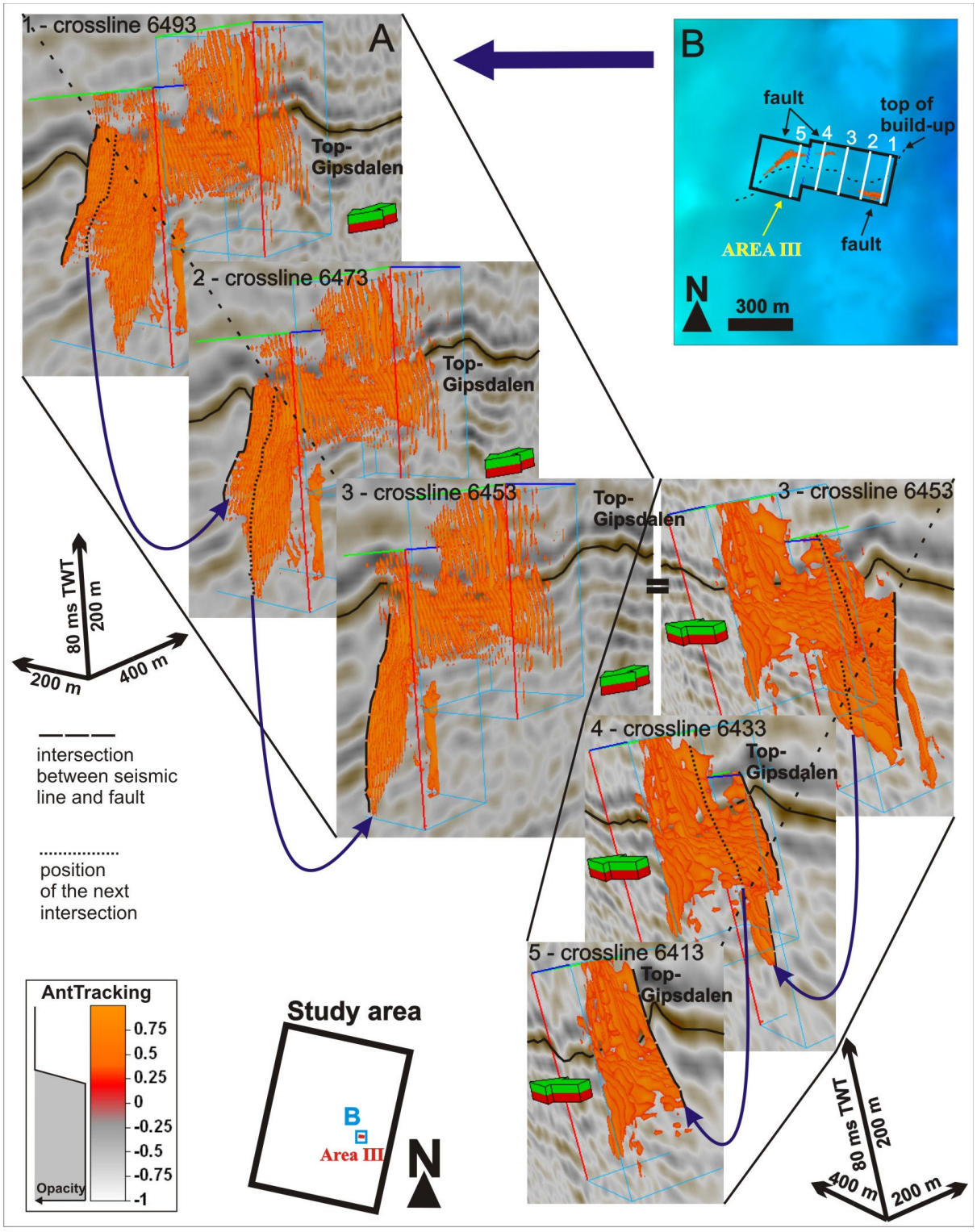

Figure 3.9 (A) Three dimensional visualization of area III, showing a build-up forming a relief on the Top-Gipsdalen surface (black line) and connected faults (orange) on five crosslines. Positions of the Top-Gipsdalen surface, intersections between the seismic line and the fault and the positions of the following intersections are indicated on seismic lines. (B) Location of area III on the Top-Gipsdalen surface time structure map. Positions of faults on sides of the build-up are illustrated in orange. Positions of seismic crosslines (1, 2, 3, 4, 5), visualized in A, are indicated by white lines. The top of the build-up ridge is indicated by black dashed line.

3.2.2. High resolution 3D seismic survey NH0372

The high resolution 3D seismic survey NH0372 has less areal extent (Figure 3.6A) and therefore does not contain as many carbonate build-ups as the study area of 3D seismic survey SG9810. The Top-Gipsdalen surface of the high resolution 3D seismic survey NH0372 can be divided into two areas with different topography (Figure 3.10A). On the western part is the Upper-Palaeozoic unconformity, a result of an uplift of the Loppa High above the sea-surface during the late Palaeozoic. This area does not have build-up topography. On the eastern part is a dipping ramp, where several build-up ridges and one enclosed lagoon (Figure 3.10A) can be recognized. The build-ups in the high resolution 3D seismic survey NH0372 are not as pronounced as the build-ups in the study area of 3D seismic survey SG9810, because they are on the upper part of the ramp and also in the 'Area of smaller build-ups' (Figure 3.6A). However, many discontinuities can be recognised in the result of the Ant-tracking workflow (Figure 3.10B, C) thanks to high resolution of the survey. For 3D visualization of faults and fractures in this case, the result of the 'Variance-Ant-tracking workflow' applied to this survey was chosen (Figure 3.10B, C). The recognised discontinuities have small areal extent and are mostly sub-vertical with angles around 80° to 90°. Therefore these are mostly interpreted as fractures associated with build-ups.

The connection between the position of fractures and the change of the dip in topography is clearly visible in this high resolution site survey. Ant-tracking revealed not only fractures apparently associated with the build-up's location, such as fractures 1, 2, 12, (Figure 3.10B) or 10, 11 (Figure 3.10C), but also fractures in areas of subtle change in the dip of topography such as 8, 9 (Figure 3.10B, C). The fractures 5 and 6 (Figure 3.10C) are clearly visible on the slopes of very tiny build-ups with small relief. Ant-tracking revealed fractures, on the slopes of build-ups, precisely surrounding the enclosed lagoon (Figure 3.10B-3, 6, 7, 10, 12). On the seismic crossline (Figure 3.10D), we can see some of the fractures (4, 10 and 11), detected by the Ant-tracking workflow, directly visible in the seismic data. The ant-tracking workflow obviously detects more than is directly visible in a seismic line. Majority of detected fractures can be considered real with high confidence, because

of their precise position around the lagoon (Figure 3.10B-3, 6, 7, 10, 12) and on the sides of a build-up (Figure 3.10B-1, 2, 12).

One, randomly chosen build-up (area IV in Figure 3.11B) is visualized in three dimensions (Figure 3.11A). The seismic in-lines in the figure create a three dimensional 'slide show', as explained in *3.2.1 Study area of 3D seismic survey SG9810.* Positions of the seismic in-lines are indicated on the Top-Gipsdalen surface (Figure 3.11B). The fracture is situated very near to the top of the build-up ridge. Its position moves a bit downhill on the inline 8272 (Figure 3.11A-4).

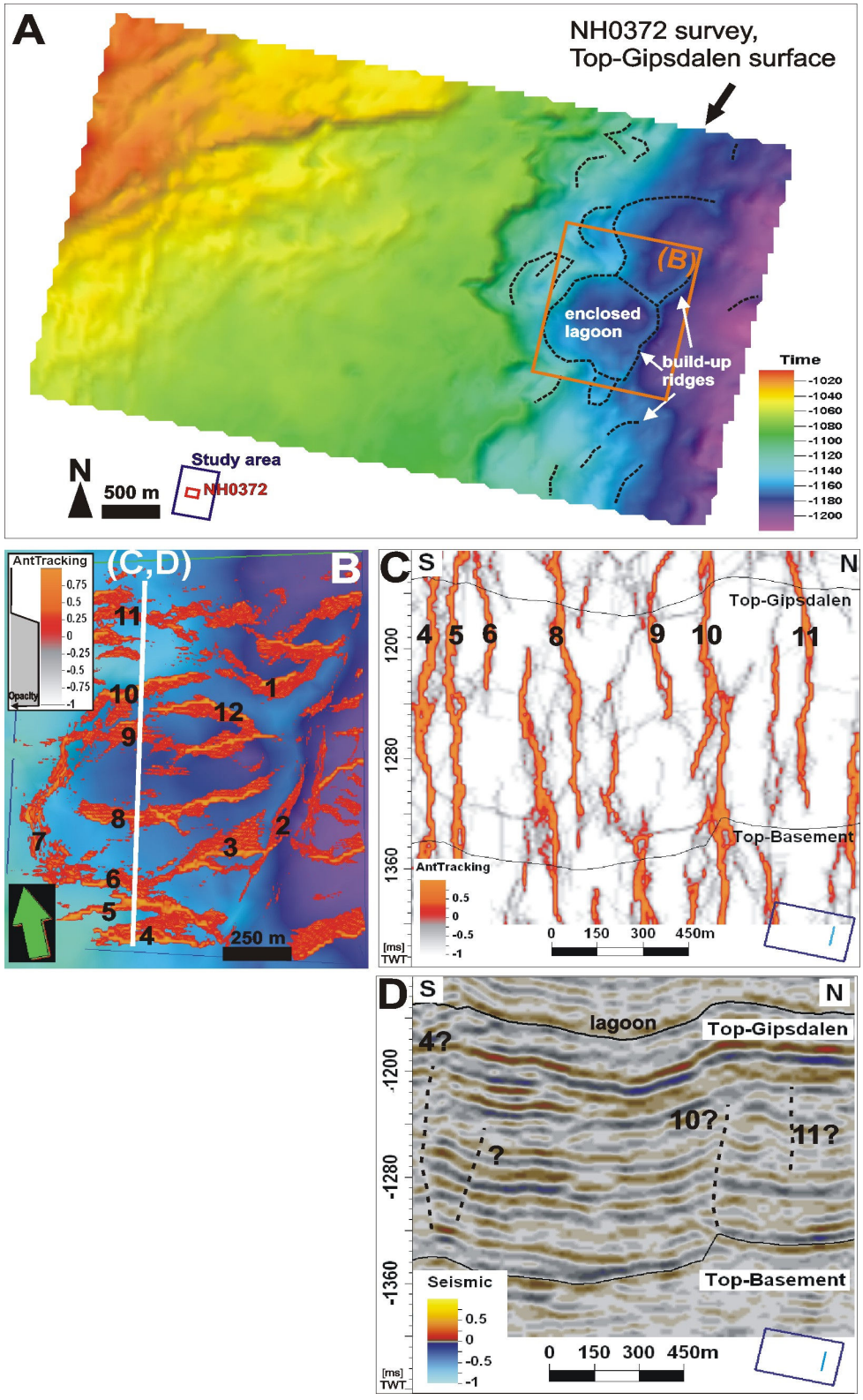

Figure 3.10 (A) Top-Gipsdalen surface of high resolution site survey NH0372. Positions of build-up ridges, enclosed lagoon and zoomed area from B are indicated. (B) Faults and fractures (orange) associated with build-ups from the result of the 'Variance – Ant-tracking workflow' are visualized on the Top-Gipsdalen surface time structure map. Faults and fractures 3, 6, 7, 10 and 12 are enclosing the lagoon. Position of the crossline from C and D is indicated by a white line. (C) Crossline 5564 showing faults and fractures (orange) associated with build-ups. (D) Seismic crossline 5564. Some of the detected faults and fractures are visible directly in seismic data. The lagoon is indicated. Positions of the Top-Gipsdalen and the Top-Basement surfaces are indicated in C and D.

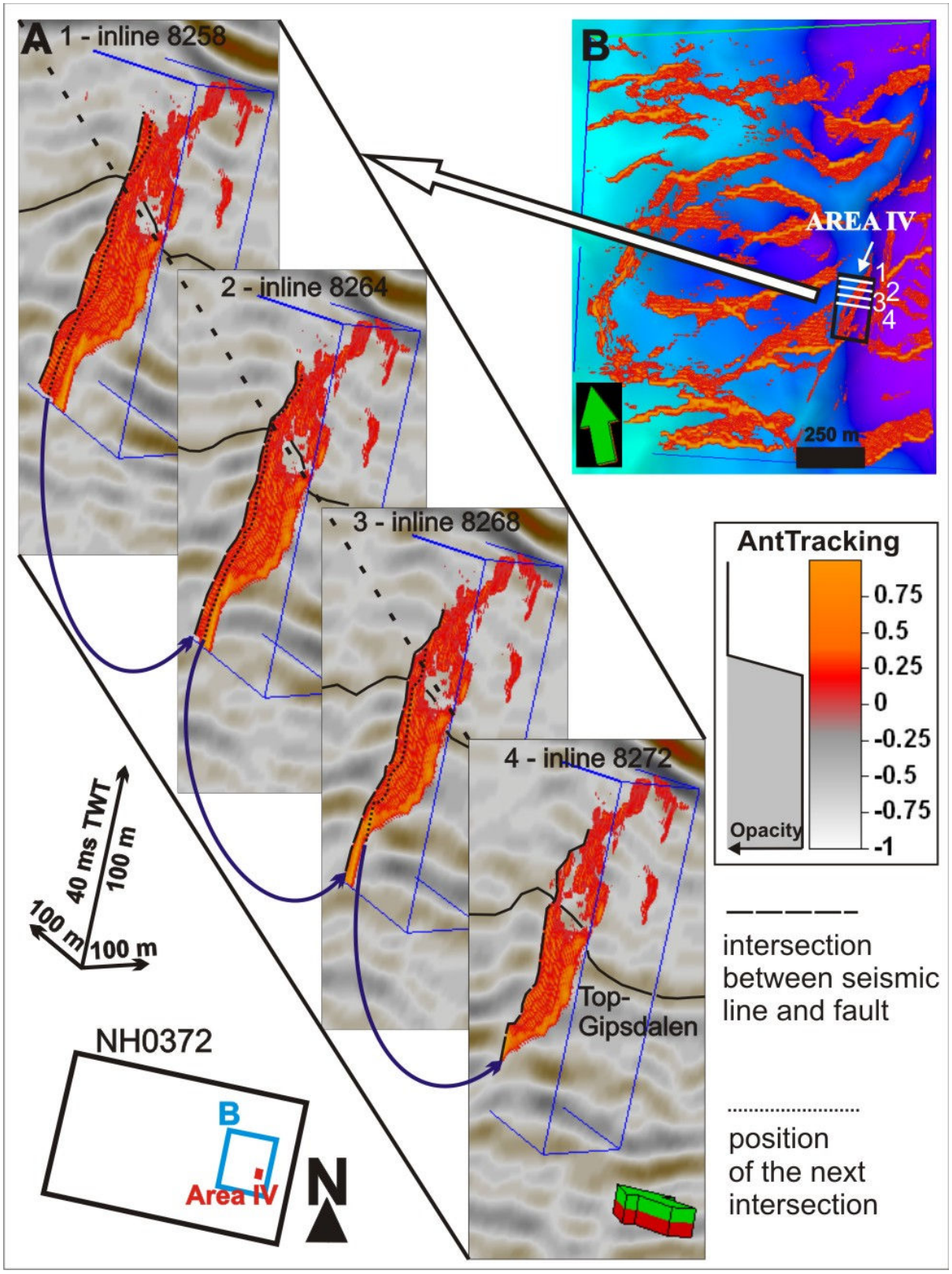

Figure 3.11 (A) Three dimensional visualization of area IV (from high resolution 3D seismic survey NH0372), showing a build-up forming a relief on the Top-Gipsdalen surface (black line) and connected fracture (orange) on four inlines. Positions of the Top-Gipsdalen surface, intersections between the seismic line and the fracture and the positions of the following intersections are indicated on seismic lines. (B) Location of area IV on the Top-Gipsdalen surface time structure map of high resolution 3D seismic survey NH0372. Positions fractures are illustrated in orange. Positions of seismic inlines (1, 2, 3, 4), visualized in A, are indicated by white lines.

3.3. Final result of Ant-tracking – 3D visualization of karst in sinkholes

The Ant-tracking method was developed for Petrel^{TM} software to detect faults, but as mentioned before, it also detects other discontinuities. Collapsed karst creates sinkholes and has a different composition than the surrounding bedrock. The sinkholes are typically filled by more or less massive breccia bodies. The boundary between karst and the surrounding bedrock is typically sharp and the seismic response is an abrupt transition from well-organized subparallel/parallel reflection patterns to systematic down-bending, mixed with chaotic, reflection patterns (Figure 3.12C). The top surface of sinkholes typically forms a more or less circular depression on a horizon subjected to karst deformation (Figure 3.12B), as a result of cavern roof collaps. Sinkholes are normally very well visible on the time maps (Figure 3.12B, Figure 3.13, Figure 3.14B) and directly in seismic lines (Figure 3.12C). Therefore the results of the Ant-tracking workflow were also checked for sinkhole response.

3.3.1. Study area of 3D seismic survey SG9810

Several smaller or bigger sinkholes are visible on the Gipsdalen surface of the study area of 3D seismic survey SG9810 (Figure 3.13B, C and D). The most pronounced detected sinkhole, of diameter 250 m, is clearly visible on the seismic line due to systematic down-bending, mixed with chaotic, reflection pattern (Figure 3.12C) and on the Top-Gipsdalen surface, creating a circular depression (Figure 3.12B, Figure 3.13). However, there is no clear response in the Ant-tracking results, in neither the 'Chaos – Ant-tracking workflow' nor the 'Variance – Ant-tracking workflow' that could be connected to the position of the sinkhole.

The Ant-tracking workflow is in general not designed for the detection of sinkholes but for detection of faults. Compared to sinkholes, faults are planar structures with large lateral extent. However, sinkholes can be very well detected by the Variance attribute cube (Figure 3.15C, D, E, F), if its parameters are customised for this objective, but that was not this case. If the response of the sinkhole is very strong and clear in the Variance attribute cube, then also the Ant-tracking workflow may

show slight response of the sinkhole in its result. But there are more suitable methods, which exist for sinkhole detection, such as 3D multi-attribute mapping of seismic facies (for example Carrillat *et al.*, 2005).

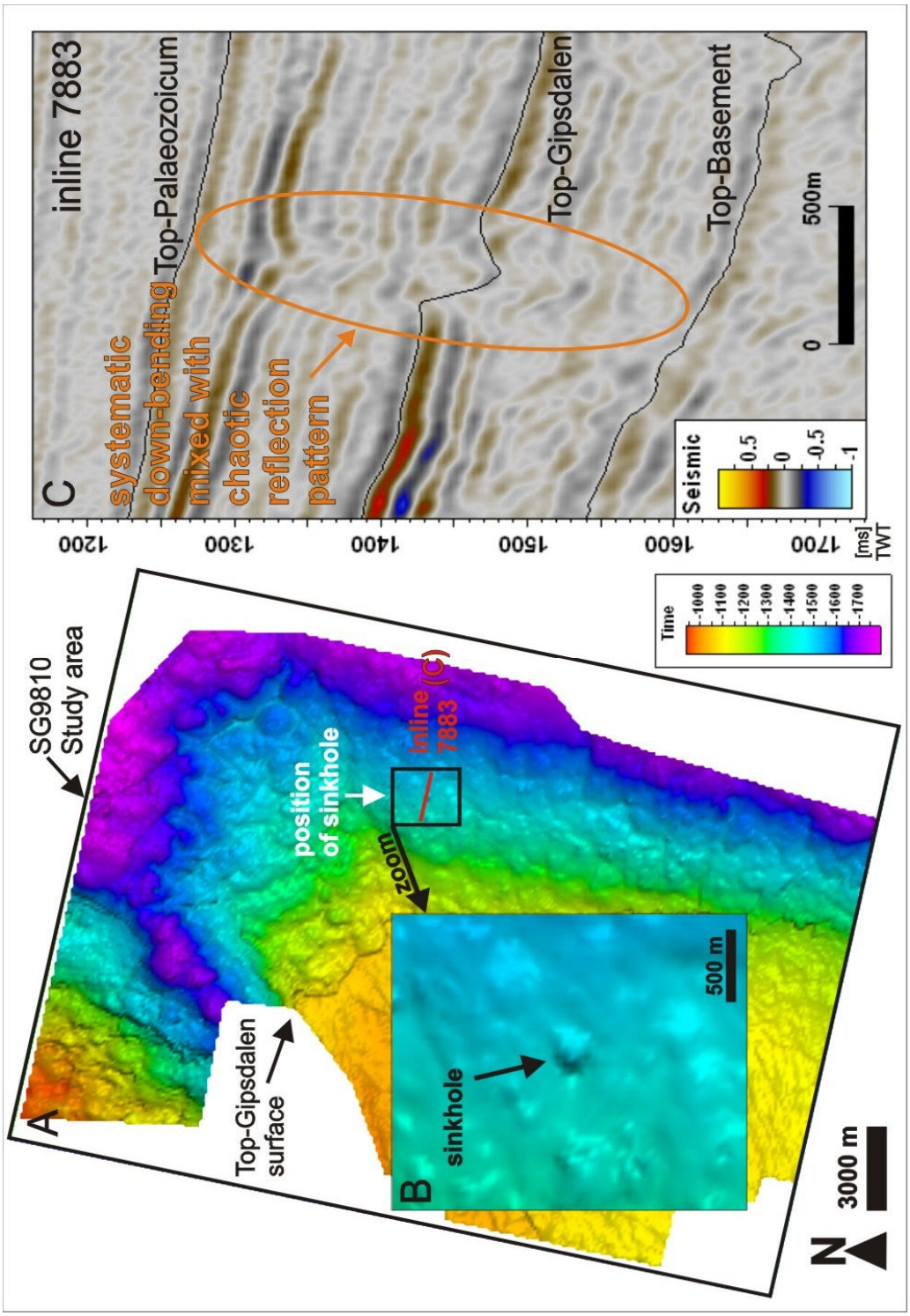

Figure 3.12 (A) Top-Gipsdalen surface of the study area of 3D seismic survey SG9810. Positions of sinkhole and inline 7883 are indicated. (B) Zoomed crop of the Top-Gipsdalen surface revealing the sinkhole in detail. (C) Seismic inline 7883 displaying systematic down-bending, mixed with chaotic, reflection pattern in the vicinity of the sinkhole. The Top-Palaeozoic, the Top-Gipsdalen and the Top-Basement surfaces are indicated by black lines.

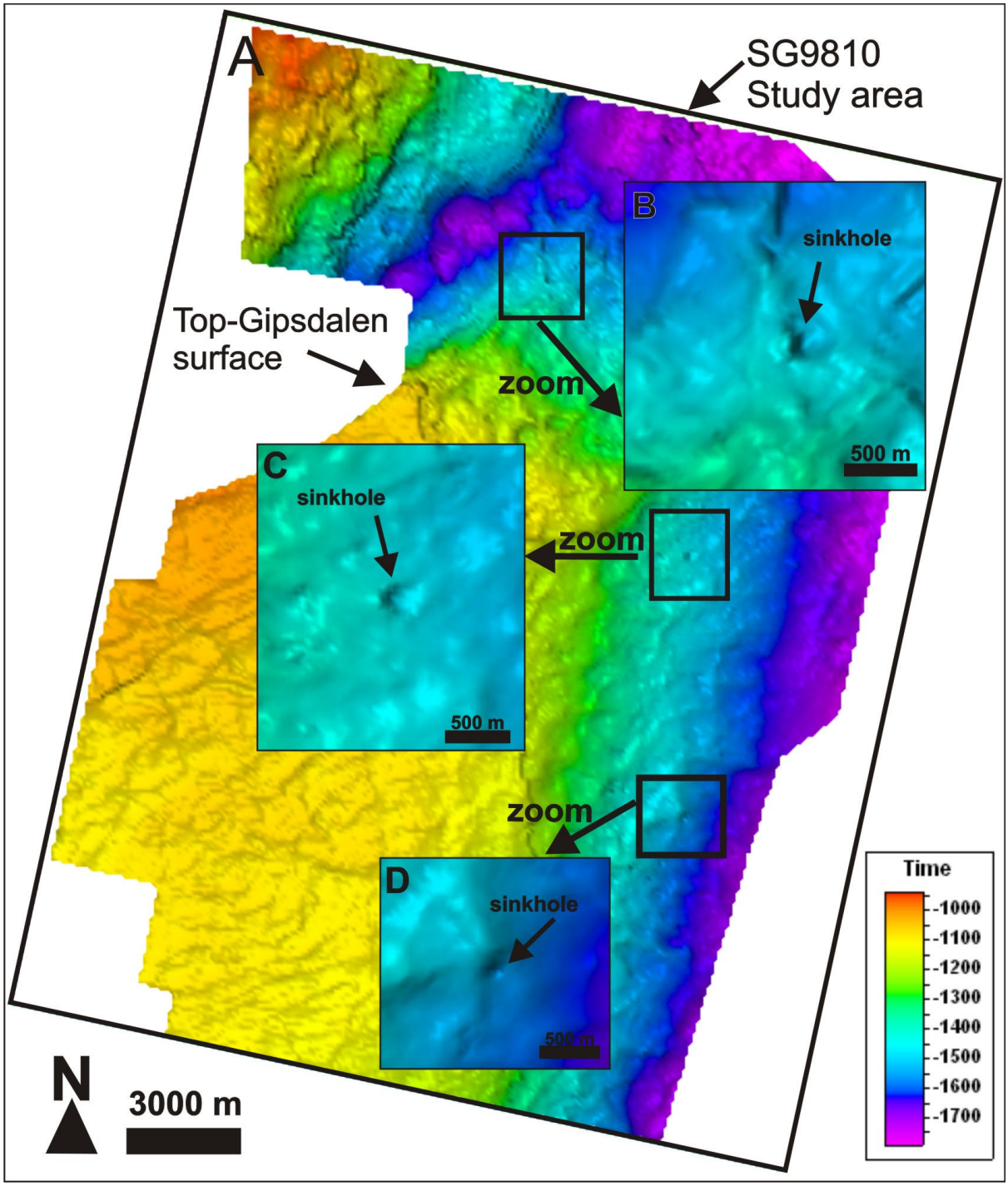

Figure 3.13 (A) Top-Gipsdalen surface of the study area of survey SG9810. Positions of three chosen sinkholes are indicated by black rectangles. (B, C, D) Zoomed crops of the Top-Gipsdalen surface revealing the sinkholes in detail.

3.3.2. High resolution 3D seismic survey NH0372

As mentioned in the previous chapter, the Ant-tracking workflow was not designed for the detection of sinkholes but for detection of faults. However the Variance attribute cube is very well suitable for sinkhole detection (Figure 3.15C, D, E, F) and thanks to high resolution of the site survey NH0372, and a strong response of a sinkhole in the Variance cube result (Figure 3.15C, D, E, F), a slight response of a sinkhole from the Top-Gipsdalen surface (Figure 3.15A, B, Figure 3.14A, B) was detected in the 'Variance - Ant-tracking workflow' (Figure 3.14C, D), even if its parameters were customised for detection of faults. The response of the sinkhole is very strong and clear, visible on a 1077 ms timeslice– in the plane of the Top-Gipsdalen surface (Figure 3.15C, D) and on a 1057 ms timeslice – 20 ms above the Top-Gipsdalen surface (Figure 3.15 E, F).

This sinkhole is visible on the time map of the Top-Gipsdalen surface in both the study area of survey SG9810 and in the site survey NH0372. However, there is no response of the mentioned sinkhole in the result of the Ant-tracking workflow applied to the study area of survey SG9810. This was expected, because this sinkhole is much smaller than the sinkhole detected on the inline 7883 (Figure 3.12C) and it would be surprising if a minor sinkhole has a response in the Ant-tracking result, while the major sinkhole does not. By application of the same technique as used for visualization of faults, the sinkhole response was visualized in three dimensions (Figure 3.14C, D) in the result of the 'Variance – Ant-tracking workflow'.

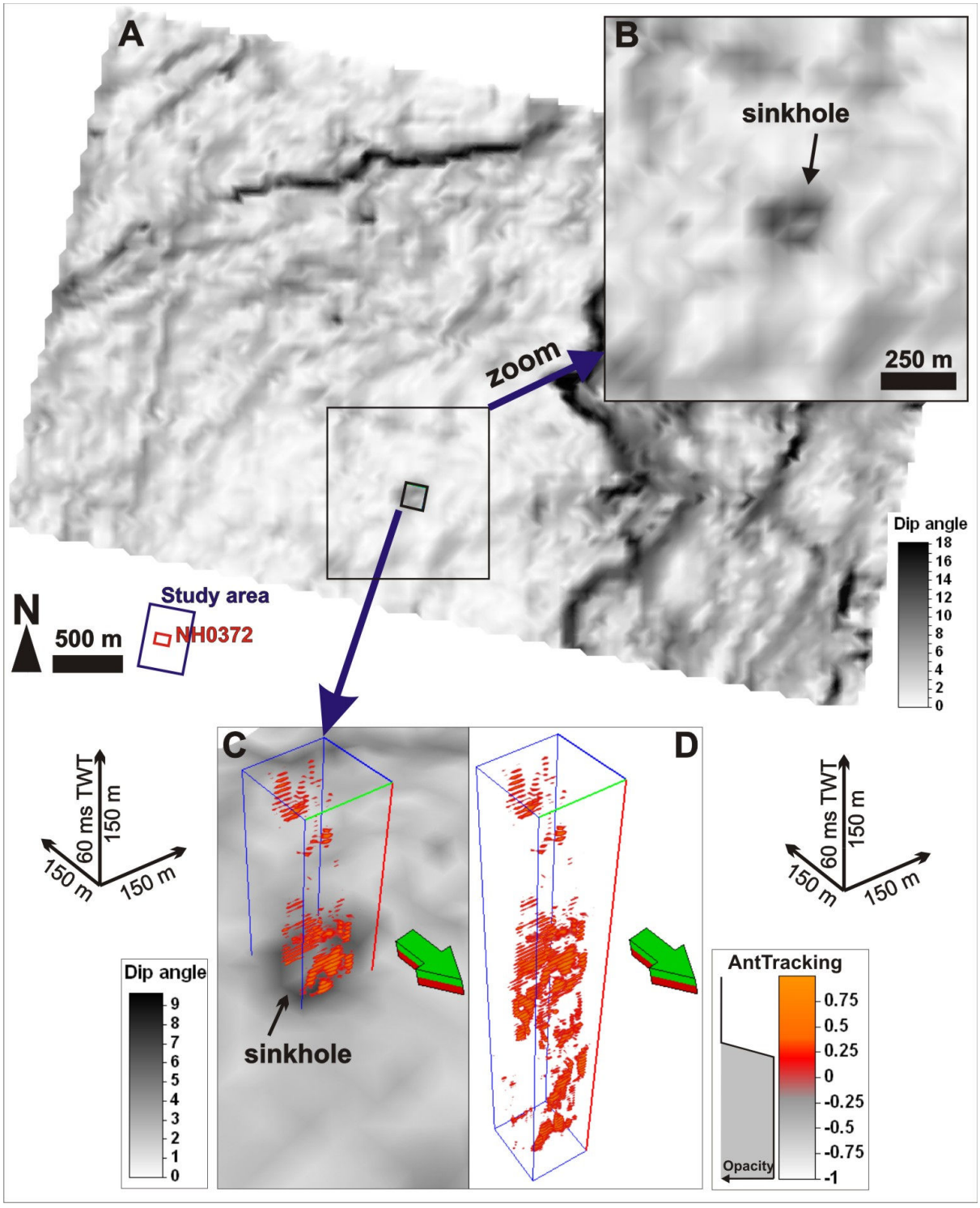

Figure 3.14 (A) Dip map of the Top-Gipsdalen surface of high resolution 3D seismic survey NH0372. Position of sinkhole is indicated by a black rectangle. (B) Zoomed crop of the Top-Gipsdalen surface revealing the sinkhole in detail. (C) 3D visualization of the sinkhole response in the Ant-tracking workflow result, plotted on the dip map of the Top-Gipsdalen surface. (C) Visualization of the whole sinkhole response in the Ant-tracking workflow result, in three dimensions.

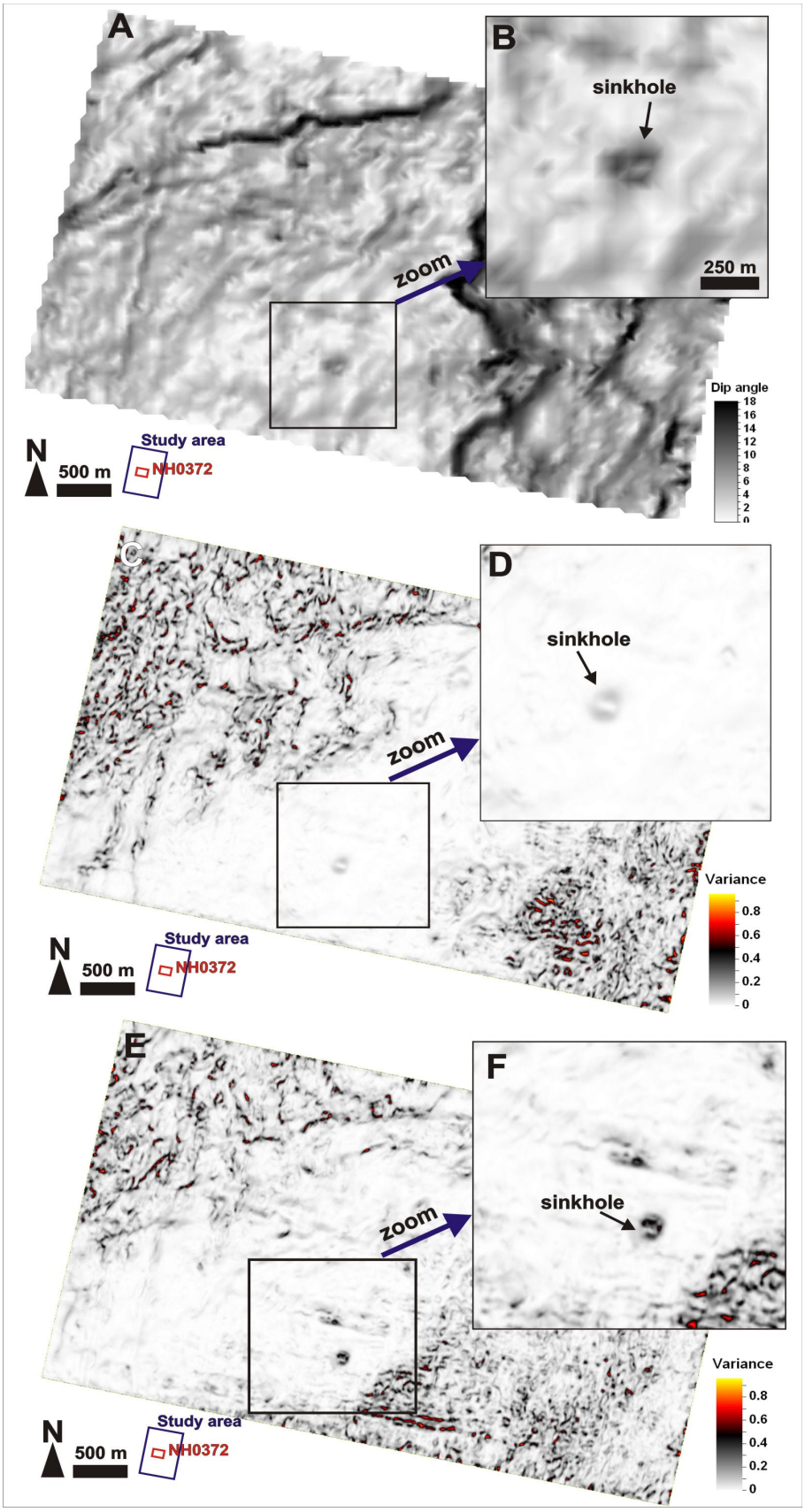

Figure 3.15 High resolution seismic site survey NH0372. (A) Dip map of the Top-Gipsdalen surface. (B) Zoomed crop of the Top-Gipsdalen surface revealing the sinkhole in detail. (C) Variance time slice map at 1077 ms. (E) Variance time slice map at 1057 ms. (D, F) Zoomed crop of the Variance time slice, revealing the sinkhole in detail. Position of sinkhole is indicated by black rectangles.

3.4. Different structures visible in the final result of the Ant-tracking workflow

The quality of the data affects the interpretation results. The reason for creating two different Ant-tracking workflows was to have a reference for comparing the results. In both the high resolution site survey NH0372 and the study area of survey SG9810, there are also many areas with high ant-tracking amplitude response, which are not representing faults or fractures connected to positions of build-ups (Figure 3.16B, Figure 3.17B, Figure 3.18A).

Three typical responses, found repeatedly in the results of the Ant-tracking workflow, are visualized here (Figure 3.16B, Figure 3.17B, Figure 3.18A). The results of the 'Chaos – Ant-tracking workflow' applied to the SG9810 survey were used to create the figures with examples, but the responses are typical regardless the workflow or the survey.

The mixture of coherence and chaotic signal (Figure 3.16A), seen in seismic lines, gives strong response in the Ant-tracking result (Figure 3.16B). This response looks partly as composed of many close fractures but is difficult to interpret clearly. Another type of chaotic response (Figure 3.17A) is caused by a single fault or fracture in the plane of the observed seismic line (Figure 3.17B). What may appear to be chaotic signal in direction of inline (Figure 3.17A), emerges as a clear fracture in the perpendicular plane – direction of crossline (Figure 3.17C-F). This confirms that the Ant-tracking workflow reveals also faults and fractures which would stay invisible for the interpreter. This is a clear example of a great advantage of a semi-automatic method, when detecting faults and fractures. The last example is a response from low amplitude signal between two seismic reflections (Figure 3.18). The directions ants are allowed to look for faults and fractures was set to 20°- 80° or 20°-90°. The aim of the Ant-tracking workflow was to detect faults and fractures, not response from low amplitude signal between two sub-horizontal reflections. The angle of 20° was chosen so, that the most of the response from the low amplitude signal between two sub-horizontal reflections is removed, but the response from faults and fractures stays in the final result. But if there is low amplitude signal

between two reflections, which are dipping in an angle over 20°, this response is detected (Figure 3.18A).

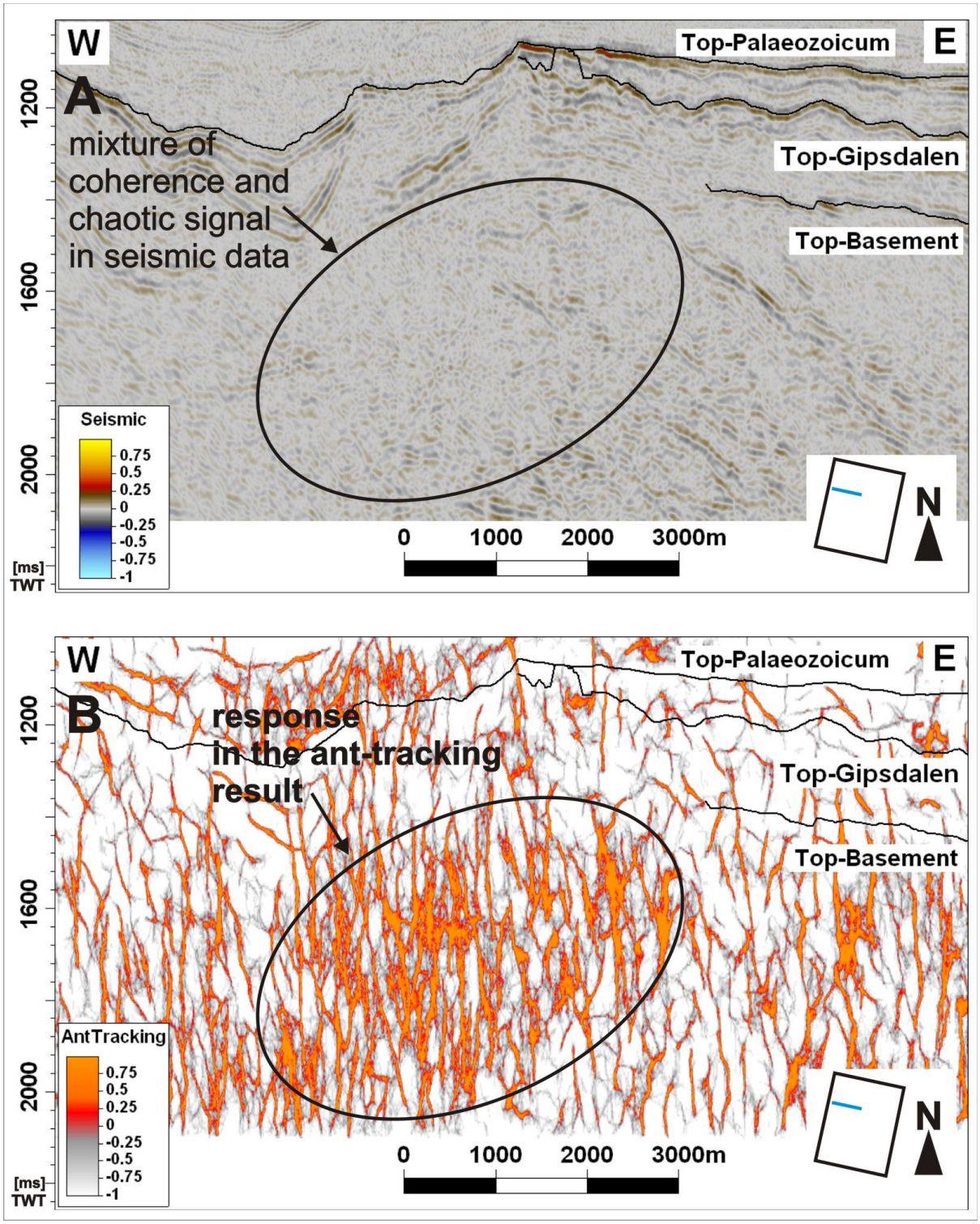

Figure 3.16 (A) Seismic inline of the study area of survey SG9810. Mixture of coherence and chaotic signal in the data is indicated. (B) The same seismic inline, displaying the result of the Ant-tracking workflow. The typical response of the mixture of coherence and chaotic signal in the data is indicated by the ellipse. The Top-Palaeozoic, the Top-Gipsdalen and the Top-Basement surfaces are indicated by black lines in both A and B.

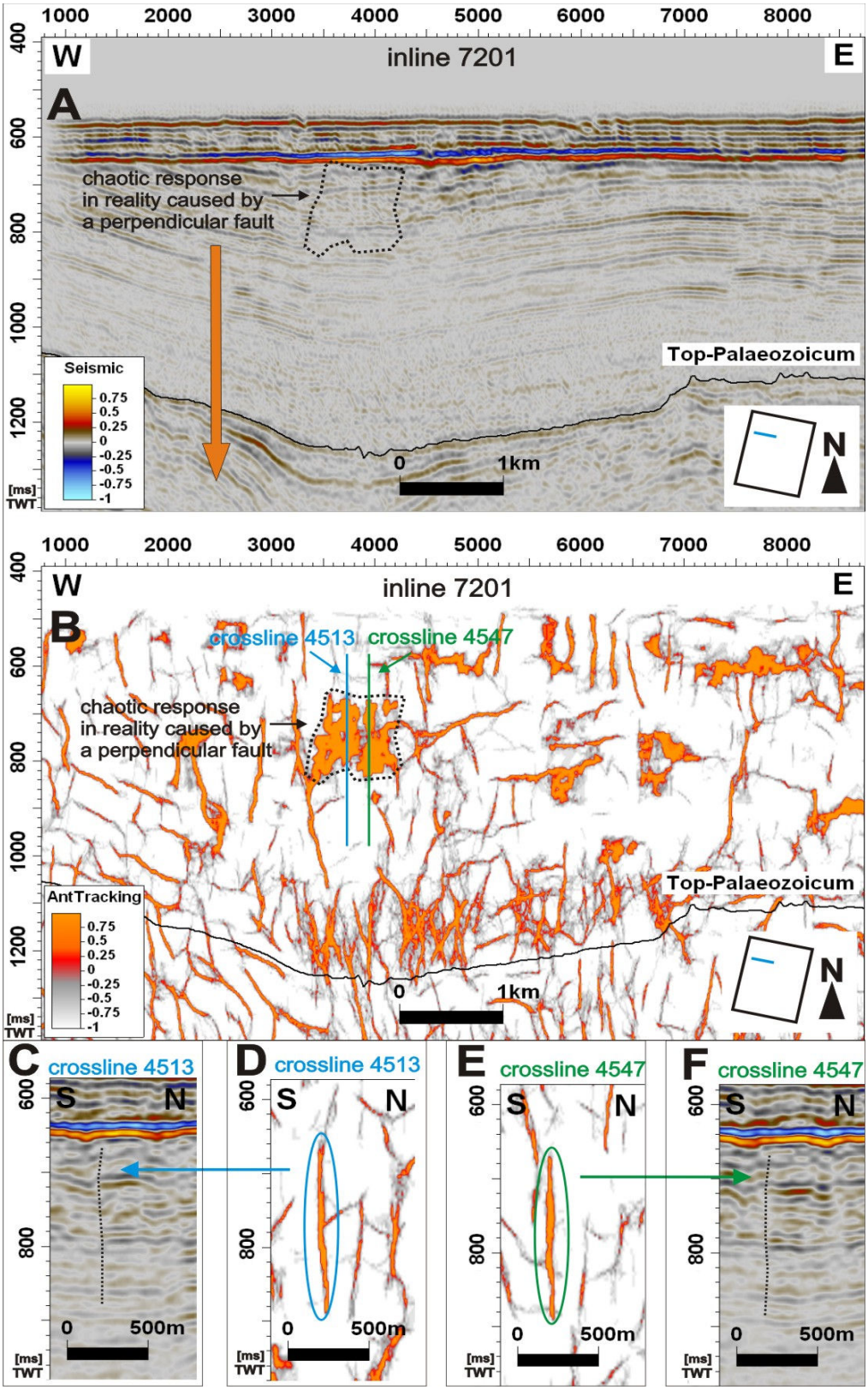

Figure 3.17 (A) Seismic inline 7201 of the study area of survey SG9810. Chaotic response in the data is indicated. (B) Seismic inline 7201, displaying the result of the Ant-tracking workflow. Chaotic response, caused by a perpendicular fracture is indicated. The positions of crosslines 4513 and 4547 are indicated in blue and green respectively. Position of the Top-Palaeozoic surface is indicated by black lines in both A and B. Position of the fracture, seen in a plane view in B, is indicated in the result of the Ant-tracking workflow on crossline 4513 (D) and crossline 4547 (E). Position of the fracture is indicated also in seismic data in crossline 4513 (C) and crossline 4547 (F).

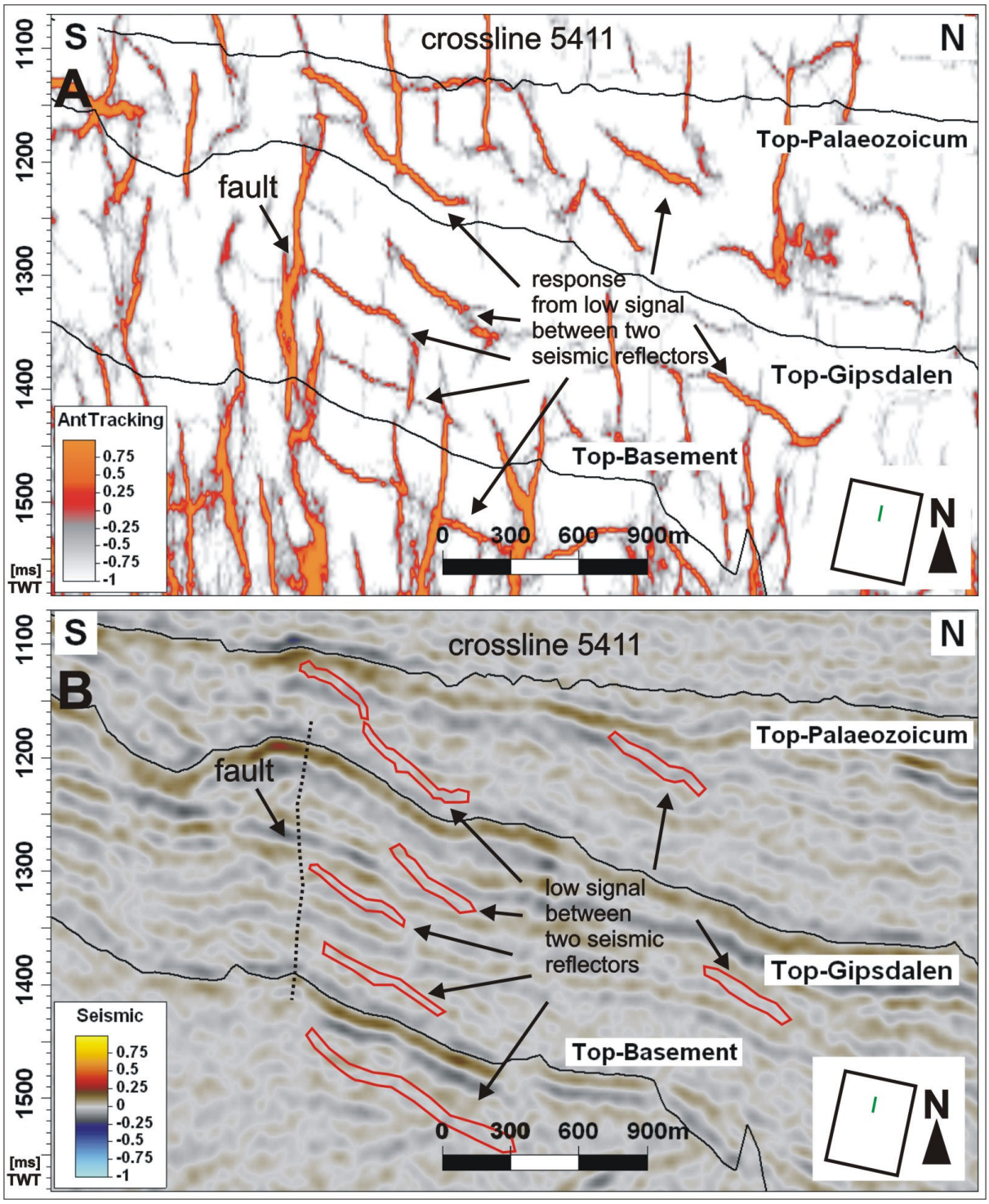

Figure 3.18 (A) Crossline 5411 from the study area of survey SG9810, displaying the result of the 'Chaos – Ant-tracking workflow'. Response from chaotic signal between two strong reflections is indicated by arrows. (B) Seismic crossline 5411. Position of chaotic signal between two reflections is indicated by the orange marked areas. Positions of one fault and the Top-Palaeozoic, the Top-Gipsdalen and the Top-Basement surfaces are indicated in both A and B.

3.5. Velocity model and depth conversion of seismic data

3.5.1. Seismic interpretation of the data

Six seismic surfaces, Seafloor, Top-Triassic, Intra-Snadd, Top-Palaeozoic, Top-Gipsdalen and Top-Basement (Figure 3.19A) were interpreted to be used as an input for the velocity model (Figure 2.9). The velocity model was applied to both the seismic cube and the interpreted surfaces to depth convert the data (Figure 3.19B). The depth converted data are useful for direct measurements of dimensions of the detected build-ups.

3.5.2. Dimensions of carbonate build-ups

The dimensions of the polygonal network build-ups were measured from the depth map of the Top-Gipsdalen surface (Figure 3.20, Figure 3.21) and the depth-converted seismic lines.

The length of the build-up ridges and the size of the build-ups differ between the ‘Area of the smaller build-ups’ and the ‘Area of the larger build-ups’ (Figure 3.6A). The build-up ridges are from 700 m to 4000 m long in the ‘Area of the smaller build-ups’ (Figure 3.21) and from 400 m to 7000 m long in the ‘Area of the larger build-ups’ (Figure 3.20). The build-ups in the ‘Area of the smaller build-ups’ have relief from the base of the lagoons in the range of 50 m to 300 m high and are 90 m to 350 m wide (Figure 3.21). The build-ups in the ‘Area of the larger build-ups’ have a relief between 150 m to 500 m high and are 110 m to 600 m wide (Figure 3.20).

There are also several enclosed lagoons visible on the Top-Gipsdalen surface. One of the measured lagoons in the ‘Area of the larger build-ups’ is ca. 1300 m to 1400 m wide and 150 m deep (Figure 3.20) and one of the measured lagoons in the ‘Area of the smaller build-ups’ is ca. 450 m to 650 m wide and 120 m deep (Figure 3.21).

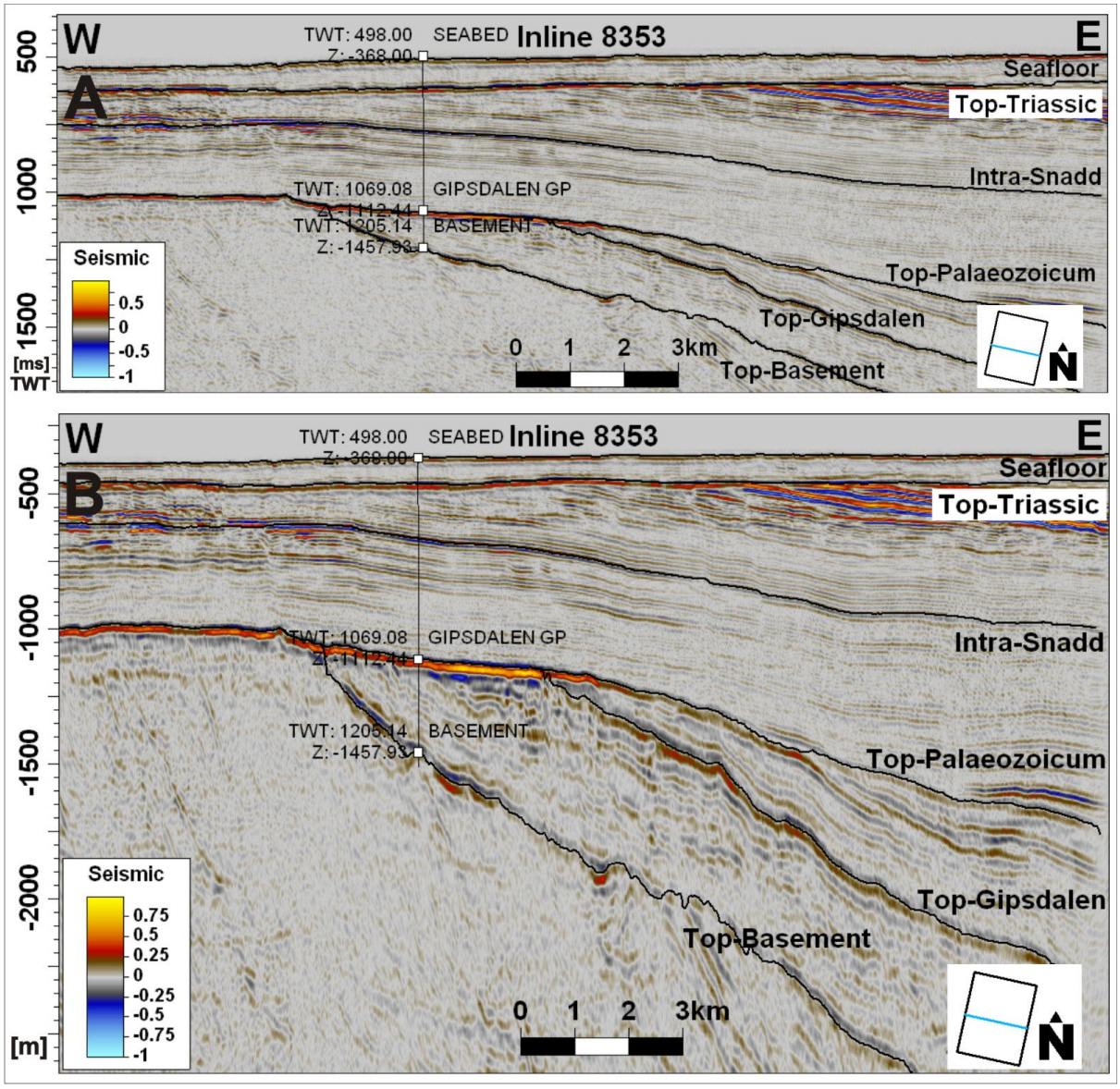

Figure 3.19 (A) Seismic inline 8353 displaying the Seafloor, the Top-Triassic, the Intra-Snadd, the Top-Palaeozoic, the Top-Gipsdalen and the Top-Basement surfaces in ms, two-way-travel time. (B) The same seismic line after the application of the depth conversion, displaying the converted surfaces in depth in metres. The well 7220/6-1 and its three well-tops are displayed.

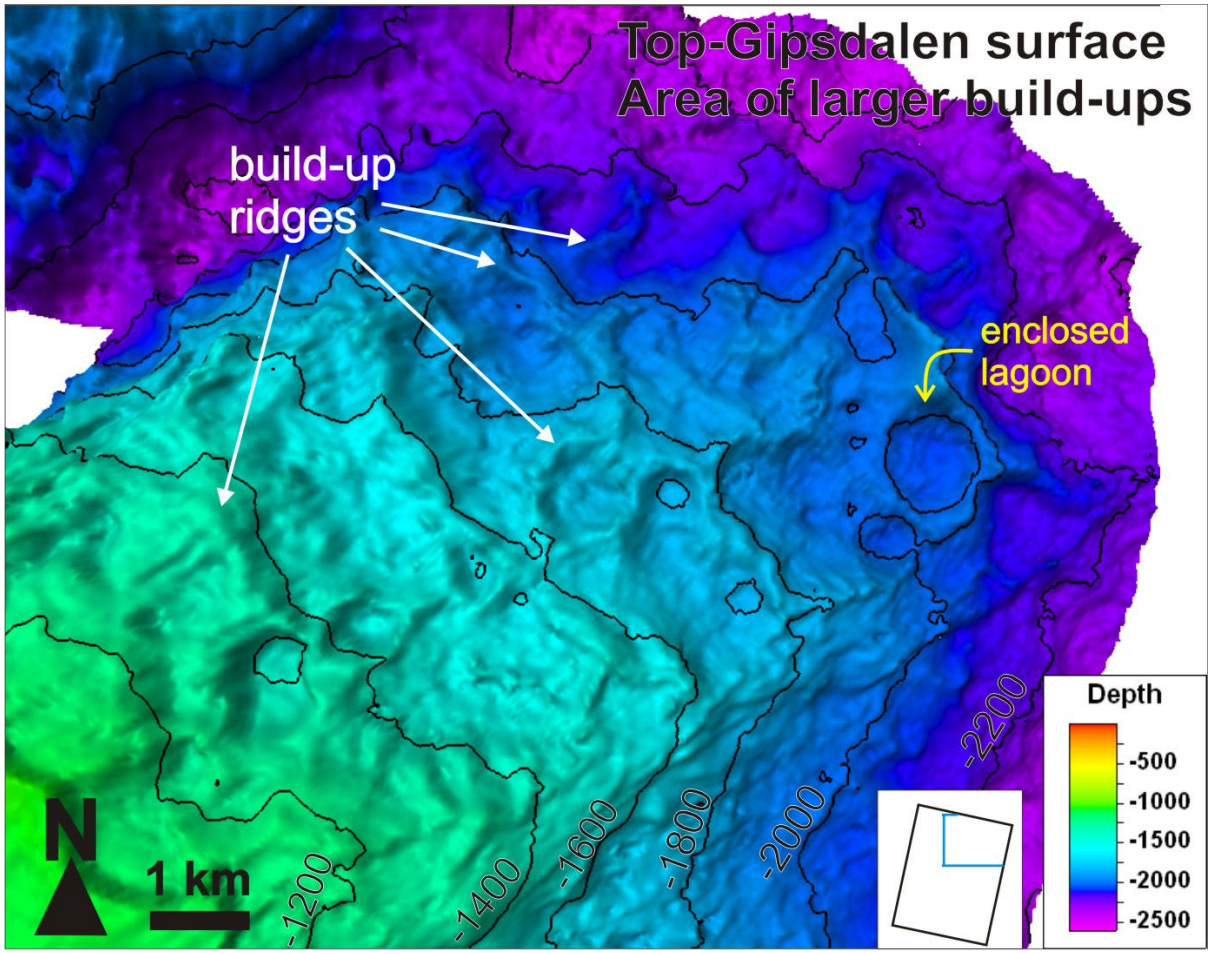

Figure 3.20 Depth converted Top-Gipsdalen surface, Area of larger build-ups. Some of the most pronounced build-up ridges and one enclosed lagoon are indicated.

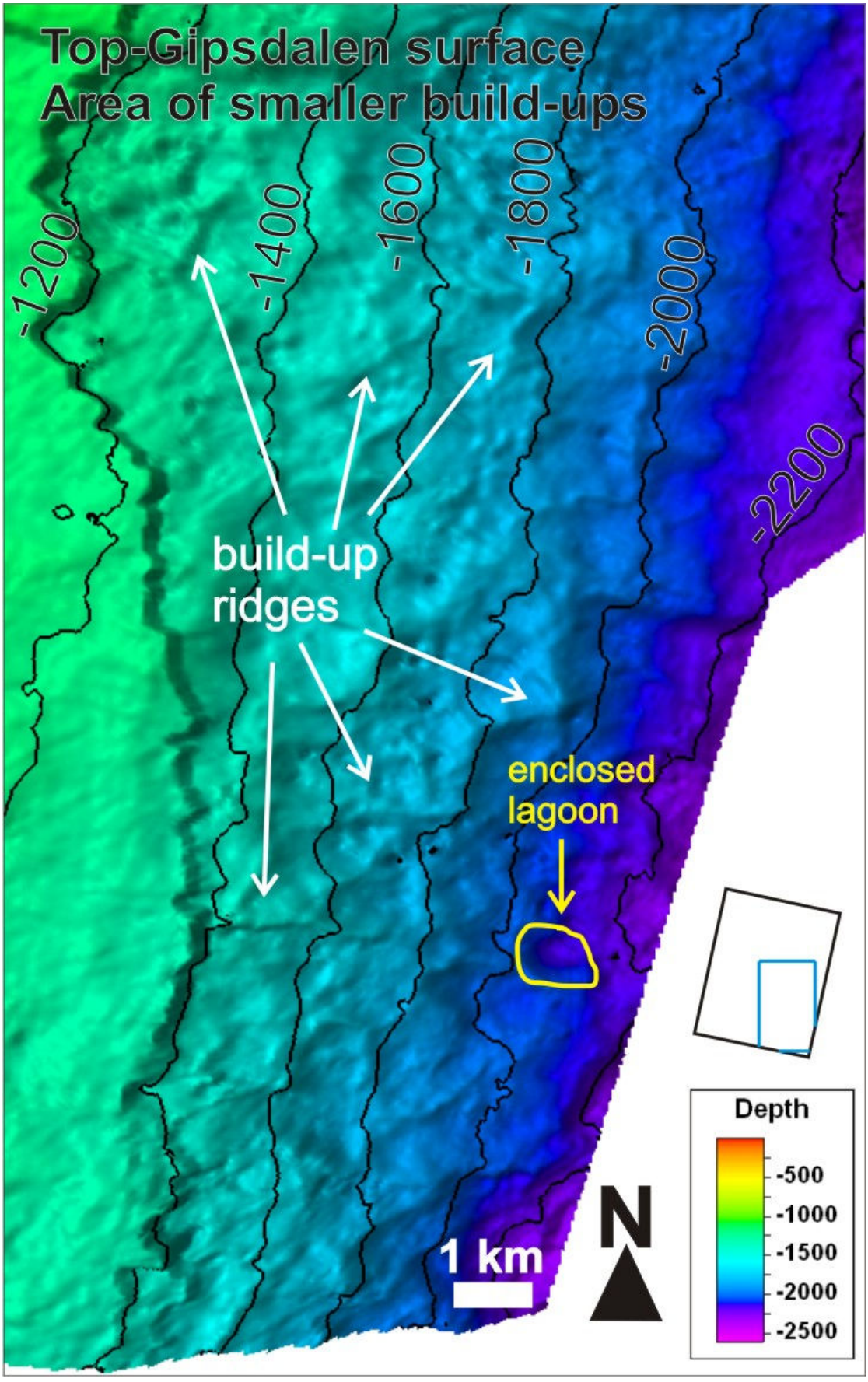

Figure 3.21 Depth converted Top-Gipsdalen surface, Area of smaller build-ups. Some of the most pronounced build-up ridges and one enclosed lagoon are indicated.

4. Discussion

4.1. Comparison of results of the Chaos – Ant-tracking workflow and the Variance – Ant-tracking workflow

The main difference between the 'Chaos Ant-tracking workflow' and the 'Variance – Ant-tracking workflow' is in the choice of an edge detection method: Chaos or Variance attribute cube. According to Petrel™ manual (Schlumberger, 2009b), the Chaos Attribute cube computes the local chaos – measure of the 'lack of organization' in the dip and azimuth estimation method and the Variance Attribute cube estimates the local variance in the seismic signal. Both of these methods are suitable for detecting edges in the seismic signal. However, the definition of an edge differs. In case of the Variance attribute cube, it refers to discontinuity in the horizontal continuity of amplitude, whereas the Chaos attribute cube detects discontinuities regardless the orientation. This also affects the final results of each of the workflows.

The Variance attribute cube (Figure 4.1C) is able to detect discontinuities more sharply than the Chaos attribute cube (Figure 4.1D). The faults detected by the Chaos attribute cube are wider and a bit blurred. However, the Variance attribute cube also has a disadvantage. Because this cube detects 'discontinuities in the horizontal continuity of amplitude', it creates relatively vertical artificial response in the result (Figure 4.2A). Depending on the data, this mostly creates a problem, when it comes to interpretation which features are real, and which are artefacts.

In this thesis two 3D seismic surveys were used, the northern part of the SG9810 and the high resolution NH0372 site survey (Figure 3.6A). These surveys have different resolution. The NH0372 survey has a six times denser acquisition grid and also better quality of the data. It is important to note that this influences the results of Ant-tracking, more precisely of the choice of the most suitable edge detection method for the Ant-tracking workflow, for each of the mentioned surveys. In the Triassic succession of the survey SG9810 (Figure 4.3, Figure 4.4) artificial response parallel to inline direction is clearly visible. This is detected by both Variance (Figure 4.3) and Chaos (Figure 4.4) attribute cube. These artefacts are not further detectable in the Palaeozoic succession. The interpretation of these artefacts is that they are

created by acquisition and processing of the data. The quality of the data is important for the results of Ant-tracking. The site survey NH0372 has not only higher resolution, but also, there were no acquisition footprints detected in any depth of the seismic volume. This is visible in results from the Variance attribute cube (Figure 4.1C) and also the Chaos attribute cube (Figure 4.1D), applied to the NH0372 site survey. The 750 ms timeslices (Figure 4.1C, D) also demonstrate higher resolution of the NH0372 site survey, detecting faults invisible in the same timeslices from the survey SG9810 (Figure 4.1A, B).

The Variance attribute cube can detect minor details, and depending on the data quality this can be positive for the result or negative. On the 1154 ms timeslice, of NH0372 site survey (Figure 4.5B), lagoon and a build-up ridge from the Top-Gipsdalen surface (Figure 3.10A, B) can be seen in the response of the Bjarmeland Group build-ups. On the same timeslice, of SG9810 survey (Figure 4.5A), is no response of the lagoon and the build-up visible. This lagoon and the build-up ridge are clearly visible on the Top-Gipsdalen surface in both surveys (Figure 3.10A, B, Figure 4.13C, D). On the 1314 ms timeslice (Figure 4.6) can be see a disadvantage on the Variance attribute cube (Figure 4.6A), as it is detecting artefacts of dipping reflections in the basement (Figure 4.2A, B, Figure 3.1A). These reflections are most likely not real, because they were not detected by the high resolution survey NH0372 (Figure 4.6B, Figure 3.1D).

Even if one Ant-tracking workflow gives good results, revealing faults in the area of interest, it is important to use at least two workflows with different parameters to quality-control the result. The results of the two workflows, customized for our objective, were compared. For 3D visualization of faults the results with clearer response were chosen: the ‘Chaos – Ant-tracking workflow’ for the study area of survey SG9810 and the ‘Variance – Ant-tracking workflow’ for the high resolution site survey NH0372.

4.1.1. Study area of 3D seismic survey SG9810

In the SG9810 study area, the ‘Chaos – Ant-tracking workflow’ gives the best results (Figure 4.2C, Figure 4.7A) and was used for 3D visualization of faults (*3.2 Final result of Ant-tracking – 3D visualization of faults and fractures connected to*

carbonate build-ups). Because of the character of the data, the Ant-tracking workflow with the Variance attribute cube as an edge detection method (Figure 4.2A, B, Figure 4.7B) detects more artefacts than the one with the Chaos attribute cube (Figure 4.7A). Even if the result of the 'Variance – Ant-tracking workflow' shows more information (Figure 4.2A, B), it is not easy to decide what is real and what is artificial response, as the most of the detected discontinuities are near to vertical (Figure 4.2A). To handle this problem, the Stereonet settings in the Ant-tracking workflow were customized to dips 20-80° (Figure 4.2B). This allows ants to look for discontinuities only with dips up to 80° (Figure 4.2B) and they are not allowed to find all the near to vertical discontinuities (Figure 4.2A). This may remove some of the real response as well, but the strongest response, considered being real, remains. An example of a real response is a fault indicated in figure 4.2 (A, B and C). This is one of the typical faults associated with build-ups and we can see that its response is clearly visible in all of the three displayed results of the Ant-tracking workflow (Figure 4.2A, B, C). Another reason, why the 'Chaos – Ant-tracking workflow' was chosen for 3D visualization, is that by removing the most vertical dips from the 'Variance – Ant-tracking workflow', the angles of the remaining (real) faults (Figure 4.2B) are not as realistic as those in the 'Chaos – Ant-tracking workflow' (Figure 4.2C). And finally, the 'Chaos – Ant-tracking workflow' was band-pass filtered in the first step, removing signal under 30 Hz. This enabled elimination of noise such as dipping reflections response occurring in the basement (Figure 4.2A, B, Figure 4.7B), and enhanced faults for further steps of the 'Chaos – Ant-tracking workflow'.

4.1.2. High resolution 3D seismic survey NH0372

Thanks to the high resolution and good quality of the data in NH0372 survey, both workflows, the 'Chaos – Ant-tracking workflow' (Figure 4.8B, D) and the 'Variance – Ant-tracking workflow' (Figure 4.8C, E) give very clear results, showing many structures, which can be easily interpreted as faults or fractures. Still, the clearest results are given by the 'Variance – Ant-tracking workflow' (Figure 4.8E). Therefore in this case, this workflow was used for 3D visualization of faults (*3.2 Final result of Ant-tracking – 3D visualization of faults and fractures connected to carbonate build-ups*). In the result of the 'Variance – Ant-tracking workflow' (Figure 4.8E) visible

faults and fractures are enclosing a lagoon, while the result of the 'Chaos – Ant-tracking workflow' (Figure 4.8D) reveals only the largest faults and shows also some scattered reflected signal, which seems more random than directly related to the build-ups' location. As mentioned before, the Variance attribute cube is detecting the discontinuities more sharply and therefore can find minor details in the data (Figure 4.9A) compared to the Chaos attribute cube (Figure 4.9B). In case of a high resolution good quality data (Figure 4.1C, D), the Variance cube (Figure 4.9A) can provide a better input into the Ant-tracking than the Chaos cube (Figure 4.9B). If visualized in three dimensions, it is easy to find out what is a real response and what is an artefact. The result of the 'Variance – Ant-tracking workflow' can be viewed as too vertical when seen for the first time (Figure 4.10A). However, the Ant-tracking workflow was tested, removing the maximum dips to 85° (Figure 4.10B) and to 80° (Figure 4.10C). The testing confirmed that the response is real when also dips up to 90° are allowed. In three dimensional view (Figure 4.10D, E, F) is clearly visible that the most precise result is the one when dips are 20-90°. It is important to note that all the displayed seismic lines are vertically exaggerated and in TWT, what visually makes the dips to be more vertical than they really are. These dips (Figure 4.10A) are mostly between ca. 83-89 degrees. These detected discontinuities are interpreted as sub-vertical syndepositional fractures associated to build-ups' positions.

The 'Chaos – Ant-tracking workflow' (Figure 4.8B, D) in the site survey NH0372 is still important for quality control of the result. Comparing the results of the two workflows with different parameters helps to distinguish the real and artificial response in the data. Especially the biggest faults are clearly visible in the results of both workflows (Figure 4.8B, C).

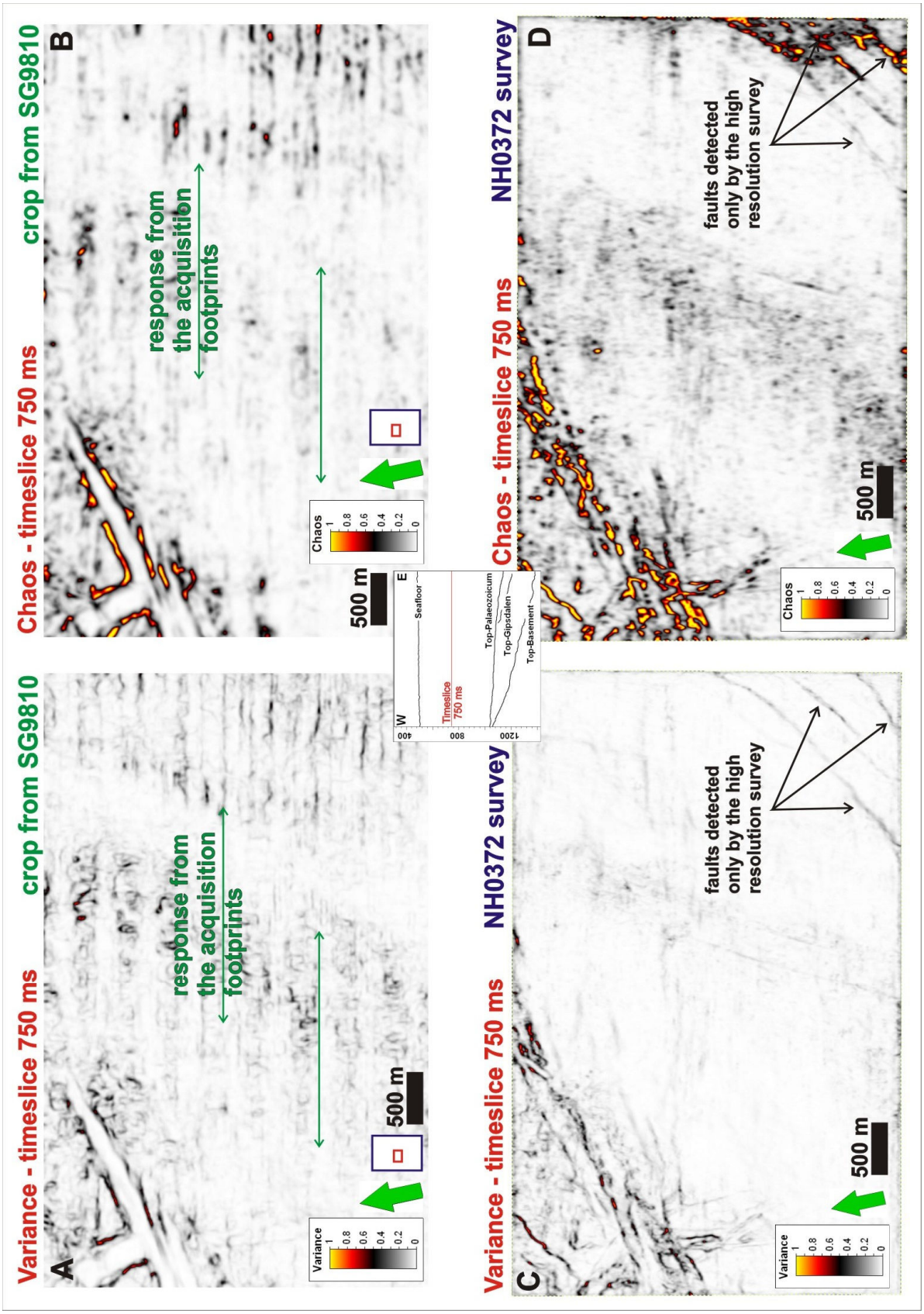

Figure 4.1 Time-slices at 750 ms. (A) Variance attribute cube, crop from study area of survey SG9810. Response from cquisition footprints is indicated. (B) Chaos attribute cube, crop from study area of survey SG9810. Response from acquisition footprints is indicated. (C) Variance attribute cube, survey NH0372. Detected faults are indicated. (D) Chaos attribute cube, survey NH0372. Detected faults are indicated.

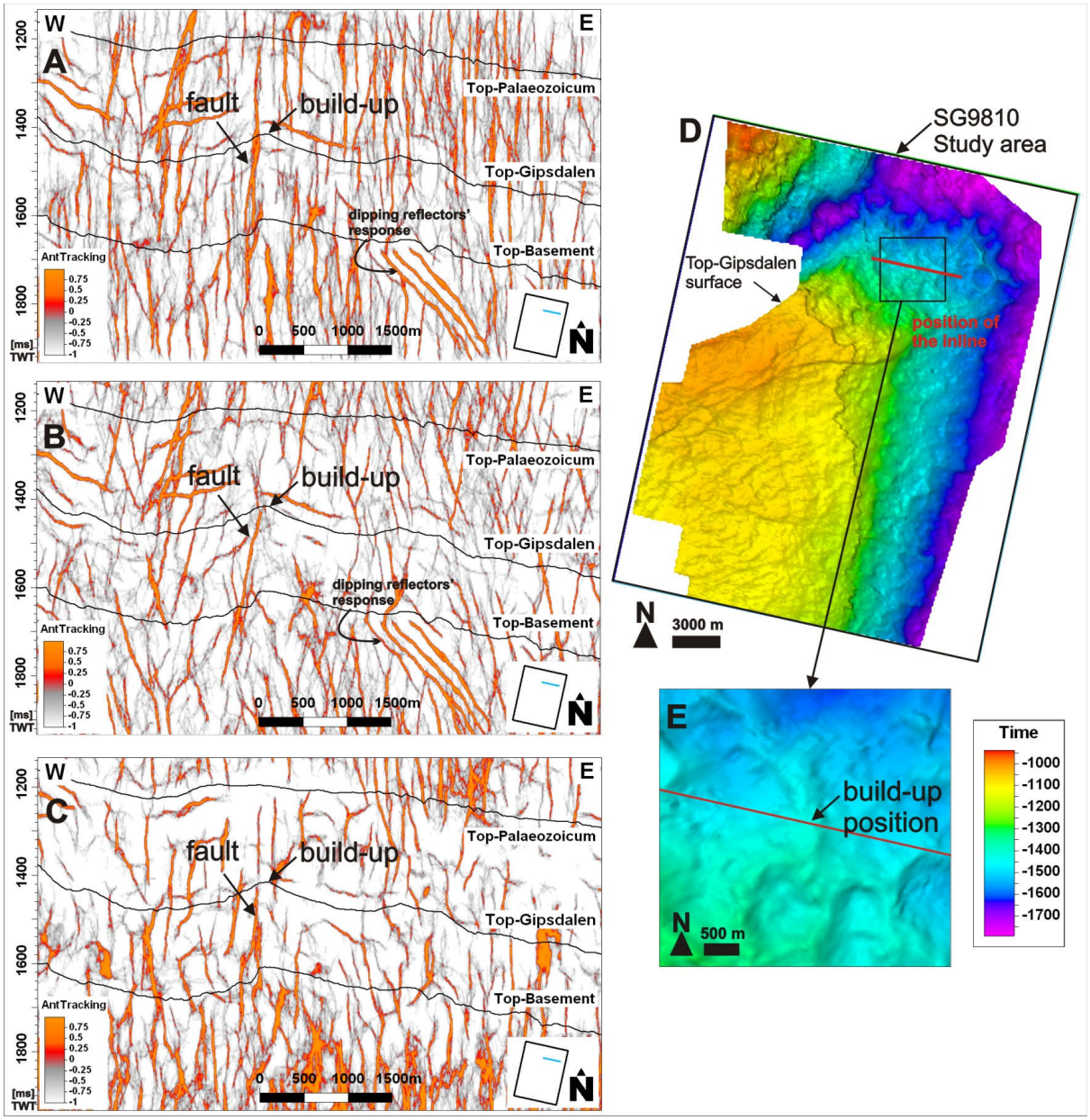

Figure 4.2 (A) The result of the 'Variance – Ant-tracking workflow'. The allowed dips for ants to look for discontinuities are 20-90° in this case. (B) The result of the 'Variance – Ant-tracking workflow'. The allowed dips for ants to look for discontinuities are 20-80° in this case. (C) The result of the 'Chaos – Ant-tracking workflow'. The allowed dips for ants to look for discontinuities are 20-90° in this case. In A, B an C are indicated positions of Top-Palaeozoicum, Top-Gipsdalen and Top-Basement surfaces, fault and build-up. In A and B is also indicated position of the dipping reflectors response. (D) The Top-Gipsdalen surface of the study area of 3D seismic survey SG9810. Position of the zoomed crop from E and the inline visualized in A, B and C is indicated. (E) Zoomed view of the Top-Gipsdalen surface. Position of the build-up visualized in A, B and C on the seismic inline is indicated.

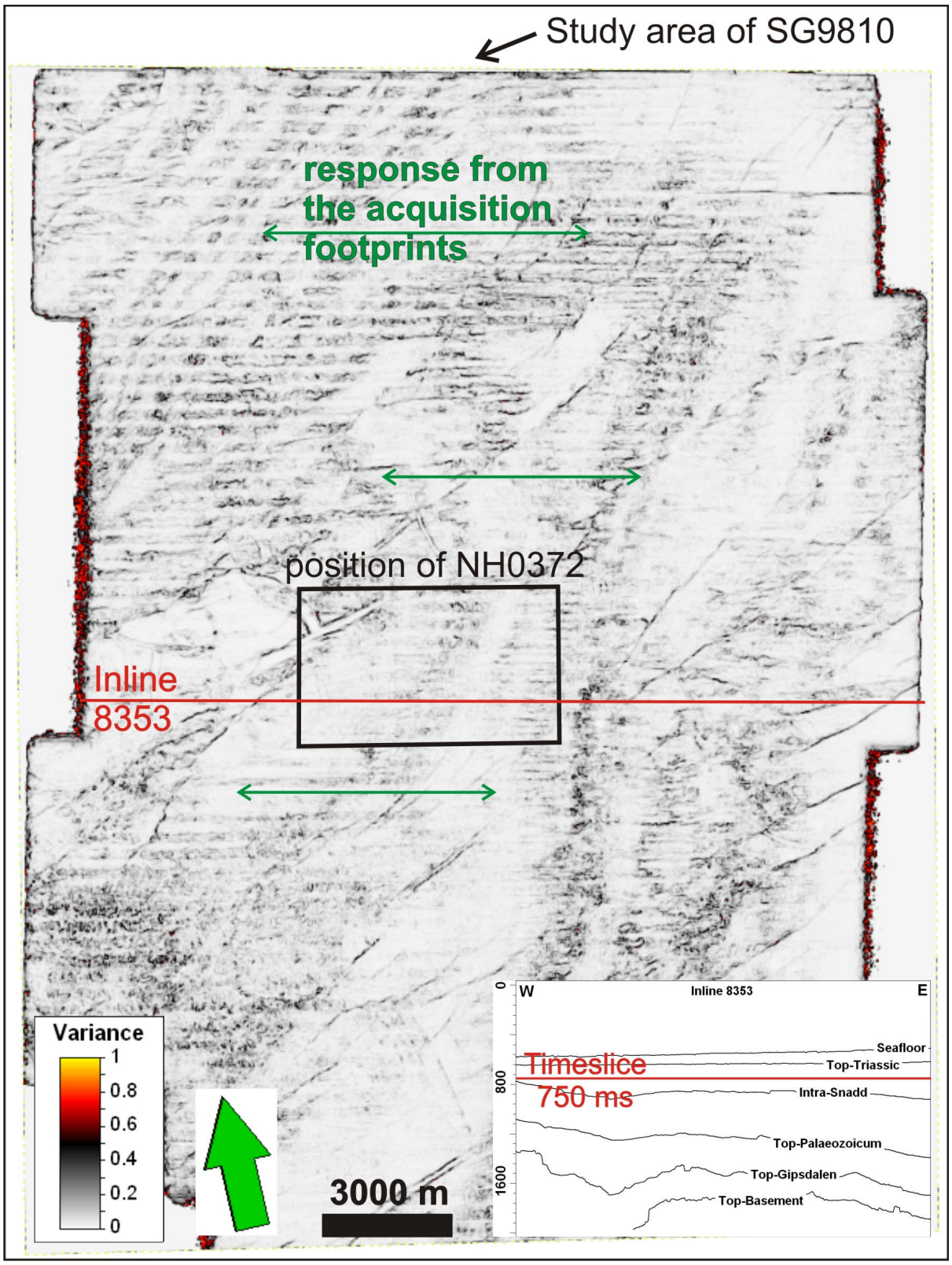

Figure 4.3 Time-slice at 750 ms from the Variance attribute cube, applied to the study area of survey SG9810. The time-slice is displaying response from the acquisition footprints in the Triassic succession and showing the positions of SW-NE trending faults. Position of NH0372 site survey is indicated.

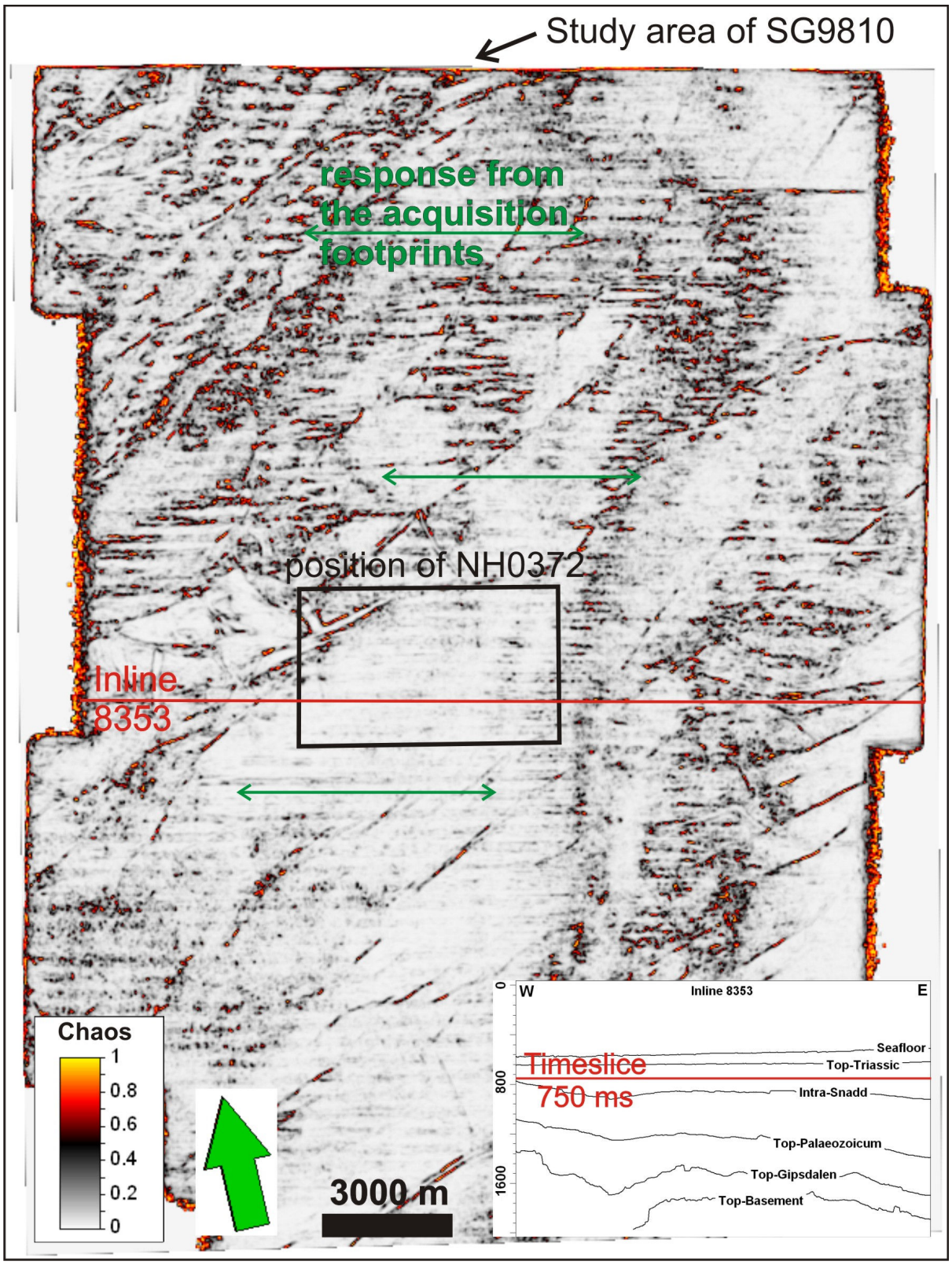

Figure 4.4 Time-slice at 750 ms from the Chaos attribute cube, applied to the study area of survey SG9810. The time-slice is displaying response from the acquisition footprints in the Triassic succession and showing the positions of SW-NE trending faults. Position of NH0372 site survey is indicated.

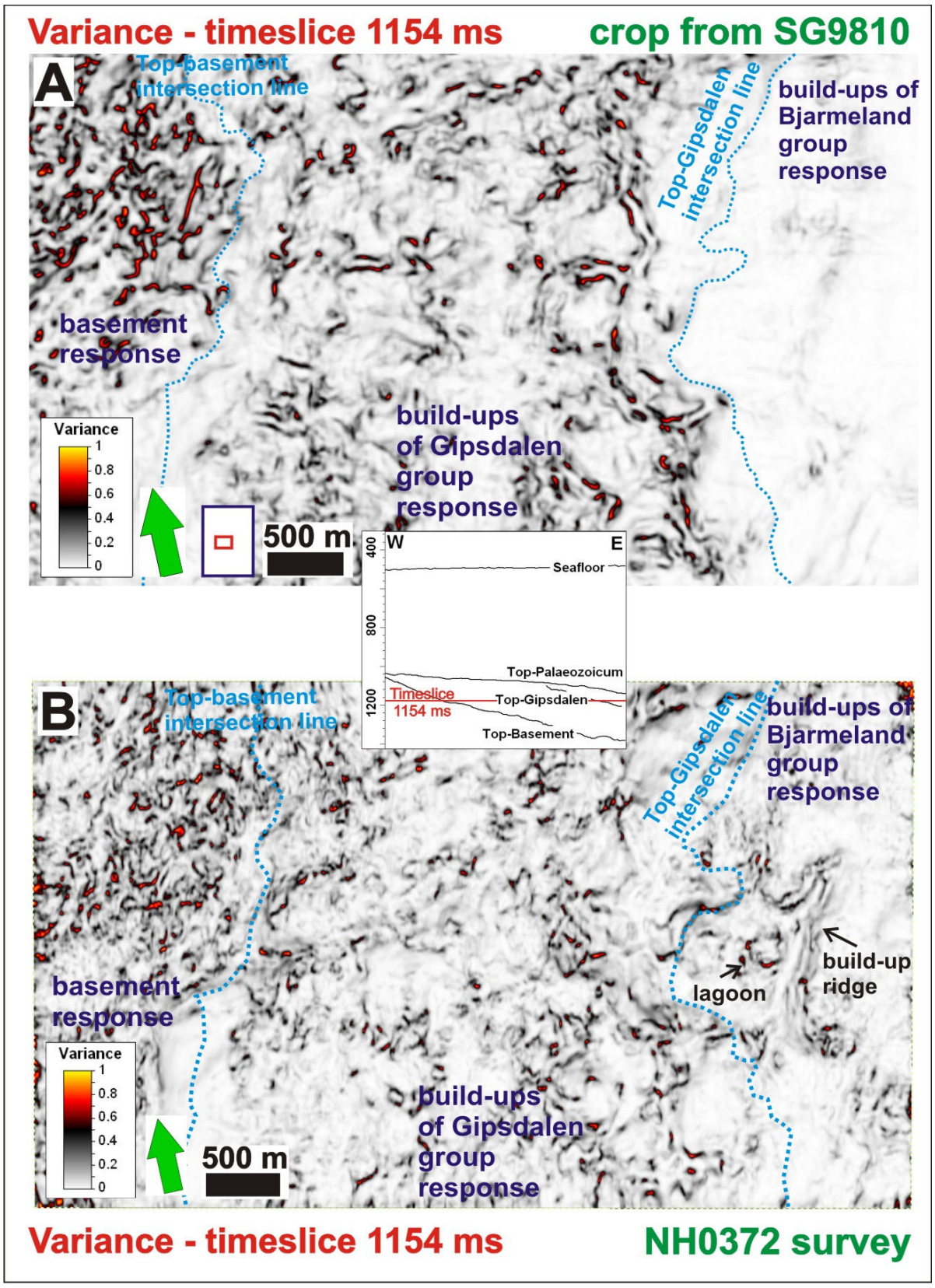

Figure 4.5 Time-slices at 1154 ms from the Variance attribute cubes. The time-slices are divided into areas with basement response, build-ups of Gipsdalen Group response and build-ups of Bjarmeland Group response. Intersection lines between the time-slices and Top-basement and Top-Gipsdalen surfaces are indicated. (A) Crop from the study area of survey SG9810. (B) The high resolution site survey NH0372. Response of lagoon and build-up ridge from the Top-Gipsdalen surface is visible in the response of build-ups of Bjarmeland Group.

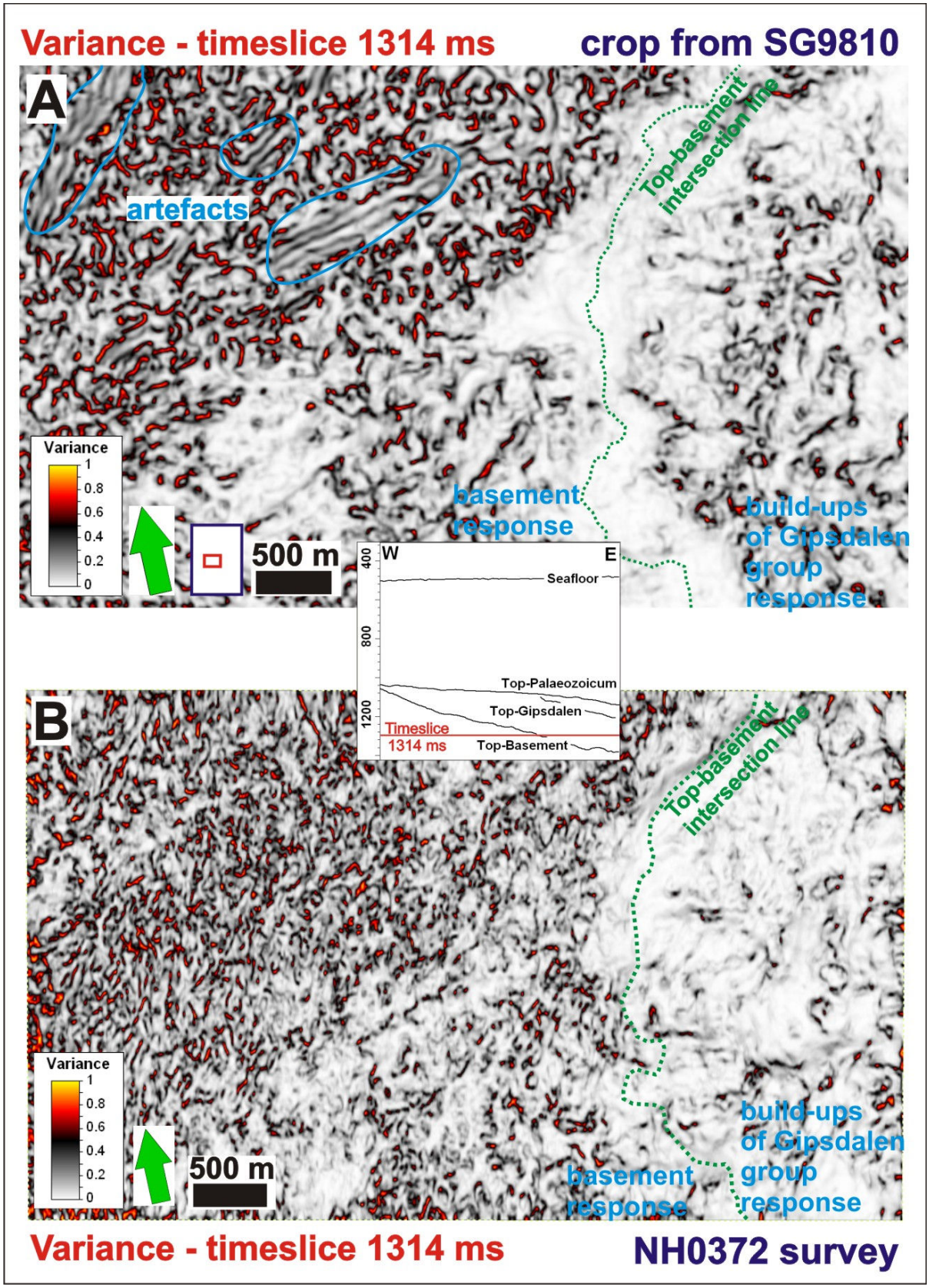

Figure 4.6 Time-slices at 1314 ms from the Variance attribute cubes. The time-slices are divided into areas with basement response and build-ups of Gipsdalen Group response. Intersection lines between the time-slices and Top-basement surfaces are indicated. (A) Crop from the study area of survey SG9810. Positions of artefacts are indicated. (B) The high resolution site survey NH0372.

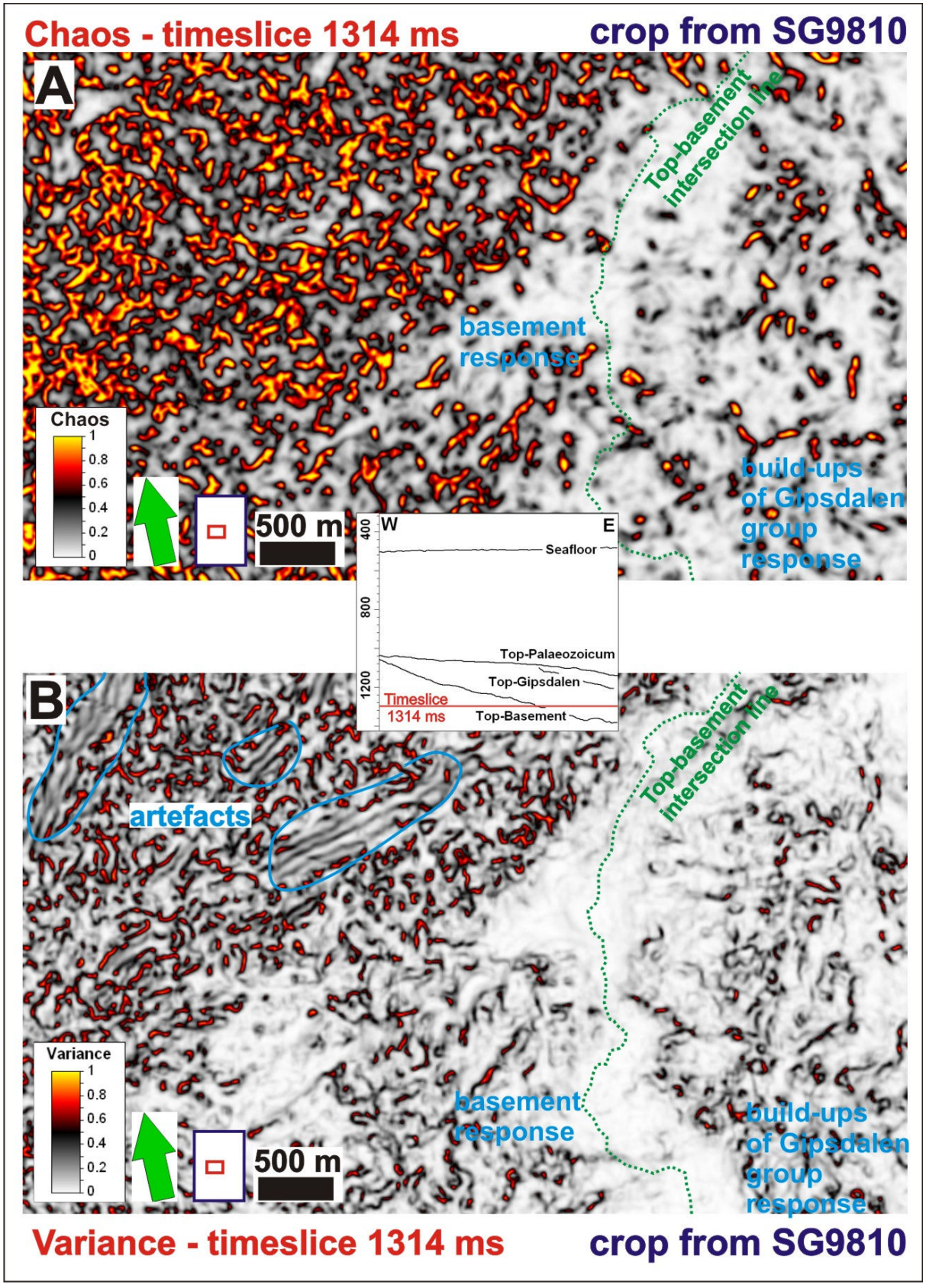

Figure 4.7 Time-slices at 1314 ms, crop from the study area of survey SG9810. The time-slices are divided into areas with basement response and build-ups of Gipsdalen Group response. Intersection lines between the time-slices and Top-basement surfaces are indicated. (A) Chaos attribute cube. (B) Variance attribute cube. Positions of artefacts are indicated.

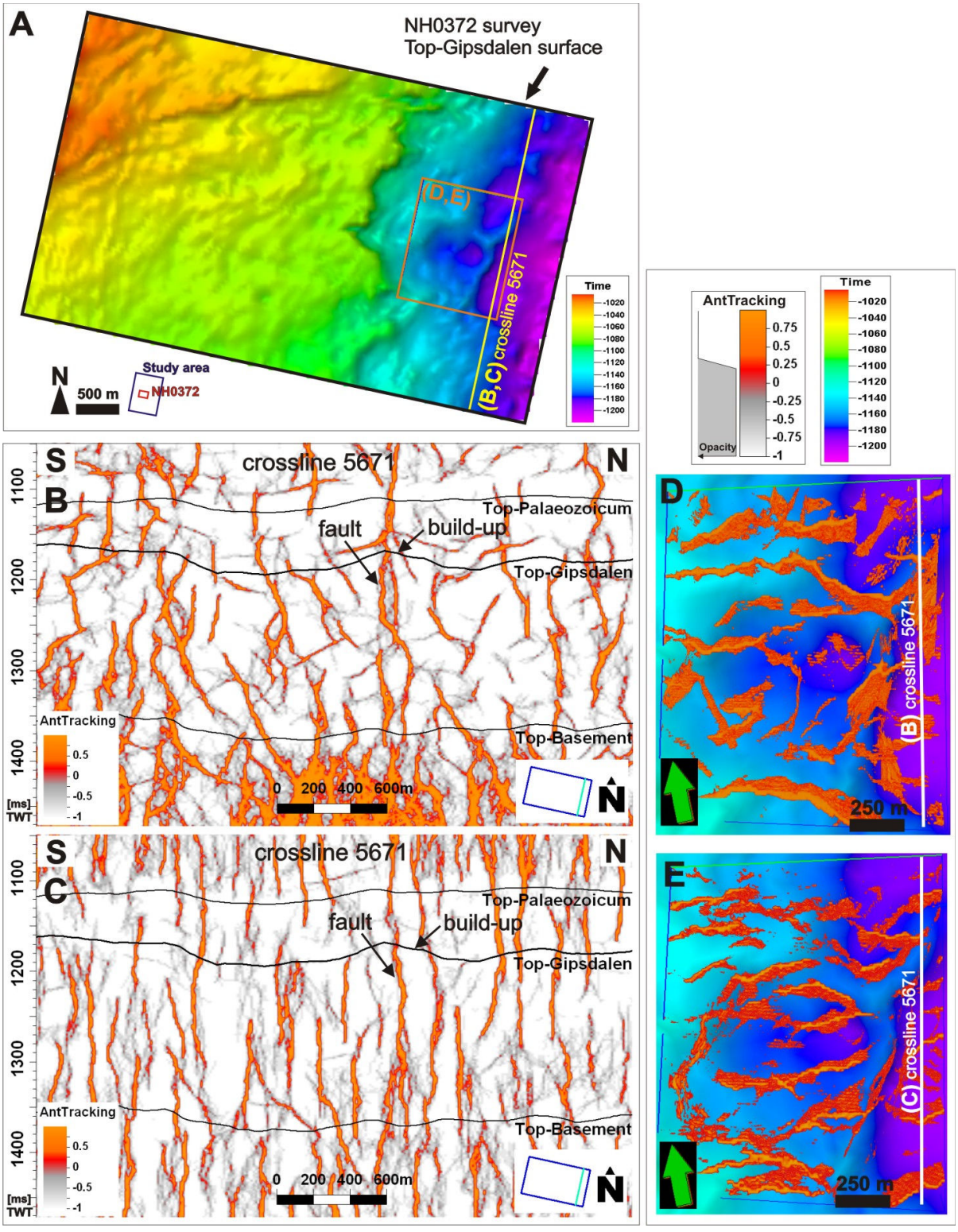

Figure 4.8 (A) The Top-Gipsdalen surface of the high resolution survey NH0372. Positions of the zoomed crops from D and E, and the crossline 5671 visualized in B and C are indicated. (B) The result of the 'Chaos – Ant-tracking workflow'. The allowed dips for ants to look for discontinuities are 20-90° in this case. (C) The result of the 'Variance – Ant-tracking workflow'. The allowed dips for ants to look for discontinuities are 20-90° in this case. Positions of Top-Palaeozoicum, Top-Gipsdalen and Top-Basement surfaces, fault and build-up are indicated. (D) Zoomed view of the Top-Gipsdalen surface of survey NH0372. Positions of faults detected by the 'Chaos – Ant-tracking workflow' are visualized in orange color. (E) Zoomed view of the Top-Gipsdalen surface of survey NH0372. Positions of faults detected by the 'Variance – Ant-tracking workflow' are visualized in orange color.

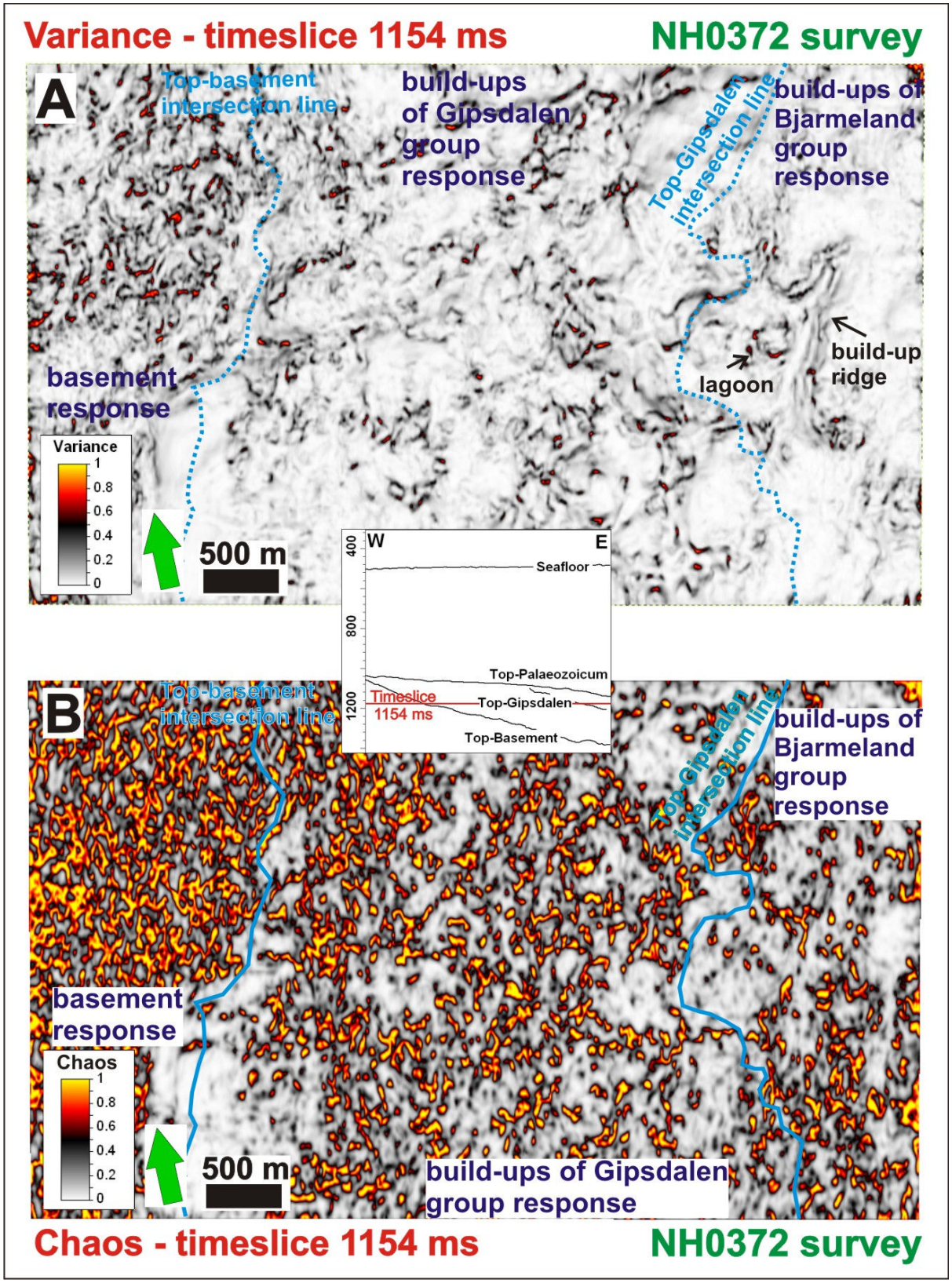

Figure 4.9 Time-slices at 1154 ms, the high resolution site survey NH0372. The time-slices are divided into areas with basement response, build-ups of Gipsdalen Group response and build-ups of Bjarmeland Group response. Intersection lines between the time-slices and Top-basement and Top-Gipsdalen surfaces are indicated. (A) Variance attribute cube. Response of lagoon and build-up ridge from the Top-Gipsdalen surface is visible in the response of build-ups of Bjarmeland Group. (B) Chaos attribute cube.

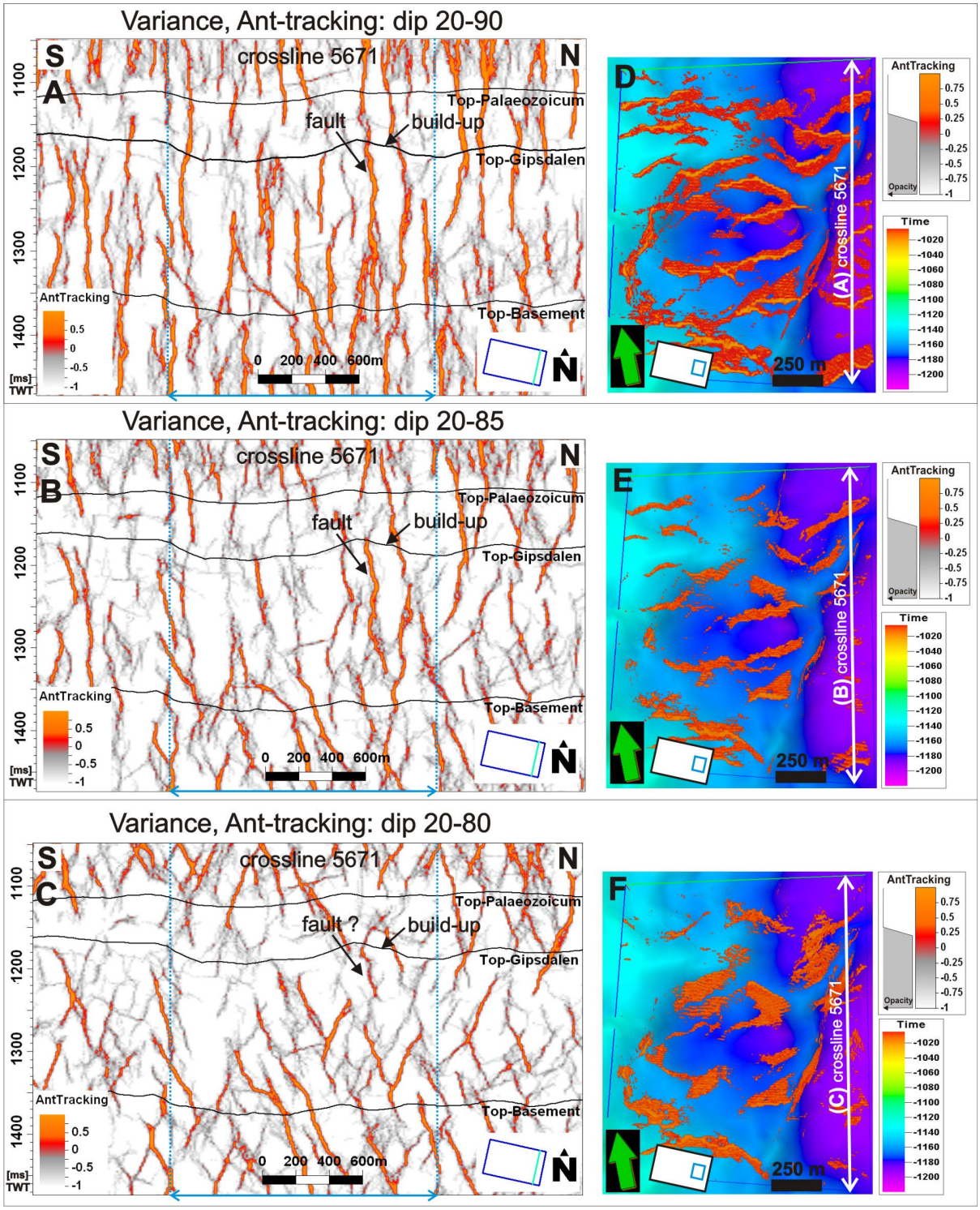

Figure 4.10 The result of the 'Variance – Ant-tracking workflow' applied to the high resolution site survey NH0372. (A) The allowed dips for ants to look for discontinuities are 20-90°. (B) The allowed dips are 20-85°. (C) The allowed dips are 20-80°. Positions of Top-Palaeozoicum, Top-Gipsdalen and Top-Basement surfaces, fault and build-up are indicated in A, B, C. (D, E, F) Zoomed view of the Top-Gipsdalen surface. Positions of faults detected in the seismic line to the left are visualized in orange color.

4.2. Development of build-ups and their associated syndepositional faults and fractures

Application of the Ant-tracking workflow revealed that the locations of carbonate build-ups in the Loppa High study area are directly associated with locations of faults and fractures. All the detected build-ups are associated with one or two faults or fractures. There were detected no build-ups, which could be claimed to be clearly 'fault-less'. In this chapter, I will describe my interpretation (Figure 4.11) of development of the carbonate build-ups and their associated syndepositional faults and fractures.

According to Gabrielsen et. al (1990) NE-trending faulting and block faulting occurred in the Loppa High area in Late Carboniferous – Early Permian. This is the time span when the Gipsdalen Group was deposited (Figure 4.12). The Gipsdalen Group was deposited during a period of high-frequency and high-amplitude glacioeustatic sea-level changes (Figure 1.7) (Stemmerik and Worsley, 1989). Carbonate build-ups started to develop during the Falk Formation, but their main development took place during the Ørn Formation (Figure 4.12). The Falk Formation (Figure 4.11A, Figure 4.12) represents the transition into shallow marine deposition, from non-marine deposition during Ugle Formation (Figure 4.12). The Falk Formation contains mixed carbonates of shallow marine facies, siliciclastics, conglomerates and shales (Larssen *et al.*, 2002). The Ørn Formation was deposited in alternating shallow and deeper marine carbonate environments during periods when the sea flooded the high (Larssen *et al.*, 2002). The deposition of carbonate build-ups took place most likely during sea level highstands (Figure 4.11E, F, H). During lowstands, the Loppa High was an island exposed to effects of weathering (Figure 4.11C, D, G). The glacioeustatic sea-level changes took place contemporaneously with the NE-trending faulting and block faulting and resulted in gradual eastward tilting of the sea floor, creating a ramp (Figure 4.11B-H). It also disrupted already deposited carbonate rocks, creating primary fractures and faults (Figure 4.11B). The climate during this time was warm and semi-arid to arid (Steel and Worsley, 1984, Stemmerik and Worsley, 1989, Stemmerik, 2000), but that was enough to begin karstification of the existing faults and fractures (Figure 4.11D). The infiltrating water

exploited faults and fractures and over time they became bigger and more pronounced (Figure 4.11D).

Organisms creating carbonate build-ups of the Gipsdalen Group, at the Loppa High, are mainly *Palaeoplysina*, often associated with phylloid algae. Palaeoplysina dominated build-ups are known from shallow water environments. In deeper water environments are common bryozoan-dominated build-ups. Organisms creating carbonate build-ups like to attach to a rigid skeleton and topographic elevation (Scoffin, 1987). The optimal growth position is along the footwall margin of fault block, which represents bathymetric high at the sea floor (Figure 4.11F, H). Highs are subjected to higher current energy, which also leads to an increased supply of nutritients necessary for build-up nucleation and growth. The main fault orientation in the study area is NE-SW. Tectonism during the deposition of the build-ups provided initial fractures and faults (Figure 4.11B, C) and gradual tilting of the ramp (Figure 4.11B-H). Build-ups also need an adequate water depth, deep enough to be below the wave base and shallow enough to get necessary sunlight for photosyntesis. In the areas with build-ups with large relief, the rate of build-up growth was able to keep the top of the build-up within the optimal water depth limit for build-up growth. The growth of buildups mirrors the faulted terrain and formes a mosaic of build-ups referred to as polygonal network build-ups described by Elvebakk et al. (2002).

The composition of Falk and Ørn formations differs and the growth of build-ups takes part mainly during the Ørn Formation (Figure 4.12), that is why I have interpreted that the faulting of the ramp got more intense at the end of the deposition of the Falk Formation and the beginning of the Ørn Formation (Figure 4.11A, B). High-frequency and high-amplitude glacioeustatic sea-level changes secured lowstands (Figure 4.11C) exposing the Loppa High for karstification (Figure 4.11D, G), allowing karst enlargement of faults and fractures. Extensive karstification may have taken place also during periods of mixing of meteoric and marine waters, during initial transgression of the ramp and during gradual sub-aerial emerging of the Loppa High. The high-frequency and high-amplitude glacioeustatic sea-level changes also secured highstands with convenient water depth for carbonate build-ups' deposition (Figure 4.11F, H). During a highstand, organisms attach to the topographic elevations of an uneven surface of karstified faults (Figure 4.11F). Later build-ups

grow on topographic elevations created by older build-ups (Figure 4.11H), creating hundreds of meters high stacked build-ups and long build-up ridges (Figure 3.20, Figure 3.21). Sea-level changes were frequent in the time of deposition of carbonate build-ups at the Loppa High. This enabled the faults and the build-ups to grow together (Figure 4.11F, G, H).

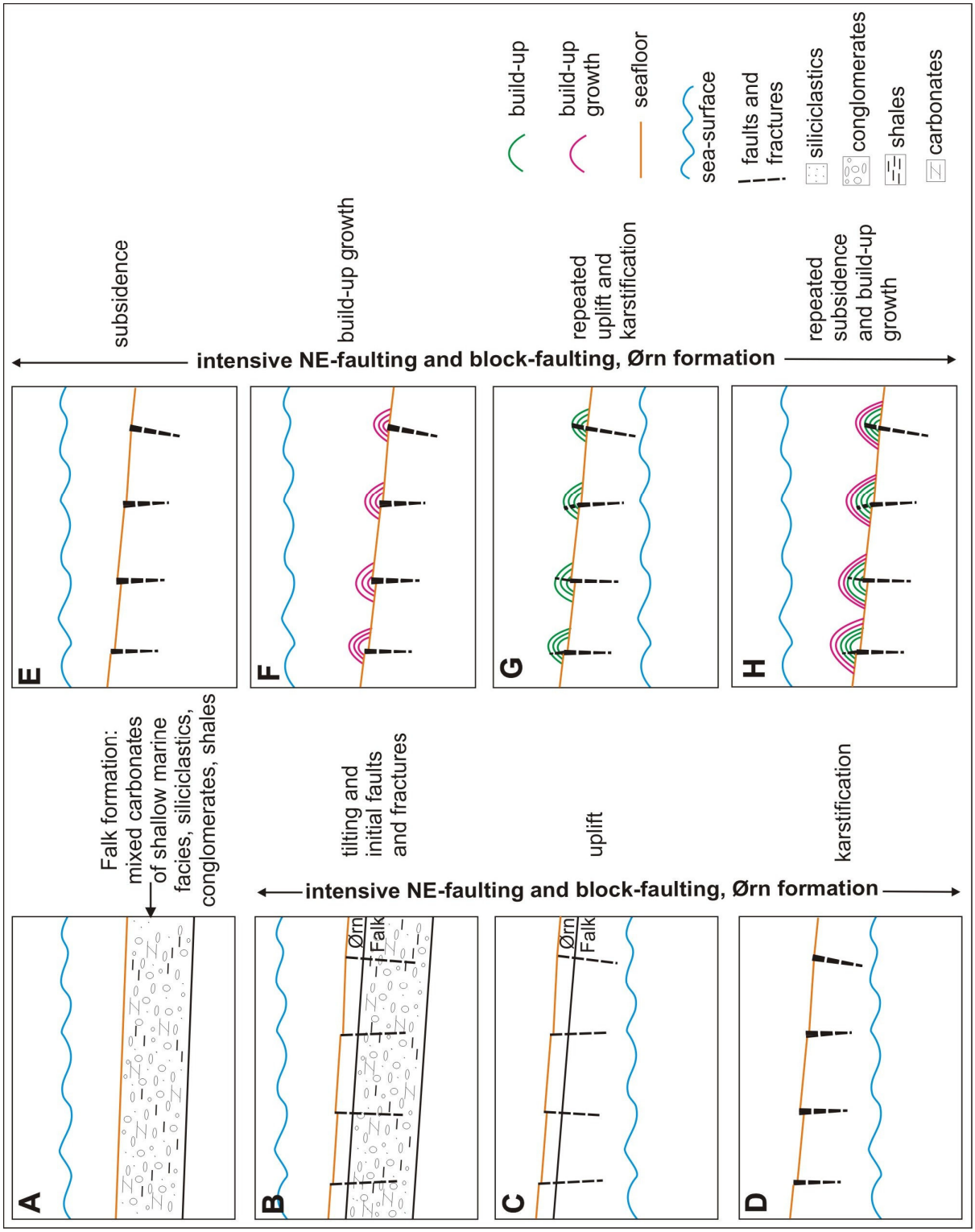

Figure 4.11 Summary figure of the interpretation of development of the carbonate build-ups and their associated syndepositional faults. (A) Deposition of Falk Formation during Moscovian. (B) Intensification of NE-faulting and block faulting which took place in Late Carboniferous – Early Permian, causing tilting, creating ramp and faults and fractures. (C) Uplift of the Loppa High during glacioeustatic sea-level changes. (D) Karstification of faults and fractures during the uplift. (E) Subsidence of the Loppa High during glacioeustatic sea-level changes. (F) Initial build-up growth on topographic elevations created by karstified faults and fractures during the subsidence. (G) Repeated uplift with continued karstification of faults and fractures and build-ups. (H) Repeated subsidence with continued build-up growth on older build-ups.

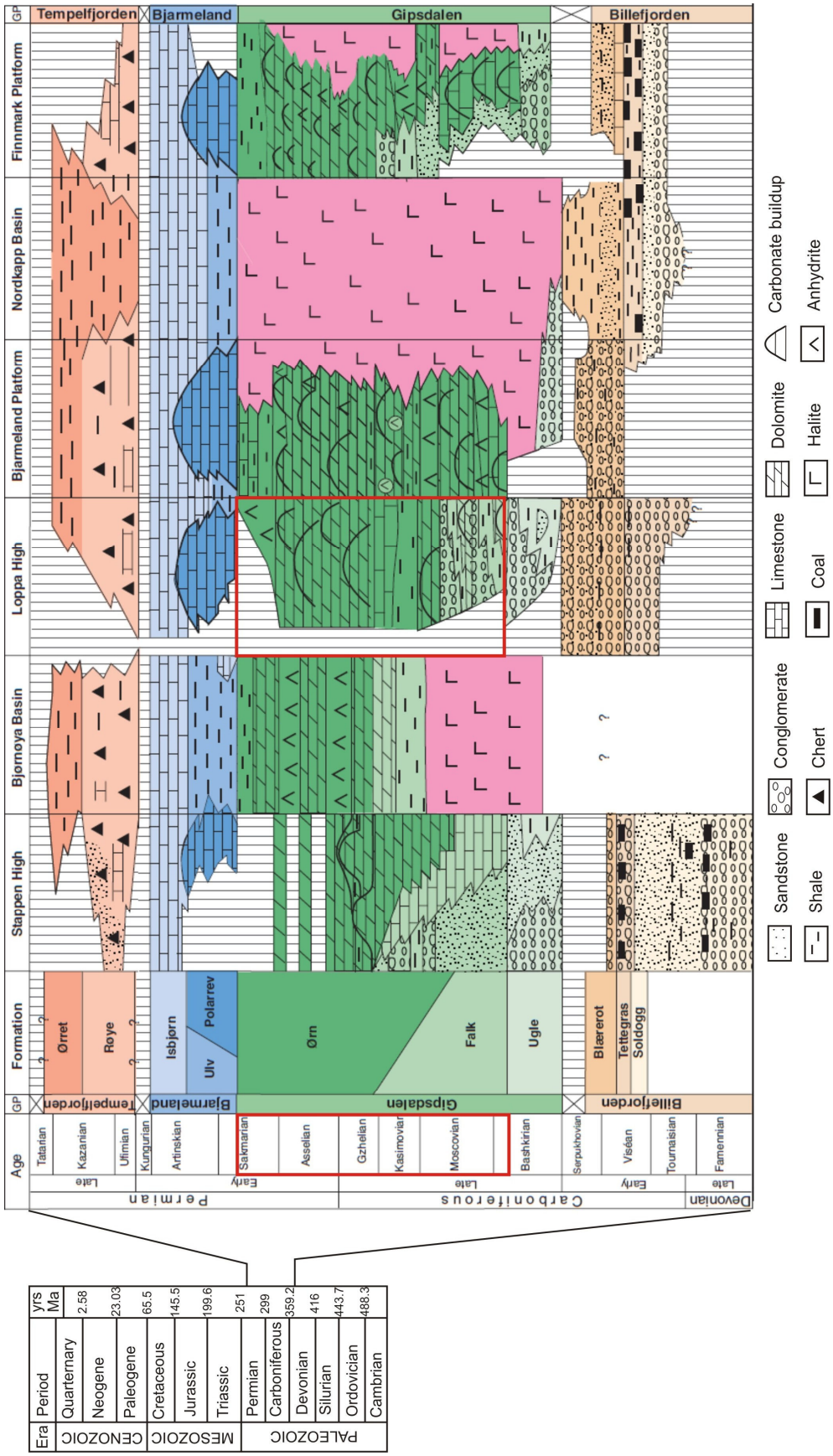

Figure 4.12 Correlation of Upper Palaeozoic lithostratigraphic units in the offshore areas of the southern Norwegian Barents Sea (modified from Larssen *et al.*, 2002). The stratigraphical interval studied in the thesis is indicated by red rectangles.

4.3. The Area of larger build-ups versus the Area of smaller build-ups

The area of larger build-ups – NE in the study area, and the area of smaller build-ups – SE in the study area are divided by a SW-NE major fault (Figure 3.6A). The fault is dividing the ramp into two segments, fault blocks. SW-NE trends of faulting and block faulting occurred on the Loppa High during Late Carboniferous – Early-Permian (Gabrielsen *et al.*, 1990), during the deposition of the Gipsdalen Group. The dip angle of the two ramp segments differs, with the steeper ramp in the 'Area of smaller build-ups' (Figure 3.6A). The subsidence of the fault block of this ramp was faster. The conditions, for build-ups' growth, were more favourable in the NE - 'Area of larger build-ups' (Figure 3.6A). The carbonate build-ups in the NE-area had grown larger (up to 500 m high and 600 m wide), creating longer build-up ridges (up to 7000 m) and enclosing deeper and larger lagoons (1300 m of diameter) (Figure 3.20) than the build-ups in the 'Area of smaller build-ups' (Figure 3.21). However different size of the build-ups doesn't seem to have any effect on position, size or angle of associated faults and fractures (Figure 3.7, Figure 3.9).

4.4. Faults and fractures in the study area of 3D seismic survey SG9810 versus the high resolution 3D seismic survey NH0372

In the high resolution site survey NH0372, the Ant-tracking workflow reveals many more faults and fractures (Figure 4.13C) compared to the results from study area of SG9810 (Figure 4.13D). In the chosen area (Figure 4.13C, D) a lagoon is visible, enclosed by the polygonal network build-ups. The Ant-tracking result from the NH0372 survey (Figure 4.13C) reveals many faults and fractures on the sides of the ridges of polygonal network build-ups, while the Ant-tracking result from the SG9810 survey (Figure 4.13D) reveals only some of them. The faults detected in the high resolution survey NH0372 are also often smaller an in more detail compared to the results from survey SG9810. In NH0372, the associated faults and fractures were detected also on the slopes of tiny - only several tens of metres high build-ups (Figure 3.10C – faults 5 and 6).

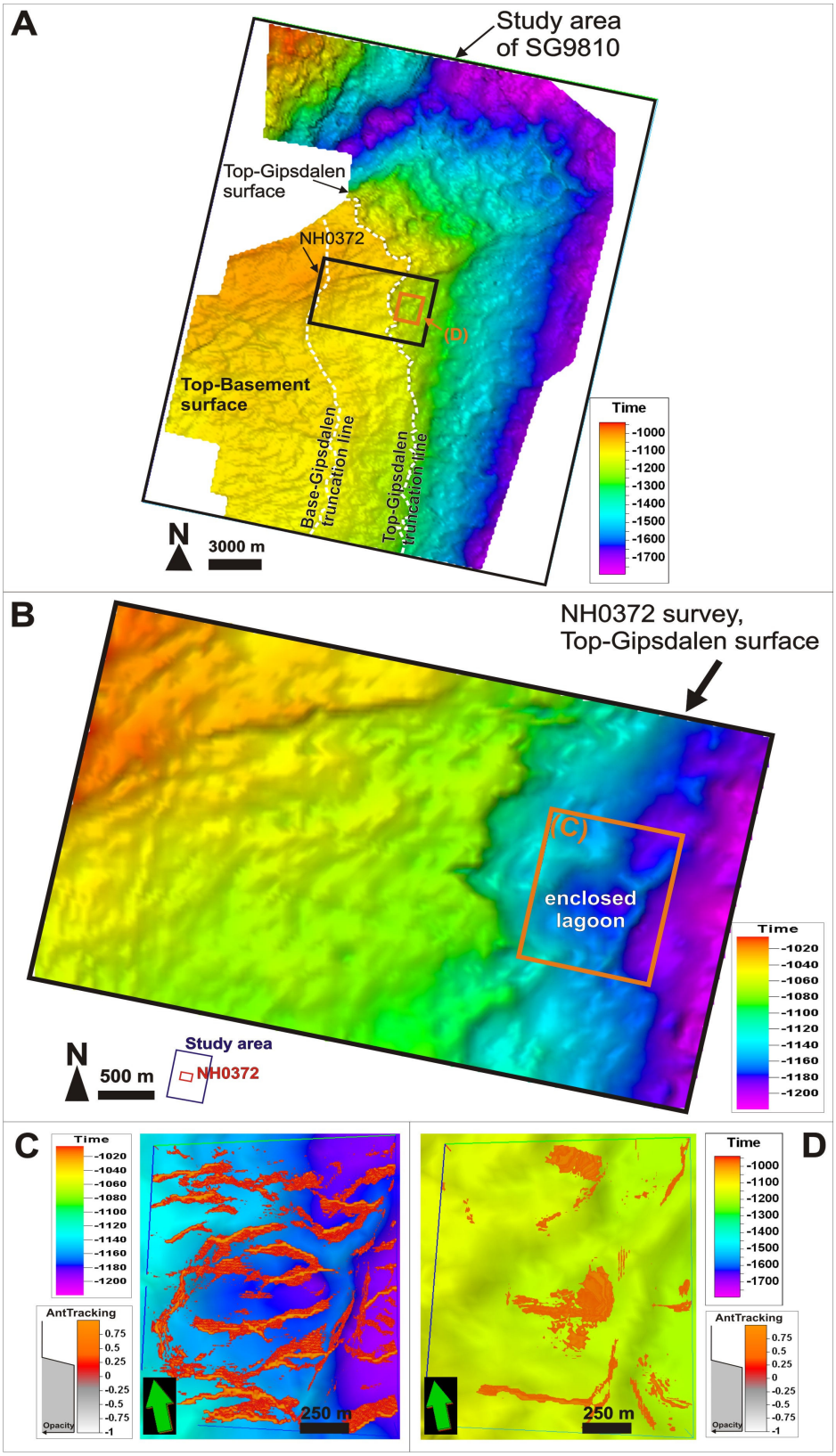

Figure 4.13 (A) The Top-Gipsdalen surface and a part of the Top-Basement surface of the study area of survey SG9810. Positions of the high resolution survey NH0372, the zoomed crop from D and the Top-Gipsdalen and the Base-Gipsdalen truncation lines are indicated. (B) The Top-Gipsdalen surface of the high resolution site survey NH0372. Positions of the zoomed crop from C and enclosed lagoon are indicated. (C) Zoomed view of the Top-Gipsdalen surface of site survey NH0372. (D) Zoomed view of the Top-Gipsdalen surface of the study area of survey SG9810. Positions of faults in C and D, generated by the Ant-tracking workflow are visualized in orange color.

4.5. Faults and carbonate build-ups – comparison with previous research

Application of the Ant-tracking workflow in this study revealed that locations of carbonate build-ups in the Loppa High are directly associated with locations of faults and fractures. It revealed that all the carbonate build-ups are associated with one or two faults or fractures, and there were no build-ups detected, which could be claimed to be clearly 'fault-less'.

Elvebakk et al. (2002) showed that the carbonate build-ups of the Loppa High are connected into a mosaic of build-up ridges, enclosing polygonal lagoons. They also observed the connection between locations of the build-up ridges and the mapped positions of syndepositional faults. This observation was made by mapping the faults manually directly from the 3D seismic data in the Loppa High area, survey SG9810. The same survey was used also in this study, together with the high resolution site survey NH0372. In this thesis, an effective method for semi-automated detection of faults – the Ant-tracking workflow was applied to the seismic data. This approach reveals all the faults and fractures within the seismic resolution of the data. The use of the Ant-tracking method not only confirmed the observation made by Elvebakk et al. (2002) but revealed that all the detected build-ups, with no exceptions, are growing directly on an associated fault/fracture or two.

Carrillat et al. (2005) was mapping carbonate build-ups and palaeokarst in the Loppa High area, also using 3D seismic survey SG9810. Their study area was in the southern part of the seismic survey, while the study area of this thesis was in the northern part of the seismic survey. They used a 3D multi-attribute mapping method to map different seismic facies in the data. Even if the main objective of that study was to map carbonate build-ups and palaeokarst, the visualisation of the palaeokarst revealed fault control on the location of the build-ups. Carrillat's finding directly supports the authenticity of the results in this thesis, because, in this case, the faults associated with build-ups were detected by a different semi-automated mapping method, which main objective was not to detect faults. This supports the claim that faults and fractures in carbonate build-ups in the Loppa High area are real and their locations are directly associated with locations of carbonate build-ups.

Also Rafaelsen et al. (2003a, 2008) observed connection between location of carbonate build-ups and location of faults. They also described connection between location of carbonate build-ups and the sea floor morphology at the time of their deposition. That observation was made from the study of 3D seismic data at the Finnmark Platform in the Barents Sea. The findings of the study carried out in this thesis agree with the findings from the Finnmark Platform. As described in *4.2 Development of build-ups and their associated syndepositional faults and fractures*, faults and fractures and especially karstified faults and fractures may create an uneven surface, which the build-up forming organisms prefer to attach to.

Hovland et al. (1994) studied relationship between carbonate build-ups and faults in the Porcupine Basin, offshore Ireland and in the Vulcan Sub-basin, offshore north-west Australia. Their findings from both areas agree with findings of this thesis, claiming that the carbonate mounds (build-ups) generally occur above deep-seated faults. However, Bailey et al. (2003) also studied the spatial distributions of faults and carbonate build-ups in the Porcupine Basin, offshore Ireland and their conclusions differ from those mentioned above. According to their findings, there was no spatial relationship between carbonate build-ups and faults in that area and suggests that there must be a different mechanism explaining the development of the build-ups. This is not impossible, but according to the findings of this thesis, I find it unlikely. I suspect that using a semi-automated method for faults detection, such as the Ant-tracking workflow, may reveal some minor faults and fractures and connections which could not be detected by an interpreter manually, directly from the seismic data.

The findings introduced in this thesis are consistent with the findings from previous research from the Loppa High area, other areas in the Barents Sea, and worldwide.

5. Conclusions

- The location of carbonate build-ups in the Loppa High study area is directly associated with location of faults and fractures mapped by applying the Ant-tracking workflow. All build-ups in the study area are associated with one or two faults or fractures. No build-ups were detected that could be claimed to be clearly 'fault-less'.

- Faults and fractures in the study area are located at the slope of the carbonate build-ups, mostly on one or both sides of the build-up ridge, where the steep dip of the build-up's side partly flattens into a gentle dip. Some faults are also located near to the top of the build-up ridge.

- Due to differences in seismic resolution of the two used surveys, the result of the Ant-tracking workflow reveals more faults and in sharper detail in the high resolution 3D seismic survey NH0372 than in the study area of 3D seismic survey SG9810.

- Detected carbonate build-ups are from 50 m to 500 m high and from 90 m to 600 m wide. The build-up ridges are from 400 m to 7000 m long. The faults and fractures associated with build-ups are detected regardless the size of the build-ups.

- Response of sinkholes, visible on the Top-Gipsdalen surface and also directly in the vertical seismic lines, was barely detected in the result of the Ant-tracking. It was detected only in the result of the Ant-tracking workflow in the site survey NH0372, when the Variance attribute cube was used as an edge detection method. No response was detected in the results from the study area of survey SG9810. The Ant-tracking workflow is not suitable for detection of sinkholes. However, the Variance attribute cube itself detects the response of sinkholes.

- Response of karstified faults was detected by the Ant-tracking workflow. The karstification process expands faults and consequently makes them easier to detect in the seismic data. However, the Ant-tracking workflow is not suitable for

detection of karst features in general. The response of the faults was detected not because they were karstified but in the first place because they were faults.

- The ‘Chaos – Ant-tracking workflow’ gives better results in the study area of seismic survey SG9810 and the ‘Variance – Ant-tracking workflow’ gives better results in the high resolution site survey NH0372.

- The results of this thesis confirm that the Ant-tracking workflow is an effective method for semi-automated detection of faults and fractures in seismic data. To achieve the best results, the parameters of the workflow must be customized with respect to the seismic data used and the exact objective of the study.

6. References

Ahr, W.M., 2008. Geology of Carbonate Reservoirs, pp. 277, John Wiley & Sons, Inc., Hoboken, New Jersey.

Bailey, W., Shannon, P.M., Walsh, J.J. & Unnithan, V., 2003. The spatial distributions of faults and deep sea carbonate mounds in the Porcupine Basin, offshore Ireland, *Marine and Petroleum Geology,* 20**,** 509-522.

Bates, R.L. & Jackson, J.A., 1980. Glossary of Geology 2nd edition, pp. 751, American Geological Institute, Falls Church, Virginia, USA.

Beauchamp, B., Harrison, J.C. & Henderson, C.M., 1989. Upper Paleozoic stratigraphy and basin analysis of the Sverdrup Basin, Canadian Arctic Archipelago: 1 - time frame and tectonic evolution, *Geological Survey of Canada,* Paper 89-1G**,** 115-124.

Berglund, L.T., Augustson, J., Færseth, R., Gjelberg, J. & Ramberg-Moe, H., 1986. The evolution of the Hammerfest Basin. *in Habitat of hydrocarbons on the Norwegian continental shelf: proceedings of an international conference (Habitat of Hydrocarbons - Norwegian Oil and Gas Finds)*, pp. 319-338, ed Spencer, A. M. Graham & Trotman for the Norwegian Petroleum Society, London.

Brekke, H. & Riis, F., 1987. Mesozoic tectonics and basin evolution of the Norwegian shelf between 60°N and 72°N, *Norsk geologisk tidsskrift,* 67**,** 295-322.

Brown, A.R., 1991. Interpretation of three-dimensional seismic data, 3rd edition, *AAPG Memoir,* 42, Tulsa, Oklahoma**,** 341.

Carrillat, A., Hunt, D., Randen, T., Sonneland, L. & Elvebakk, G., 2005. Automated mapping of carbonate build-ups and palaeokarst from the Norwegian Barents Sea using 3D seismic texture attributes. *in Petroleum Geology: North-West Europe and Global Perspectives – Proceedings of the 6th Petroleum Geology Conference*, pp. 1595-1611 eds Doré, A. G. & Vining, B. A. Petroleum Geology Conferences Ltd. Published by the Geological Society, London.

Cutbill, J.L. & Challinor, A., 1965. Revision of the stratigraphical scheme for the Carboniferous and Permian rocks of Spitsbergen and Bjørnøya, *Geological Magazine,* 102**,** 418-439.

Dallmann, W.K., Gjelberg, J.G., Harland, W.B., Johannessen, E.P., Keilen, H.B., Lønøy, A., Nilsson, I. & Worsley, D., 1999. Upper Palaeozoic lithostratigraphy. *in Lithostratigraphic lexicon of Svalbard: review and recommendations for nomenclature use : Upper Palaeozoic to Quaternary bedrock*, pp. 25-126, ed Dallmann, W. K. Norsk Polarinstitutt, Tromsø.

Doré, A.G., 1991. The structural foundation and evolution of Mesozoic seaways between Europe and the Arctic, *Palaeogeography, Palaeoclimatology, Palaeoecology,* 87**,** 441-492.

Elvebakk, G., Hunt, D.W. & Stemmerik, L., 2002. From isolated buildups to buildup mosaics: 3D seismic sheds new light on upper Carboniferous-Permian fault controlled carbonate buildups, Norwegian Barents Sea, *Sedimentary Geology,* 152**,** 7-17.

Ezaki, Y., Kawamura, T. & Nakamura, K., 1994. Kapp Starostin Formation in Spitsbergen: A sedimentary and faunal record of Late Permian palaeoenvironments in an Arctic region, *Canadian Society of Petroleum Geologists Memoir,* 17**,** 647-655.

Gabrielsen, R.H., Færseth, R.B., Jensen, L.N., Kalheim, J.E. & Riis, F., 1990. Structural elements of the Norwegian Continental Shelf. Part 1: The Barents Sea region. *NPD Bulletin* v. 6, Norwegian Petroleum Directorate, http://www.npd.no/Global/Norsk/3%20-%20Publikasjoner/NPD%20Bulletin/NPD_BulletinNr6.pdf.

Harland, W.B., Anderson, L.M. & Manasrah, D., 1997. The geology of Svalbard, pp. 521, Geological Society, London.

Hovland, M., Croker, P.F. & Martin, M., 1994. Fault-associated seabed mounds (carbonate knolls?) off western Ireland and north-west Australia, *Marine and Petroleum Geology,* 11**,** 232-246.

Hunt, D., Elvebakk, G., Rafaelsen, B., Pajchel, J., Hogstad, K., Robak, H. & Randen, T., 2003. Palaeokarst Recognition & 3D Distribution - New Insights From The Upper Palaeozoic, Loppa High, Barents Sea: Extended abstract, *EAGE 65th conference & exhibition,* Stavanger, Norway, 2 - 5 June 2003.

Larssen, G.B., Elvebakk, G., Henriksen, L.B., Kristensen, S.-E., Nilsson, I., Samuelsberg, T.J., Svånå, T.A., Stemmerik, L. & Worsley, D., 2002. Upper Palaeozoic lithostratigraphy of the Southern Norwegian Barents Sea. *NPD Bulletin* v. 9, Norwegian Petroleum Directorate, http://www.npd.no/Global/Norsk/3%20-%20Publikasjoner/NPD%20Bulletin/PalaeozoicNomenclature_17.pdf.

NormanEinstein, 2005. The map: location of the Barents Sea and the surrounding seas and islands, http://commons.wikimedia.org/wiki/File:Barents_Sea_map.png.

NPD, 2009. Norwegian Petroleum Directorate, http://www.npd.no/engelsk/cwi/pbl/en/well/all/5039.htm.

NPD, 2010. Norwegian Petroleum Directorate, http://www.npd.no/engelsk/cwi/pbl/en/su/all/150.htm.

Pedersen, S., Skov, T., Randen, T. & Sønneland, L., 2005. Automatic Fault Extraction Using Artificial Ants, *Mathematical Methods and Modelling in Hydrocarbon Exploration and Production***,** 107-116.

Pedersen, S.I., Randen, T., Sonneland, L. & Steen, O., 2002. Automatic fault extraction using artificial ants. 72nd Annual International Meeting, *SEG Expanded Abstracts,* 21**,** 512-515.

Rafaelsen, B., Andreassen, K., Samuelsberg, T.J., Hogstad, K. & Randen, T., 2003a. Upper Paleozoic carbonate build-ups in the norwegian Barents sea - new insights from 3-D seismic and automated facies mapping, *EAGE 65th Conference & Exhibition,* Stavanger, Norway, 2 - 5 June 2003.

Rafaelsen, B., Elvebakk, G., Andreassen, K., Stemmerik, L., Colpaert, A. & Samuelsberg, T.J., 2008. From detached to attached carbonate buildup complexes - 3D seismic data from the upper Palaeozoic, Finnmark Platform, southwestern Barents Sea, *Sedimentary Geology,* 206**,** 17-32.

Rafaelsen, B., Elvebakk, G., Hunt, D., Andreassen, K. & Randen, T., 2003b. Automated 3D seismic facies mapping of Upper Paleozoic carbonates in the southwestern Norwegian Barents Sea, http://www.nhm.uio.no/forskning-samlinger/studier/geologi/svalex/ressurs_CD/Papers_and_extended_abstracts/Rafaelsen_et_al_2003b_Ext.pdf.

Rafaelsen, B., Holm, J.P. & Svindland, K.T., 2006. Karst, a potential geohazard and reservoir, http://www.carbonet.net/bjarne/Rafaelsen%202006.swf.

Rønnevik, H., Beskow, B. & Jacobsen, H.P., 1982. Structural and stratigraphic evolution of the Barents Sea, *Offshore North Seas 1982,* Technology Conference and Exhibition, Stavanger**,** pp. 29.

Schlumberger, 2009a. Petrel 2009, Seismic-to-Simulation Software manual: Interpreter's Guide to Seismic Attributes, Houston.

Schlumberger, 2009b. Petrel 2009, Seismic-to-Simulation Software manual: Seismic Visualization and Interpretation Course, Houston.

Scoffin, T.P., 1987. An introduction to carbonate sediments and rocks., pp. 77-78. Blackie; Chapman and Hall, Glasgow; New York.

Shi, J., 2009. Application of Ant Tracking Technology in Small Fault Interpretation, *Journal of Oil and Gas Technology,* 2.

Silva, C.C., Marcolino, C.S. & Lima, F.D., 2005. Automatic Fault Extraction Using Ant Tracking Algorithm in the Marlim South Field, Campos Basin, *SEG Expanded Abstracts,* 24.

Steel, R.J. & Worsley, D., 1984. Svalbard's post-Caledonian strata - an atlas of sedimentational patterns and palaeogeographic evolution. *in Petroleum Geology of the North European Margin*, pp. 109-135, eds Spencer, A. M., Holter, E., Johnsen, S. O., Mørk, A., Nysæther, E., Songstad, P. & Spinnangr, Å. Norwegian Petroleum Society, Graham and Trotman, London.

Stemmerik, L., 2000. Late Palaeozoic evolution of the North Atlantic margin of Pangea, *Palaeogeography, Palaeoclimatology, Palaeoecology,* 161**,** 95-126.

Stemmerik, L., Elvebakk, G. & Worsley, D., 1999. Upper Palaeozoic carbonate reservoirs on the Norwegian Arctic Shelf: delineation of reservoir models with application to the Loppa High, *Petroleum Geoscience,* 5**,** 173-187.

Stemmerik, L., Larson, P.A., Larssen, G.B., Mørk, A. & Simonsen, B.T., 1994. Depositional evolution of lower permian Palaeoaplysina build-ups, Kapp duner formation, Bjørnøya, Arctic Norway, *Sedimentary Geology,* 92**,** 161-174.

Stemmerik, L. & Worsley, D., 1989. Late Palaeozoic sequence correlations, North Greenland, Svalbard and the Barents Shelf. *in Correlation in Hydrocarbon Exploration, 99-111*, ed Collinson, J. D. Norwegian Petroleum Society, Graham & Trotman, London.

Stemmerik, L. & Worsley, D., 2005. 30 years on – Arctic Upper Palaeozoic stratigraphy, depositional evolution and hydrocarbon prospectivity, *Norwegian Journal of Geology,* 85**,** 151-168.

Sutadiwiria, G. & Prasetyo, H., 2006. Uncertainty in Geophysic-Geology-Reservoir Modelling for Globigerinid Sands Carbonate in the NE-Java Basin, Indonesia: Case Study: Planning vs. Actual Field Development in the Madura Strait, Indonesia, *Society of Petroleum Engineers*.

SwRI®, 2007. Carbonate Fault Project. Southwest Research Institute®, San Antonio, Texas, http://www.swri.org/4org/d20/deps/consortium/images/cfp.pdf and http://www.cfp.swri.org/

UniCam, 2006. Faults & Fractures in Carbonates. University of Camerino Project, http://www.serg.unicam.it/Faults.htm.

Worsley, D., 2008. The post-Caledonian development of Svalbard and the western Barents Sea, *Polar Research,* 27**,** 298-317.

Worsley, D., Aga, O.J., Dalland, A., Elverhøi, A. & Thon, A., 1986. The geological history of Svalbard, evolution of an arctic archipelago, pp. 121, Statoil, Aske Trykkeri, Stavanger.

Worsley, D., Agdestein, T., Gjelberg, J.G., Kirkemo, K., Mørk, A., Nilsson, I., Olaussen, S., Steel, R.J. & Stemmerik, L., 2001. The geological evolution of Bjørnøya, Arctic Norway: Implications for the Barents Shelf, *Norsk Geologisk Tidsskrift,* 81**,** 195-234.

7. Appendix

7.1. Calculating the seismic resolution

The calculation of seismic resolution in carbonates of the Gipsdalen Group was carried out as described in Brown (1991). With increasing depth, the frequency of the signal decreases, due to faster attenuation of higher frequencies. The seismic velocity depends on the composition of rocks and on depth. The seismic velocity increases with depth where the older and deeper rocks are more compacted.

The resolution has both vertical and horizontal aspects. Vertical resolution is taken as a quarter of wavelength. This is the closest separation of two wavelets of a given bandwidth.

Vertical resolution = $\frac{\lambda}{4} = \frac{v}{4f}$, where: λ – wavelength; v – seismic velocity; f – seismic frequency

Horizontal resolution is taken as width of the first Fresnel zone.

Horizontal resolution = $v\sqrt{\frac{t}{f}}$, where: v – seismic velocity; t – depth in time; f – seismic frequency

Migration is improving the horizontal resolution. By 2D migration, the Fresnel zone collapses into an ellipse perpendicular to the line (Figure 7.1). By 3D migration, it collapses into a small circle (Figure 7.1) of diameter $\lambda/4$. The diameter of $\lambda/4$ is for perfect migration and is in praxis depending on the data quality. It might be up to twice this size ($\lambda/2$). The data quality used in this thesis is good. Both the vertical and the horizontal resolution will be calculated as a quarter of the wavelength ($\lambda/4$). To calculate the seismic resolution, we need to know seismic velocity and dominant frequency of the real spectra in the seismic unit.

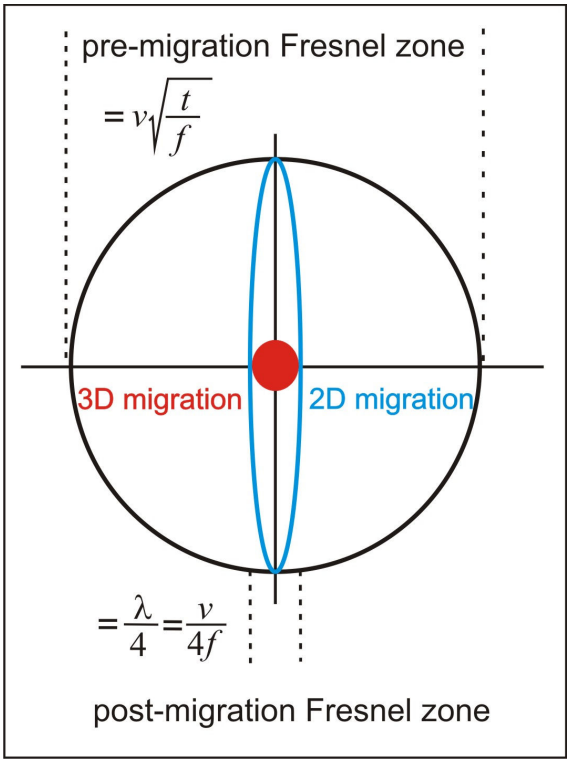

Figure 7.1 Effect on Fresnel zone size and shape by 2D and 3D migration (modified from Brown, 1991).

The seismic velocity was calculated in the carbonates of the Gipsdalen Group, between Top-Gipsdalen and Top-basement surfaces (Figure 3.19). Values of two-way-travel time and depth were taken from measurements in the well 7220/6-1 (Figure 3.19). The calculated seismic velocity is 5078.5 ms^{-1}. In further calculation of the seismic resolution velocity of 5000 ms^{-1} will be used.

Calculation of seismic velocity:

$$v = \frac{\Delta z}{\Delta t}, \quad \Delta t = \frac{t_2 - t_1}{2}, \quad \Delta z = z_2 - z_1$$ where:

v – seismic velocity
Δz – thickness of seismic unit
z_2, z_1 – depths
Δt – one way time
t_2, t_1 – two-way-travel times

$$\Delta z = z_2 - z_1 = 1457.93 - 1112.44 = 345.49\ m$$

$$\Delta t = \frac{t_2 - t_1}{2} = \frac{1.20514 - 1.0608}{2} = 0.06803\ s$$

$$v = \frac{\Delta z}{\Delta t} = \frac{345.49}{0.06803} = 5078.5\ ms^{-1}$$

To determine dominant frequency, volume attribute cube, the Dominant Frequency, was applied to the data (Figure 7.2, Figure 7.3). The Dominant Frequency attribute cube reveals the time varying spectral properties of seismic data (Schlumberger, 2009a). The dominant frequency in carbonates of the Gipsdalen Group was determined 55 Hz in survey NH0372 (Figure 7.2) and 30 Hz in survey SG9810 (Figure 7.3). This was also confirmed by an application of high-pass filter, applying filters with gradually decreasing high-pass and observing when a detectable change in the carbonate level appears.

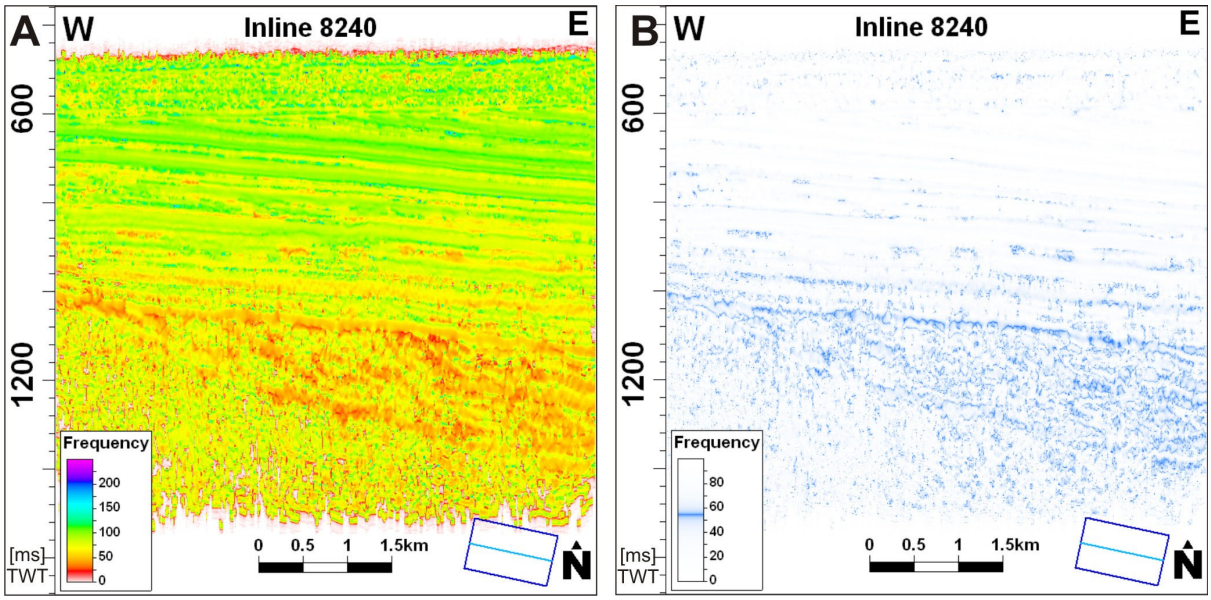

Figure 7.2 Dominant frequency attribute cube applied to the data. Seismic inline 8240, high resolution survey NH0372. (A) Frequencies displayed in colour scale. (B) Dominant frequency in carbonates of the Gipsdalen Group (55 Hz) is enhanced.

Seismic resolution in carbonates of the Gipsdalen Group in the high resolution seismic survey NH0372 was calculated as 23 m.

$$\frac{\lambda}{4} = \frac{v}{4f} = \frac{5000}{4 \times 55} = 22.7\,m$$

Seismic resolution in carbonates of the Gipsdalen Group in the seismic survey SG9810 was calculated as 42 m.

$$\frac{\lambda}{4} = \frac{v}{4f} = \frac{5000}{4 \times 30} = 41.7\,m$$

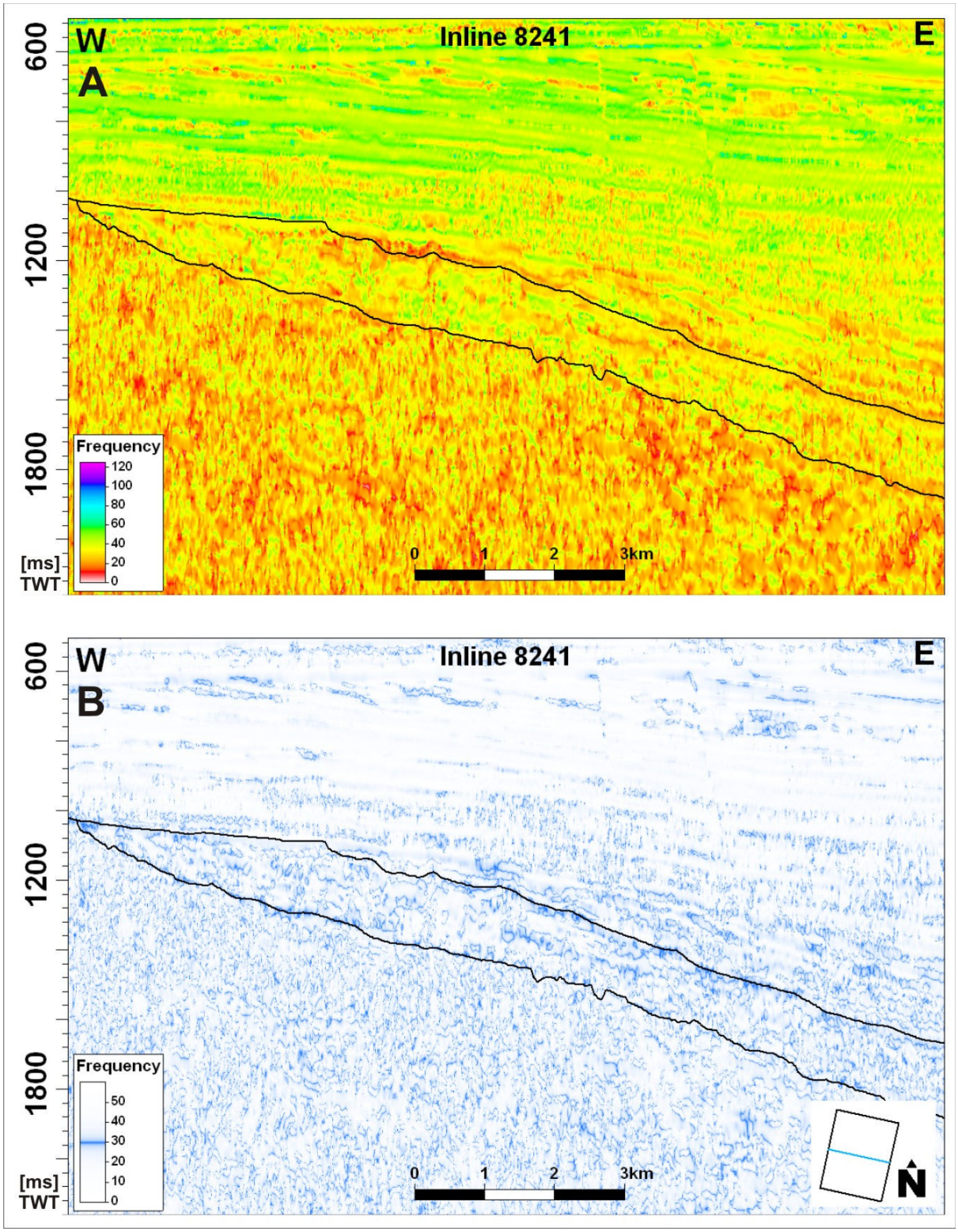

Figure 7.3 Dominant frequency attribute cube applied to the data. Seismic inline 8241, 3D seismic survey SG9810. (A) Frequencies displayed in colour scale. (B) Dominant frequency in carbonates of the Gipsdalen Group (30 Hz) is enhanced.